Rationally Engineering Porous Carbon-Based Metal Nanocomposites for Efficient and Durable Electrocatalysis Applications

by

Zhen Zhang

A thesis
presented to the University of Waterloo
in fulfillment of the
thesis requirement for the degree of
Doctor of Philosophy
in
Chemical Engineering

Waterloo, Ontario, Canada, 2021

Examining Committee Membership

The following served on the Examining Committee for this thesis. The decision of the Examining Committee is by majority vote.

External Examiner	Dr. Feng Jiao Associate Professor
Supervisor	Dr. Zhongwei Chen Professor
Internal Member	Dr. Ali Elkamel Professor
Internal Member	Dr. Jeff Gostick Associate Professor
Internal-external Member	Dr. Zhongchao (Chao) Tan Professor

Author's Declaration

This thesis consists of material all of which I authored or co-authored: see Statement of Contributions included in the thesis. This is a true copy of the thesis, including any required final revisions, as accepted by my examiners.

I understand that my thesis may be made electronically available to the public.

Statement of Contributions

The body of this thesis is based upon a combination of published works. Various chapters are adapted from the following list of publications.

Chapter 2 of this thesis consist of a review paper that was co-authored by myself, my supervisor, Dr. Zachary Paul Cano, Dr. Dan Luo, Dr. Haozhen Dou, Dr. Aiping Yu. I am the first author of this paper. I conceptualized study design, and performed data collection and manuscript writing. My coauthors reviewed the manuscript and provided feedback on draft manuscript.

"Rational Design of Tailored Porous Carbon-Based Materials for CO_2 Capture", *Journal of Materials Chemistry A*, 2019, 7 (37), 20985-21003.

Chapter 3 of this thesis consist of a paper that was co-authored by myself, my supervisor, Dr. Ya-Ping Deng, Dr. Zhenyu Xing, Dr. Dan Luo, Dr. Serubbabel Sy, Dr. Zachary Paul Cano, Dr. Guihua Liu, Dr. Yi Jiang. I am the first author of this paper. I conceptualized study design, carried out the experiment, collected and analyzed the data, and prepared the manuscript. My coauthors provided advice during research and gave feedback on draft manuscript.

"'Ship in a Bottle' Design of Highly Efficient Bifunctional Electrocatalysts for Long-Lasting Rechargeable Zn−Air Batteries", *ACS Nano*, 2019, 13 (6), 7062-7072.

Chapter 4 of this thesis consist of a paper that was co-authored by myself, my supervisor, Dr. Dan Luo, Dr. Gaoran Li, Dr. Rui Gao, Dr. Matthew Li, Dr. Shuang Li, Dr. Lei Zhao, Dr. Haozhen Dou, Dr. Guobin Wen, Dr. Serubbabel Sy, Dr. Yongfeng Hu, Dr. Jingde Li, Dr. Aiping Yu. I am the first author of this paper. I conceptualized study design, carried out the experiment, collected and analyzed the data, and prepared the manuscript. My coauthors provided advice during research and gave feedback on draft manuscript.

"Tantalum-Based Electrocatalyst for Polysulfide Catalysis and Retention for High-Performance Lithium-Sulfur Batteries", *Matter*, 2020, 3 (3), 920-934.

Chapter 5 of this thesis consist of a paper that was co-authored by myself, my supervisor, Dr. Guobin Wen, Dr. Dan Luo, Dr. Bohua Ren, Dr. Yanfei Zhu, Dr. Rui Gao, Dr. Haozhen Dou, Dr. Guiru Sun, Dr. Ming Feng, Dr. Zhengyu Bai, Dr. Aiping Yu. I am the first author of this paper. I conceptualized study design, carried out the experiment, collected and analyzed the data, and prepared the manuscript. My coauthors provided advice during research and gave feedback on draft manuscript.

"'Two Ships in a Bottle' Design for Zn-Ag-O Catalyst Enabling Selective and Long-Lasting CO_2 Electroreduction", *Journal of the American Chemical Society*, 2021, 143 (18), 6855-6864.

Abstract

Electrocatalysis plays an essential role in electrochemical energy storage and conversion, enabling a number of sustainable processes for future technologies such as metal−air batteries, sulfur-based batteries, and carbon dioxide (CO_2) conversion. The grand challenge is to develop advanced electrocatalysts with enhanced activity, selectivity and durability to enable widespread adoption of clean energy technologies. Carbon-based metal hybrid materials have been receiving intense interest as promising electrocatalysts for the electrochemical transformations central to the energy conversion and chemical production technologies. Constructing effective electrocatalysts requires fundamental understanding, rational design and delicate manipulation of the catalytically active sites. This thesis work presents advanced electrocatalyst design strategies by rationally engineering porous carbon-based metal nanocomposites for promising electrochemical transformation systems including oxygen, sulfur, and CO_2 electrocatalysis, providing a new route to efficiently convert abundant resources such as H_2O, S, and CO_2 to electricity to march toward a sustainable energy future.

In the first study (Chapter 3), a unique “ship in a bottle” concept in catalyst design is proposed, which is to impregnate metal nanoparticles/nanoclusters inside the nanopores of a porous carbon matrix. As a proof-of-concept, the catalyst, composed of cobalt sulfide (CoS_2) nanoparticles impregnated within the S-doped defective carbon nanopores that act as interconnected nanoreactors, is engineered for bifunctional oxygen electrocatalysis including oxygen reduction (ORR) and oxygen evolution reaction (OER). The erected 3D porous conductive architecture provides a “highway” for expediting charge and mass transfer. This design not only delivers a high surface-to-volume ratio to increase numbers of exposed

catalytic sites but also precludes nanoparticles from aggregation during cycling owing to the pore spatial confinement effect. Therefore, the long-term plague inherent to nanocatalyst stability can be solved. Moreover, the synergistic coupling effects between defect-rich interfaces and chemical bonding derived from heteroatom-doping boost the catalytic activity and prohibit the detachment of nanoparticles for better stability. Consequently, the developed catalyst not only presents superior bifunctional oxygen electrocatalytic activities and durability, but also enables a long-term cyclability for over 340 hours at a high current density of 25 mA cm^{-2} in a practical application of rechargeable Zn−air batteries. Such a universal "ship in a bottle" design offers an appealing and instructive model of nanocatalyst engineering.

Based on the proposed "ship in a bottle" design concept, the second work (Chapter 4) further introduces defect engineering and crystallinity manipulation of metal nanoclusters. The engineered ultrafine amorphous tantalum oxide nanoclusters with oxygen vacancies (Ta_2O_{5-x}) implanted inside a microporous carbon matrix are, for the first time, employed as a new electrocatalyst for polysulfide catalysis and retention. Through a pore-constriction mechanism, the dimensions of tantalum oxide are controlled to be nanosized, not only shaping the incomplete unit cell in an amorphous structure for efficient crystallinity tuning, but also exposing abundant polysulfide-retaining and catalytically active sites. The introduced oxygen vacancies in tantalum oxide manipulating electron structure with increased intrinsic conductivity function as catalytic centers to accelerate sulfur redox reactions. Moreover, the polysulfide shutting effect, sulfur agglomeration and volume expansion are well suppressed in the designed pitaya-like structure. As a result, the developed sulfur electrode in a lithium-sulfur battery presents excellent cycling stability and rate capability at practically relevant sulfur loadings and electrolyte content.

The last study (Chapter 5) further optimizes the monometallic design to a bimetallic design by a "two ships in a bottle" strategy to meet higher electrocatalyst requirements. The engineered bimetallic Zn-Ag-O catalysts, where ZnO and Ag phases are twinned to constitute an individual ultrafine nanoparticle impregnated inside nanopores of an ultrahigh-surface-area carbon matrix, enable selective and durable CO_2 electroreduction to CO. Bimetallic electron configurations are modulated by constructing a Zn-Ag-O interface, where the electron density reconfiguration arising from electron delocalization enhances the stabilization of the *COOH intermediate favorable for CO production, while promoting CO selectivity and suppressing HCOOH generation by altering the rate-limiting step toward a high thermodynamic barrier for forming HCOO*. Moreover, the pore-constriction mechanism restricts the bimetallic particles to nanosized dimensions with abundant Zn-Ag-O heterointerfaces and exposed active sites, meanwhile prohibiting detachment and agglomeration of nanoparticles during CO_2 reduction for enhanced stability. The designed catalysts realize 60.9% energy efficiency and $94.1 \pm 4.0\%$ Faradaic efficiency toward CO, together with a remarkable stability over 6 days. Beyond providing a high-performance CO_2 reduction electrocatalyst, this study presents a promising catalyst-design strategy for efficient energy conversion.

Acknowledgements

Time flies, thesis writing here means the invaluable journey of my Ph.D. study is coming to an end. Here I would like to express my sincere gratitude to my supervisor, Professor Zhongwei Chen who provided me with strong support, guidance and advice during my Ph.D. study. He gave me the freedom to pursue various research ideas; without his support, I would never have accomplished so much. His insightful guidance for me is not only on the research but also on the way of thinking and solving problems in life.

Moreover, I appreciate my Ph.D. thesis examining committee members, including Professor Jeff Gostick, Professor Ali Elkamel, and Professor Zhongchao (Chao) Tan from the University of Waterloo, and Professor Feng Jiao as the external examiner from the University of Delaware for their valuable time and insights.

In addition, I would like to thank all the group members who were always there to help in my project. I appreciate my outstanding colleagues including but not limited to Dr. Dan Luo, Dr. Zachary Paul Cano, Dr. Rui Gao, Dr. Ya-Ping Deng, Dr. Guobin Wen, Dr. Gaoran Li, Dr. Haozhen Dou, Dr. Lei Zhao, Dr. Zhenyu Xing, Dr. Jingde Li, Dr. Guihua Liu, Dr. Matthew Li, Dr. Gaopeng Jiang, and Dr. Zhong Ma for their valuable advice on my research.

Finally, I would like to give my sincere gratitude to my parents and fiancee Xiaojuan Du for their unconditional support, encouragement and love. I would also like to thank all those lovely close friends that I have made here in Waterloo. Thanks for all their generous support whenever and wherever I needed.

The memory I had here in Waterloo will last forever.

Table of Contents

List of Figures

List of Tables

List of Abbreviations

3DOM – Three-dimensional ordered macropores

ACs – Activated carbons

BET – Brunauer–Emmett–Teller

BJH – Barrett–Joyner–Halenda

BE – Binding energy

CO_2RR – CO_2 reduction reaction

CBM – Conduction band minimum

CN – Carbon nitride

CVD – Chemical vapor deposition

CMG – Chemically modified graphene

CNTs – Carbon nanotubes

CA measurement – Chronoamperometric measurement

CV – Cyclic voltammetry

DWCNTs – Double-walled carbon nanotubes

DFT – Density functional theory

DOL – 1,3-dioxolane

DME – Dimethoxymethane

EDS – Energy-dispersive X-ray spectroscopy

EELS – Electron energy loss spectroscopy

EPR – Electron paramagnetic resonance

EIS – Electrochemical impedance spectroscopy

EXAFS – Extended X-ray absorption fine structure

E_{ads} – Adsorption energy

E/S ratio – Electrolyte/sulfur ratio

EE_{ca} – Cathodic energy efficiency

FFT – Fast Fourier transform

FT – Fourier transformed

FE – Faradaic efficiency

GO – Graphite oxide

GODCs – Graphene oxide derived carbons

GDL – Gas diffusion layer

GC – Gas chromatography

HTC – Hydrothermal carbonization

HMF – Hydroxymethyl furfural

HRTEM – High-resolution transmission electron microscopy

HAADF-STEM – High-angle annular dark-field scanning transmission electron microscopy

HER – Hydrogen evolution reaction

Ir/C – Carbon support iridium catalyst

I_D/I_G ratio – The intensity ratio of D and G peaks

IRMOFs – Isoreticular metal organic frameworks

ICP-OES – Inductively coupled plasma optical emission spectrometer

K–L equation – Koutecky–Levich equation

KJ – Ketjen Black EC600JD

Li-S – Lithium-sulfur

LiTFSI – Lithium bis(trifluoromethanesulfony) imide

LSV – Linear sweep voltammetry

LED – Light-emitting diode

LPS – Lithium polysulfide

MNPs – Metal nanoparticles

MOFs – Metal organic frameworks

NMP – *N*-Methyl-2-pyrrolidone

NMR – Nuclear magnetic resonance

ORR – Oxygen reduction reaction

OER – Oxygen evolution reaction

PSD – Pore size distribution

Pt/C – Carbon support platinum catalyst

PCET – Proton-coupled electron transfer

PMMA – Poly(methylmethacrylate)

PVDF – Poly(vinylidene fluoride)

PDOS – Projected density of states

QSDFT – Quenched solid density function theory

RDE – Rotating disk electrode

RHE – Reversible hydrogen electrode

SCE – Saturated calomel electrode

SEM – Scanning electron microscopy

SAED – Selected area electron diffraction

TEM – Transmission electron microscopy

TGA – Thermogravimetric analysis

TPD – Temperature programmed desorption

TEOS – Tetraethyl orthosilicate

UMNPs – Ultrafine metal nanoparticles

VBM – Valence band maximum

VASP – Vienna ab initio Simulation Package

XRD – X-ray diffraction

XPS – X-ray photoelectron spectroscopy

XAS – X-ray absorption spectroscopy

XANES – X-ray absorption near-edge structure

Chapter 1 Introduction

1.1 Background

The rapid rise in global population and industrialization advances, powered by immoderate fossil fuel exploitation, have resulted in emergency problems of climate change and energy crisis.[1] Nowadays, a promising movement for carbon neutrality is urgently taking shape worldwide. In this context, it is critical to balance increasing energy demand and pursing low emissions. Global awareness on energy utilization is experiencing a transformation from the industrial civilization based on pollutive fossil fuels to the sustainable one driven by renewable clean energies such as solar, wind, and hydroelectric power.

To date, renewable energy costs have declined significantly, providing affordable carbon-free electricity right now. For example, solar electricity costs of 2 US cents per kWh were reported by the International Energy Agency (IEA)'s World Energy Outlook 2020 representing a decrease of 95% since 2009,[2] which is now competitive with fossil fuels typically costing 4-6 US cents per kWh. As displayed in Figure 1.1, the electrical energy generated from renewable energy resources has been increasingly contributing to the electricity generation market. However, the installation of renewables alone cannot meet the world's targeted carbon emissions reduction and energy supply; the greater challenge arises from the intermittent and unpredictable nature of renewable energy resources (e.g., wind and sunlight), which necessitate efficient interconversion between electrical and chemical energy to store off-peak electricity produced from these resources.

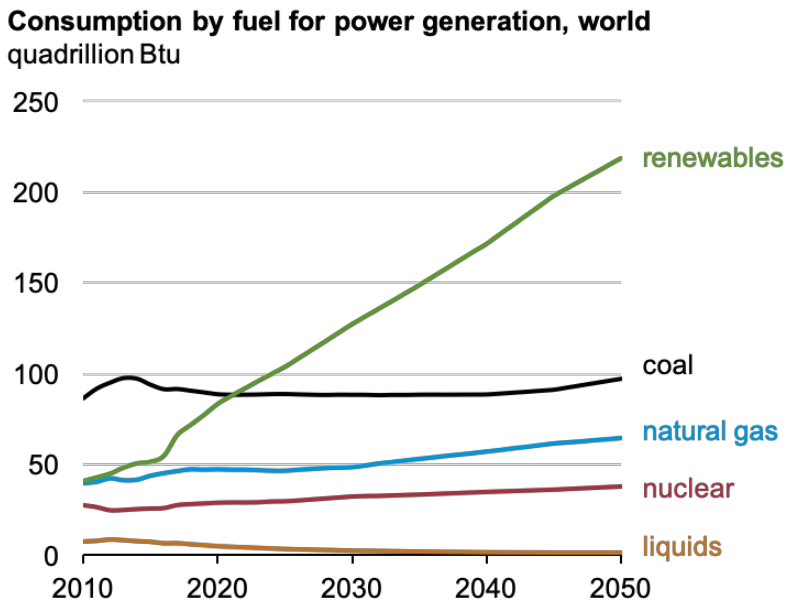

Figure 1.1 Global electric power generation fuel-mix.[3]

Electrochemical energy conversion and storage systems have emerged as the most promising technology, which can utilize excess renewably produced electricity for energy storage and further dispatch by a smart grid for residential and industrial end uses (Figure 1.2). In the electrochemical energy system, the electricity can be converted into chemical energy stored in chemical bonds in molecules. A fascinating prospect is to develop electrochemical conversion processes that can convert abundant resources in the Earth's atmosphere such as water, carbon dioxide (CO_2), and nitrogen into important chemicals and fuels including hydrogen, hydrocarbons, oxygenates, and ammonia, ultimately resulting in a closed water cycle, carbon cycle, and nitrogen cycle by coupling to renewable energy.[4]

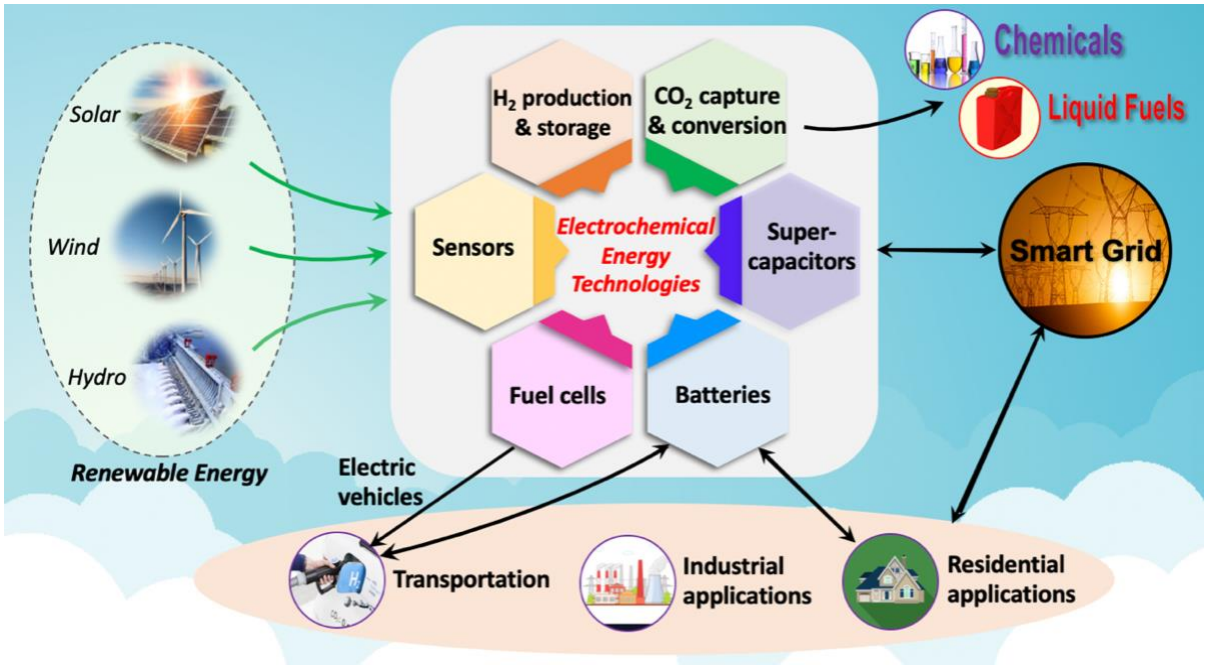

Figure 1.2 Schematic of electrochemical energy technologies and their applications.

Electrocatalysis plays an essential role in electrochemical energy conversion and storage, enabling a number of sustainable processes for future technologies including oxygen electrocatalysis in metal−air batteries, sulfur electrocatalysis in lithium-sulfur (Li-S) batteries, and CO_2 electrocatalysis for carbon utilization. Specifically, Zn−air batteries represent a promising energy storage system because of the high energy density (1086 Wh kg^{-1}, 4 times higher than the widely used lithium-ion batteries), improved safety, and environmental compatibility (Figure 1.3a).[5] During discharging, atmospheric oxygen diffuses into the porous air electrode and is ready to be reduced to hydroxide ions via the oxygen reduction reaction (ORR). During charging, the Zn−air batteries are capable of storing electric energy through the oxygen evolution reaction (OER). Both ORR and OER are the critical reactions at the cathode side, determining the overall efficiency and electrochemical performance of Zn−air batteries.[6] Besides, another important example is the Li-S batteries (Figure 1.3b) that represent one of the

most promising contenders in the "beyond lithium-ion batteries" energy-storage arena to support the ever-expanding electrical market due to the low cost ($0.2 per kg of sulfur vs. $40 per kg of $LiCoO_2$), high theoretical capacity (1672 mAh g^{-1}), and natural abundance of sulfur.[7] The Li-S energy is generated through the electrochemical redox reaction between S and lithium sulfide (Li_2S) involving a series of multi-step reactions of intermediate polysulfide catalytic conversion.[8] In addition, another promising instance is the electrochemical CO_2 reduction reaction (CO_2RR) (Figure 1.3c), which presents a sustainable and feasible option to not only achieve a carbon-neutral cycle but also supplement or potentially replace the fossil-based resources to produce high value-added chemicals and fuels such as CO, formic acid, methane, methanol, ethylene, and ethanol to generate economic values.[9] On account of the thermodynamically stable nature of CO_2 molecule, effective catalysis must be involved in the CO_2 conversion process. In particular, CO_2RR involves a multiple proton-coupled electron-transfer (PCET) process, including $2e^-$, $4e^-$, $8e^-$, $12e^-$, or even more electrons pathways, leading to a variety of carbon-based products.[10] As such, it is crucial to enable selective catalytic conversion toward the specific product. Taken together, critical to enabling these promising electrochemical energy conversion systems is the development of efficient, durable, and selective electrocatalysts that act as the indispensable role in the electrochemical processes.

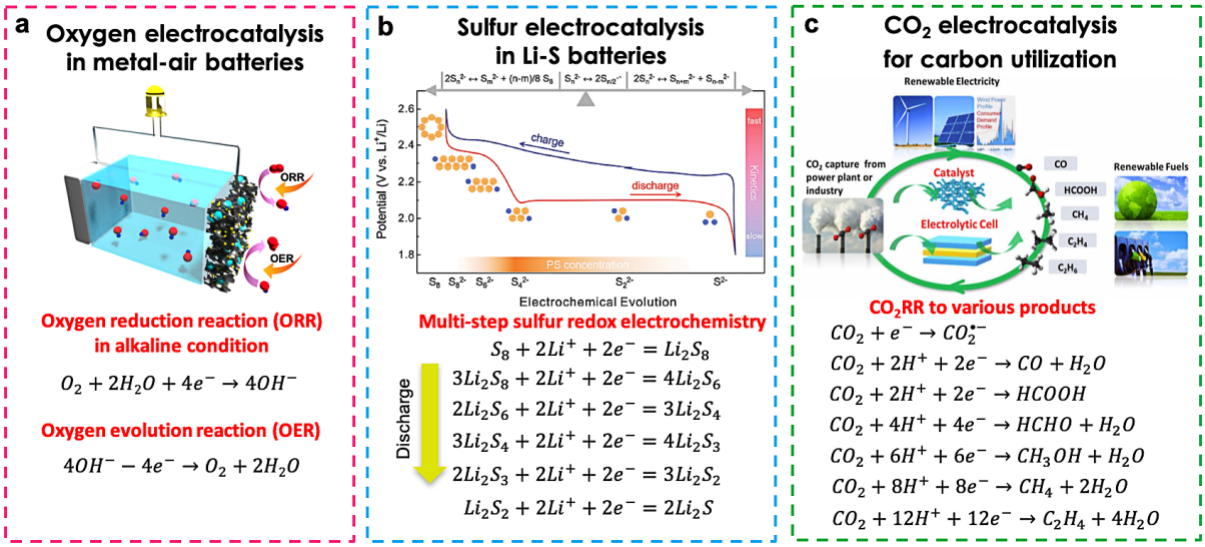

Figure 1.3 Key role of electrocatalysis in promising electrochemical energy conversion and storage systems including (a) oxygen electrocatalysis in metal−air batteries, (b) sulfur electrocatalysis in Li-S batteries,[11] and (c) CO_2 electrocatalysis for carbon utilization.

1.2 Motivation and Challenges

Constructing effective electrocatalysts requires fundamental understanding, rational design and delicate manipulation of the catalytically active sites. The ideal electrocatalysts should satisfy six criteria: i) high surface area for species adsorption and reaction at active sites; ii) optimal adsorption energy toward reactant, intermediate, and product; iii) high conductivity for direct electron transport; iv) high electrochemical stability; v) fast mass transport for improved kinetics; vi) strong interactions between active sites and support.

Decreasing the size of catalysts to a nanometer scale with an increased surface-to-volume ratio and facilely tunable surface properties showing particular features distinguishable from the bulk equivalents, provides a promising approach for constructing high-performance nanocatalysts.[12] The bulk equivalents normally show low utilization of active sites due to the

limited surface area and diffusion, while ultrafine metal nanoparticles (UMNPs) with a narrow size distribution are capable of providing a higher density of active sites available for electrocatalytic reactions and make the surface atoms more reactive, hence significantly enhancing atom efficiency and reducing the cost of precious-metal catalysts.[13] However, as the surface energy drastically increases with decreasing the particle size (Figure 1.4a), the synthesis of UMNPs with an uniform size and homogeneous distribution remains a great challenge. Worse yet, the UMNPs with high surface energy are in a thermodynamically unstable state and prone to aggregating during electrocatalytic reactions (Figure 1.4b), causing activity and stability loss. Therefore, control of size, shape, and dispersion of UMNPs is critical to construct an efficient electrocatalyst.

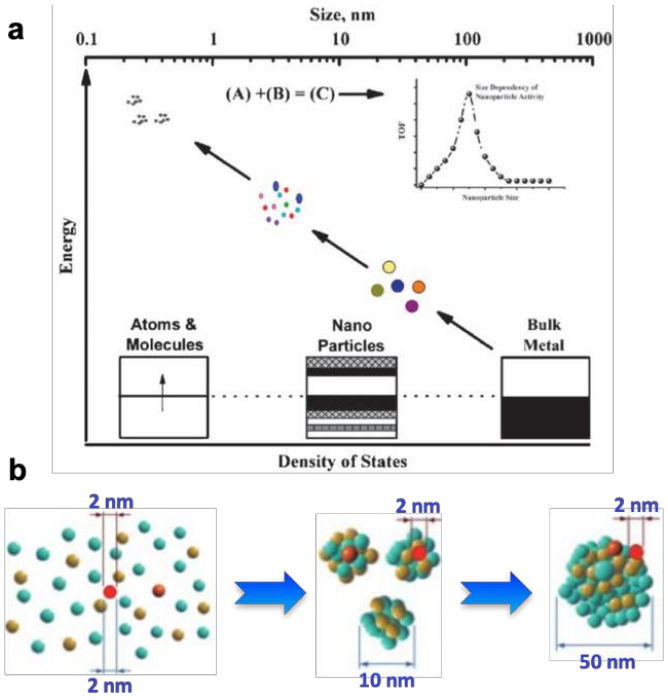

Figure 1.4 (a) Surface energy increasing with the decrease of particle size.[14] (b) Agglomeration of UMNPs due to high surface energy.

Having porous structures in electrocatalysts to support metal nanoparticles (MNPs) offers a viable strategy, which favors the construction of dispersed active sites and facilitates reactants/products transfer. Porous carbon-based materials have received great attention in electrocatalyst design and synthesis by virtue of their large surface area and porosity, abundant microstructures and morphologies, high intrinsic conductivity, good chemical and thermal stability, structural tunability at the atomic level, wide availability, and low cost.[15,16] The past few decades have witnessed the development of various carbon allotropes with unique properties, which offer the promise of technological breakthroughs of carbon-based electrocatalysts. As shown in Figure 1.5, various carbon-based materials with well-defined structures at nanoscale cover the entire range of dimensionalities, including i) 0D structure such as the fullerenes, carbon dots, and nanodiamonds, ii) 1D single-walled and multi-walled carbon nanotubes, iii) 2D structure such as graphene and multilayer graphitic nanosheets, and iv) 3D structure such as graphite and diamond.

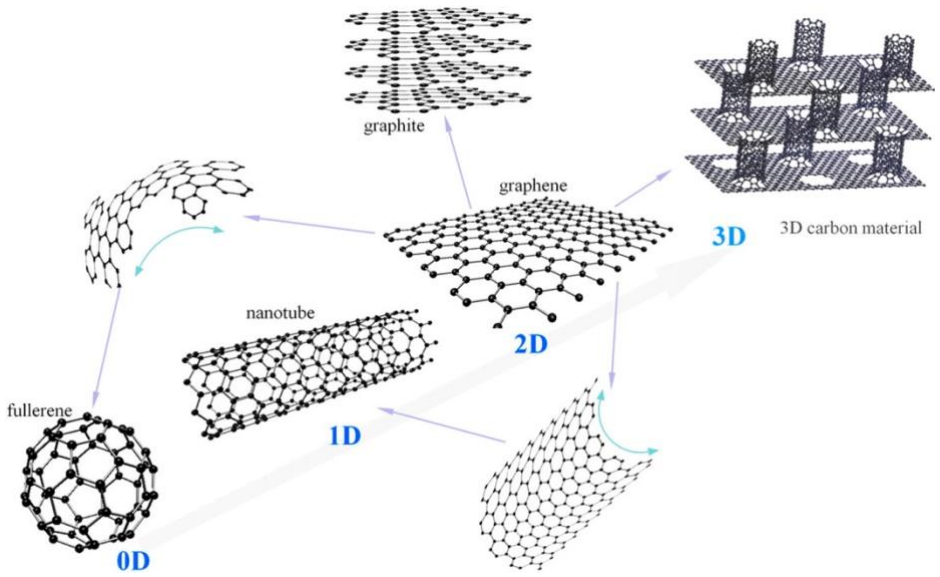

Figure 1.5 Classification of carbon allotropes as per their dimensionality.[17]

The electrocatalytic performances of porous carbon-based materials depend not only on the building blocks but also on the assembled hierarchical architectures.[18,19] The controlled integration of bare carbon nanostructures and active phases remains a challenge. Numerous efforts have been dedicated to the development of synthetic routes to carbon-based metal hybrid materials in recent years, including MNPs-deposition onto carbon matrix,[20] and carbon coating over MNPs.[21] In the former, 2D graphene/graphitic nanosheets or 1D carbon nanotubes are commonly employed as the supports, on which MNPs realize in situ growth and deposition (Figure 1.6a). However, this strategy cannot efficiently immobilize MNPs and control their growth during synthesis and electrocatalytic reactions, which could cause the aggregation and/or detachment of MNPs and thus degrade their catalytic activity and durability. As to the latter strategy, it can form a carbon-sealed confined space for MNPs (Figure 1.6b). However, this strategy normally lacks high and uniform porosity for sufficient mass transfer, as well as poor control of particle size and structural change due to the potential inconsistency of carbon-coating thickness, resulting in limited electrochemical performances. Therefore, rational structural design of porous carbon-based metal nanocomposites is crucial yet challenging to engineer advanced nanocatalysts toward promising electrocatalysis applications.

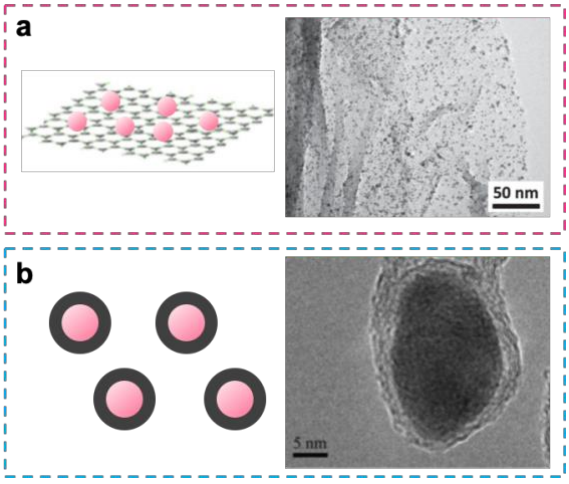

Figure 1.6 Schematics and corresponding morphology observation by transmission electron microscopy (TEM) of (a) MNPs-deposition onto carbon matrix,[22] and (b) carbon coating over MNPs.[23]

1.3 Research Objectives

The research objective of this thesis is to study advanced design strategies for rationally engineering porous carbon-based metal nanocomposites for efficient and durable electrocatalysis applications. Methodologies for immobilizing UMNPs to high-surface-area porous carbons will be developed to engineer electrocatalysts, achieving multi-objective optimization for improved catalytic activity, durability, and selectivity.

The specific objectives of this research include: i) design and synthesize UMNPs-supported porous carbon nanocomposites; ii) evaluate the capability and suitability of engineered materials when employed as catalysts in promising electrochemical transformation systems, including oxygen, sulfur, and CO_2 electrocatalysis; iii) understand how rational structural and compositional design influences the electrocatalytic performances in terms of activity, durability, and selectivity; iv) contribute to an innovative and general catalyst-design strategy of immobilizing metal phases to porous materials for wide implementation in various catalysis systems.

1.4 Structure of Thesis

A unique catalyst-design strategy of impregnating UMNPs into the nanopores of high-surface area porous carbon matrices is developed in this thesis work, which presents great potential for promising electrocatalysis applications (Figure 1.7).

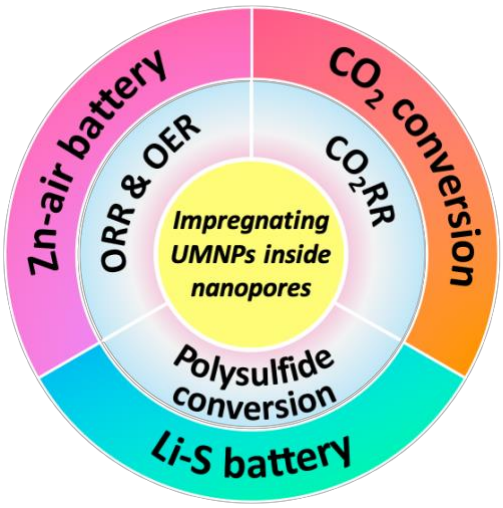

Figure 1.7 Catalyst design strategy of impregnating UMNPs into nanopores of high-surface-area porous carbon matrices for promising electrocatalysis applications.

Figure 1.8 depicts a breakdown of work conducted throughout this thesis. This thesis is organized in six chapters. **Chapter 1** introduces the background, motivation, current research progress and challenges of porous carbon-based metal hybrid electrocatalysts, scope and structure of the thesis work. **Chapter 2** presents some key synthesis routes to porous carbon materials and impregnation techniques for rationally engineering UMNPs-impregnated porous carbons. Three different tasks that have been published are discussed in subsequent Chapter 3-5. **Chapter 3** proposes a unique "ship in a bottle" concept to design electrocatalysts, which is to impregnate metal nanoparticles/nanoclusters inside the nanopores of a porous carbon matrix. As a proof-of-concept, the catalyst comprising cobalt sulfide (CoS_2) nanoparticles impregnated within the S-doped defective carbon nanopores that act as interconnected nanoreactors is engineered for efficient and durable bifunctional oxygen electrocatalysis for ORR and OER, enabling long-lasting rechargeable Zn−air batteries. **Chapter 4** further takes advantage of the "ship in a bottle" design strategy to manipulate metal nanoclusters crystallinity and introduce defect engineering. The engineered ultrafine amorphous tantalum oxide nanoclusters with

oxygen vacancies (Ta_2O_{5-x}) implanted inside a microporous carbon matrix are, for the first time, employed as a new electrocatalyst for polysulfide catalysis and retention, enabling high-performance Li-S batteries. **Chapter 5** further optimizes the monometallic design to a bimetallic design by a "two ships in a bottle" strategy to meet higher electrocatalyst requirements. The engineered bimetallic Zn-Ag-O catalysts, where ZnO and Ag phases are twinned to constitute an individual ultrafine nanoparticle impregnated inside nanopores of an ultrahigh-surface-area carbon matrix, enable highly selective and durable CO_2 electroreduction to CO. **Chapter 6** summarizes the important results and offers some discussions on the future direction that the work may take.

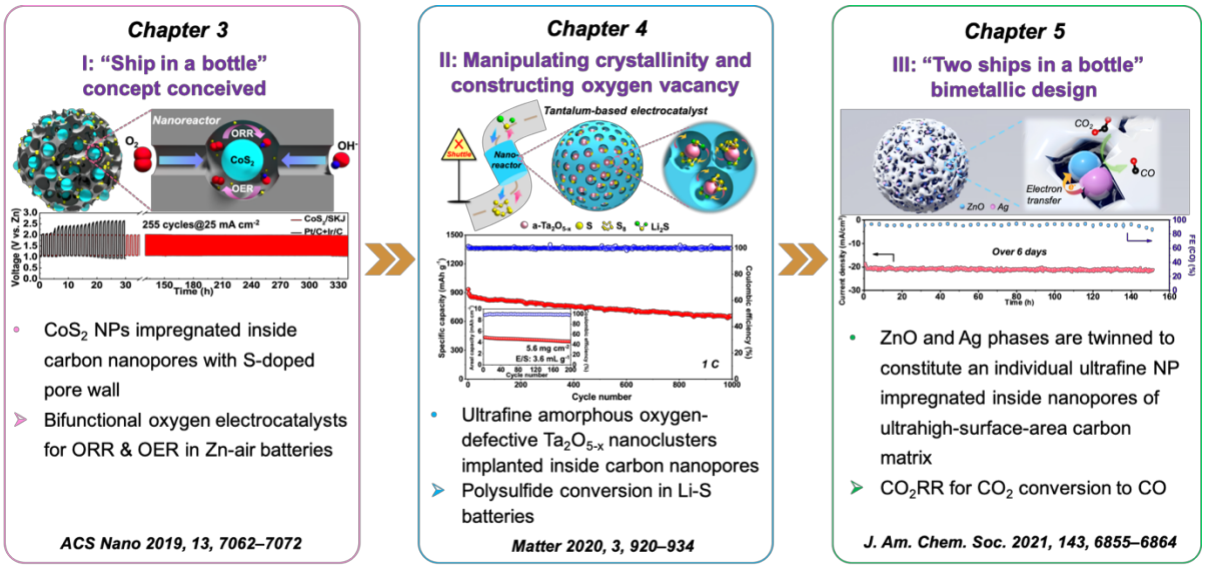

Figure 1.8 Schematic illustration of the research topics throughout this thesis.

Chapter 2 Literature Review of Fabrication Approaches

To rationally engineer advanced electrocatalysts comprising UMNPs impregnated inside the nanopores of porous carbons, it is essential to summarize the key protocols for design and fabrication approaches. The methodologies include two key aspects: i) controlled synthesis of high-surface-area porous carbons, and ii) efficient impregnation techniques of immobilizing UMNPs within porous carbons with clean surfaces.

2.1 Synthesis Strategy of Porous Carbons

In this section, various porous carbons are classified according to their precursors and fabrication strategies for clarity. Within each category, the preparation principles, resulting microscopic morphologies, and pore textures are reviewed.

2.1.1 Conventional Activated Carbons (ACs)

Typically, ACs refer to coal and petroleum pitch-based porous carbonaceous materials, which have long been the most commonly used type of porous carbon. Coal tar pitch is the most common carbon precursor because of its low cost, high carbon content and wide availability from the petrochemical industry, which normally brings about a high carbon yield.[24] However, the main issue of using coal and pitch as the precursors is that their naturally containing impurity minerals often cannot be removed from the carbonaceous product, and these residual elements scarcely contribute to the development of porous structures. Besides, compositions in coal and pitch vary greatly, significantly affecting the properties of the final AC products.[25]

In most situations, ACs are produced with abundant micropores to improve the specific surface area available for practical applications. In a recent study, Shao et al. reported that

carbons synthesized by carbonization and activation of coal tar pitch showed a very high surface area of 3537 m^2 g^{-1}.[26] However, it is difficult to obtain a definite classification of their pore structure because of their innumerous forms and intricate pore features. Usually, all three types of pore sizes (i.e., micropore, mesopore, and macropore) are comprised within one AC product with wide pore size distributions.[27]

2.1.2 Biomass-Derived Carbons

Biomass resources are naturally available and distributed widely all over the world. By virtue of their renewability, high cost-effectiveness and environmental benignity, biomass-derived carbons have attracted great interest and have become promising candidates for electrochemical energy conversion in recent years.[28] A wide range of biomass sources with low economic value can be used as the precursors for carbon materials, such as rich husk,[29] coconut shells,[30] microalgae,[31] and saccharides.[32] The successful conversion of these renewable resources into high-value carbons is normally achieved by pyrolysis and/or carbonization methods followed by an activation process. Details and examples of the individual processes involved in these methods are reviewed in the following subsections.

2.1.2.1 Pyrolysis and Activation. Direct pyrolysis of biomass precursors combined with activation is an effective approach to fabricate porous carbons. For instance, Wang et al. used waste celtuce leaves as the carbonaceous precursors, which were subjected to air-drying and pyrolysis at a high temperature followed by a chemical activation process (Figure 2.1).[33] The obtained carbon products displayed a well-developed porosity with a large surface area of 3400 m^2 g^{-1} and pore volume of 1.88 cm^3 g^{-1}, which were employed as electrode material and adsorption material for high-performance supercapacitors and CO_2 capture, respectively.

Figure 2.1 Synthesis of porous carbons from biomass.[33]

Regarding the pyrolysis conditions, the pyrolysis temperature is the most significant factor affecting the properties of porous carbons. With the rise of temperature, the ash and fixed carbon percentage increase while the volatile matter decreases. As a result, carbonaceous materials produced at a higher pyrolysis temperature normally have a greater quality, though the yields can be reduced owing to the primary decomposition of biomass and secondary decomposition of char residues.[34] In addition, pyrolysis residence time and heating rate, as well as inert gas flow also exert an effect on the pore structure, morphology and yields of carbons.[35]

Direct pyrolysis and carbonization usually lead to carbonaceous materials with less porosity. The activation process, which is a key step to producing well-developed pore structures for adsorption of gas molecules, can be classified into two procedures: physical activation and chemical activation.

(1) Physical activation. The fabrication of porous carbons by physical activation requires high temperature reaction of pyrolytic carbonaceous precursors in a reactive atmosphere with oxidizing gases such as O_2, CO_2, or steam.[36] At high temperatures (800-1100 °C), the oxidizing gases react with the carbon framework partially with the formation of CO or CO_2, enlarging

and opening the incipient pores formed at the prior carbonization step to generate a defined pore structure. In the typical case of steam and CO_2, the involved reaction mechanism is:[37]

$$C + H_2O = H_2 + CO \text{ (steam as the activating agent) (2.1)}$$

$$C + CO_2 = 2CO \text{ (CO_2 as the activating agent) (2.2)}$$

Besides, O_2 was explored as the activating agent by Plaza et al. to prepare porous carbons from olive stones and almond shells.[38] They initially found excessive burn-off and decrease of carbon yield occurred in the activation process, due to the fact that the high exothermic enthalpy makes it difficult to control the reaction temperature and reaction speed of O_2 with carbon. However, by appropriately tuning activation conditions (i.e., O_2 content), the pore size distribution of the carbons can be tuned.

Thermal parameters of physical activation exert significant effect on carbon yields. Specifically, at a higher temperature, more volatile compounds are removed from the carbon framework; the longer activation time enables more oxidizing gases (e.g., O_2, CO_2, or steam) to burn the carbon and organic compound away. These inevitably leads to low total carbon yields but rather high surface areas and pore volumes.[39]

(2) Chemical activation. A wide variety of activating agents have been studied for chemical activation, such as KOH,[40] $ZnCl_2$,[41] H_3PO_4,[41] and K_2CO_3.[42] KOH is the most widely-used among these, due to its ability to efficiently contribute to forming micropores or small mesopores within the carbon framework. The KOH activation process has been investigated by Lillo-Ródenas et al. via temperature programmed desorption (TPD) experiments combined with thermodynamic studies, by which the reaction mechanism was proposed as follows:[43]

$$\sim 400\ ^\circ C: 6KOH + 2C \rightarrow 2K_2CO_3 + 3H_2 + 2K \text{ (2.3)}$$

$$>700\ °C: K_2CO_3 \rightarrow K_2O + CO_2 \quad (2.4)$$

$$K_2CO_3 + 2C \rightarrow 2K + 3CO \quad (2.5)$$

$$K_2O + C \rightarrow 2K + CO \quad (2.6)$$

$$CO_2 + C \rightarrow 2CO \quad (2.7)$$

Therefore, the development of pore structures is attributed to the etching effect toward carbon atoms by oxidation (2.3, 2.5, 2.6) as well as the in situ generated potassium intercalated within carbon layers which could vaporize and penetrate within the carbon matrix to expand the lattice (Figure 2.2).[44] In addition, the generated CO_2 reacts with carbon via the carbon gasification process to further promote the development of porosity (2.7).[40] For instance, Serafin et al. prepared microporous carbons from various biomass precursors (e.g., carrot and kiwi peels, sugar beet pulp, fern leaves) via KOH activation.[45] The resulting carbons possessed high microporosity with a surface area of up to 1593 $m^2\ g^{-1}$.

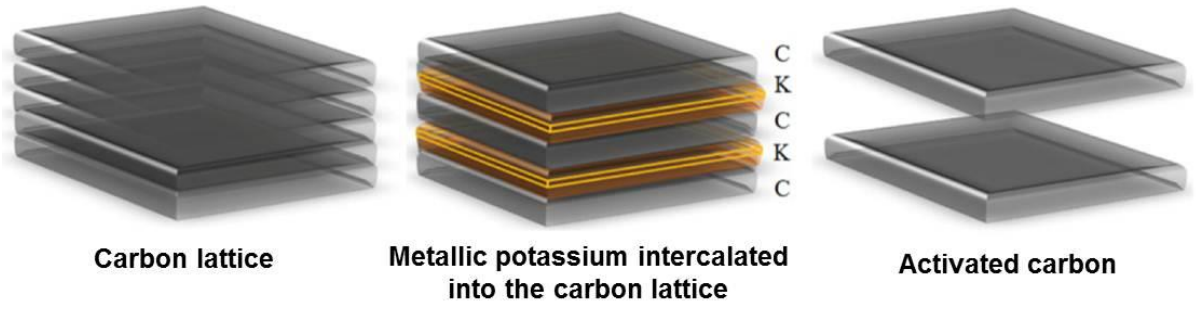

Figure 2.2 Activation mechanism above 700 °C by the penetration of metallic potassium into the lattice of the carbon, the expansion of the lattice by the intercalated potassium, and the rapid removal from the carbon matrix.[44]

However, the conventional KOH-activation method consumes large amounts of alkalis (the typical weight ratio of KOH to precursor is 3-4) via inhomogeneous physical mixing, which easily damages the morphology and structure of carbons. Besides, excessive use of strong

alkalis can result in a corrosive, costly, and risky preparation process that is adverse to large-scale and sustainable production. To this end, I developed a new ionic activation methodology using homodisperse potassium ions as the activating agent to fabricate highly ultramicroporous carbons (Figure 2.3).[46] This work circumvented the use of corrosive alkali activating agents, and more importantly, it offered a route to precisely tune the ultramicroporosity of carbon materials, which achieves an ultrahigh ultramicropore content of 95.5%. Besides potassium-based chemical activation, other reagents were also investigated as activating agents such as $ZnCl_2$ and H_3PO_4.[47] Owing to their small sizes and dehydrating function that facilitate the development of microporosity, the developed carbon materials commonly possess abundant micropores.

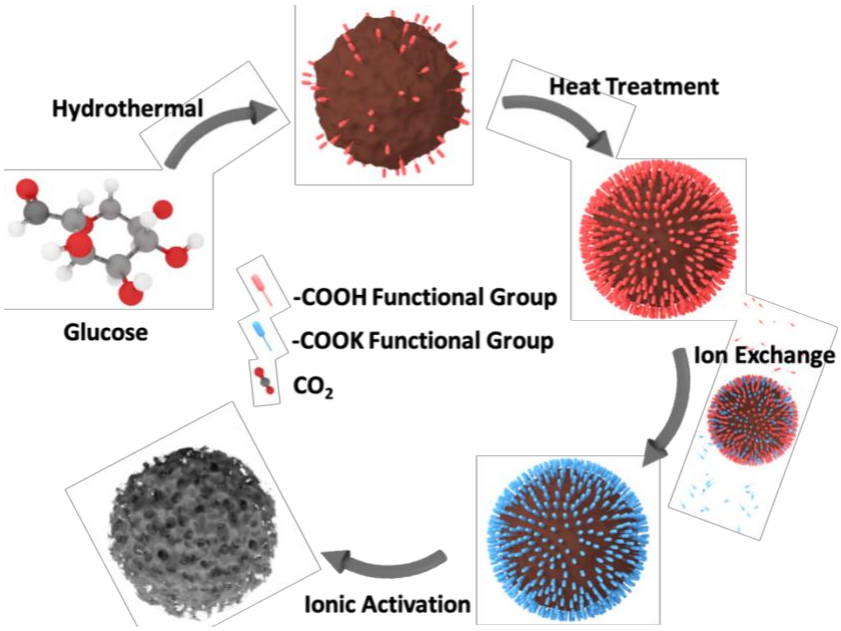

Figure 2.3 Schematic of controlled synthesis of ultramicroporous carbon materials.[46]

Compared to physical activation, chemical activation generally allows the use of lower activation temperatures but maintain an easier adjustment of porosity, delivering a higher final carbon yields. As a general trend for both physical and chemical activation, a rise in activation

temperature results in increased porosity due to the volatilization process but significantly decreased carbon yields. As such, striking a balance between carbon yields and pore texture is crucial for selecting appropriate activation conditions.

2.1.2.2 Sol–Gel Process. In recent years, the sol–gel method has rapidly developed as a direct and facile strategy for fabricating porous carbon materials from renewable biomass, especially for sugar-based resources (e.g., starch and cellulose).[48] "Starbons®" carbon, derived from polysaccharides, is a typical example that possesses highly developed mesopore textures. In particular, the pore volume and size of carbons can be specifically tuned in this methodology.[49] Typically, the sol–gel process comprises three main stages. First, the gelatinization of precursors occurs in water upon heating. Then, a solvent with a lower surface tension (e.g., ethanol) is introduced to substitute the moistures inside the gel. After drying, the obtained porous gel doped with a catalytic amount of acid is subjected to pyrolysis under vacuum, resulting in the generation of highly porous carbons. Robertson and Mokaya reported the successful synthesis of porous carbon materials through a simple subcritical drying route combined with activation process wherein no additional drying steps, sol–gel additives and modifications were required.[50] The obtained highly microporous carbons possessed a surface area up to 1980 $m^2 g^{-1}$ and pore volume up to 2.03 $cm^3 g^{-1}$, with the pore sizes of 0.8 and 1.3 nm.

The sol–gel method has been widely employed in both laboratories and industries, because a relatively high carbon yield can be realized in the practical production, which benefits from the efficient gelatinization and little mass loss in the fabrication process.[51] However, the main hurdle is the rigorous drying process of the wet gel and the long preparation-period. Additionally, in the process of solvent exchange, a slight change may trigger considerable

variations in structure features and properties of the product carbons. Besides, the issue of pore-blocking occurring in gelatinization process also needs to be resolved.[52]

2.1.2.3 Hydrothermal Carbonization. The hydrothermal carbonization (HTC) process has attracted great interest among researchers in recent years. By virtue of its intrinsic features, such as high carbon-efficiency under quite mild reaction conditions (<200 °C), abundant functional groups produced on the surface of the carbonaceous products, environmentally-friendly synthesis without organic solvents or harmful gas emissions involved, HTC is regarded as the most promising approach to convert biomass into high value-added functional carbonaceous materials (Figure 2.4a).[53] Hydrothermally carbonized biomass is usually employed as carbon precursor rather than direct biomass, owing to its higher carbon yield and more homogeneous composition. Carbohydrates, such as glucose,[54] sucrose,[55] starch,[56] and cellulose,[57] have been the most used precursors for HTC processes thus far. Sugars initially dehydrate to form hydroxymethyl furfural (HMF) and furfuryl derivatives, which then undergo complex polymerization (condensation and addition) and aromatization reactions to generate spherical functionalized carbons (Figure 2.4b).[58]

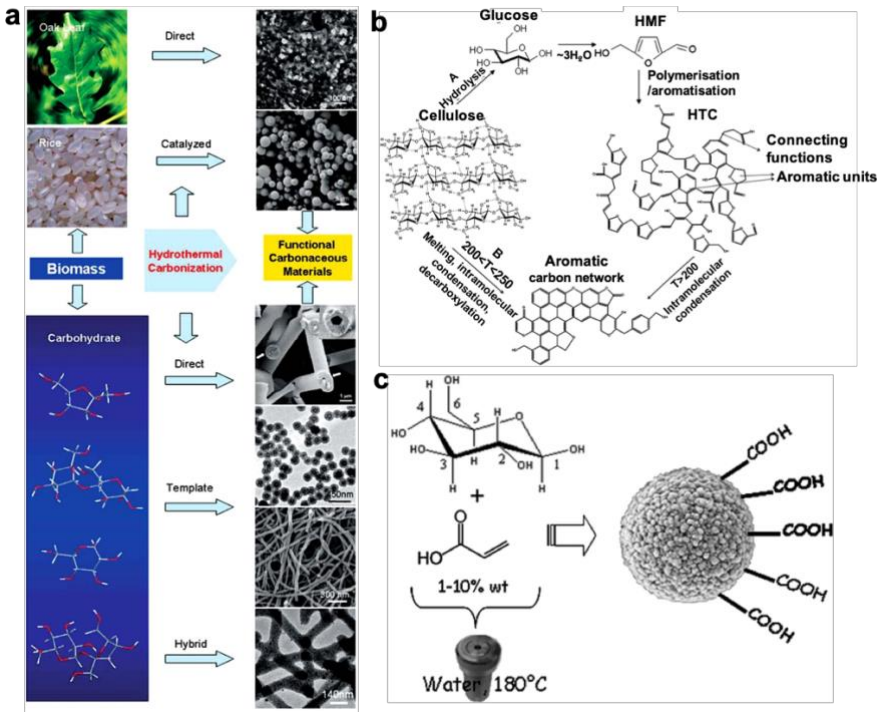

Figure 2.4 (a) Schematic illustration of preparation of various functional carbonaceous materials from biomass (e.g., carbohydrates) via HTC.[53] (b) Conversion of cellulose into hydrochar via (A) HMF resulting in a furan-rich aromatic network and (B) direct aromatization.[58] (c) Synthesis of carbon microspheres loaded with abundant carboxyl.[54]

HTC-derived porous carbons have been widely investigated and applied in energy conversion and gas adsorption. Sevilla et al. developed a range of porous carbons from sustainable biomass resources, which underwent HTC followed by chemical activation.[59] The microporosity of hydrothermally carbonized carbons was significantly increased after the activation process, presenting a large surface area of 2850 m^2 g^{-1}. In addition to the traditional HTC process which produces colloidal carbon spheres using carbohydrates as precursors, the appropriate additives or template can tune the synthesis of new carbonaceous materials with special surface chemical groups and structures. A typical case is the synthesis of carbon

microspheres loaded with rich carboxylic groups by one-step HTC of glucose with the presence of acrylic acid (Figure 2.4c).[54] This work provided a green route to fabricate hydrophilic functionalized carbons with improved water dispersity. Liu et al. further advanced this strategy with chemical activation using carboxylate as the activating agent, which was derived from the carboxyl-rich carbons via HTC, producing abundant ultramicropores (< 0.7 nm) in carbon materials.[60]

2.1.3 Polymer-Derived Carbons

Although fossil resources and biomass are the most frequently used carbon precursors, they are often not the ideal choices for porous carbon material designs due to their complex inorganic components and impurities. Alternatively, the use of synthetic polymers as the precursors offers high carbon yield, more facile control of chemical compositions, and thus achieves precise morphologies, tunable pore structures and easy surface chemistry modification. Increasing research efforts on polymer-derived carbons have been made in recent years, which can be classified into the following categories based on their synthesis methodologies.

2.1.3.1 Hard-Template Method. The hard-template technique (also referred to as nanocasting or exo-templating) has been recognized as an effective method to fabricate carbon materials with tunable pore texture over various length scales.[61] The hard-template method uses a suitable porous solid as the sacrificial scaffold to replicate its structure and porosity after the introduction of a carbon precursor via infiltration techniques (e.g., wet impregnation). After the carbonization process and removal of the template, the product carbon exhibits an inverse replica from the used template.

Kyotani et al. performed the pioneering research on the nanocasting methodology, in which highly microporous carbons with uniform pore sizes (1-2 nm) and desired shapes were obtained by using layered clay minerals and zeolites as the templates.[62,63] Since this advancement, various template materials with accessible porosity together with thermally stable carbon precursors have been extensively investigated, providing further great progress in this area. For instance, porous carbon nitride (CN) spheres were developed by Zhao's group who employed spherical mesoporous cellular silica foams as the hard template and ethylenediamine and carbon tetrachloride as the precursors.[64] The high N content of 17.8 wt% and hierarchical pore structure with pore size distribution at 4.0 and 43 nm were achieved in the CN spheres.

In addition, various solid materials (e.g., colloid crystals and MgO) have been used as hard templates,[65,66] and extended to the multiple-template route. As a classic example, a multimodal porous architecture, which consisted of wormhole-like mesopores (ca. 2.7 nm) and large spherical mesopores (ca. 10 nm) within the walls of 3D ordered macropores (3DOM) (ca. 150 nm), was constructed via a ternary-nanocasting strategy (Figure 2.5).[67] The poly(methyl methacrylate) (PMMA) colloidal crystal was used as a template for generating the 3DOM structure, while colloidal SiO_2 nanoparticles and tetraethyl orthosilicate (TEOS) acted as the template for spherical mesopores and wormhole-like mesopores, respectively. The resulting carbons with such a unique hierarchically porous structure may significantly boost the kinetics for electrocatalysis applications.

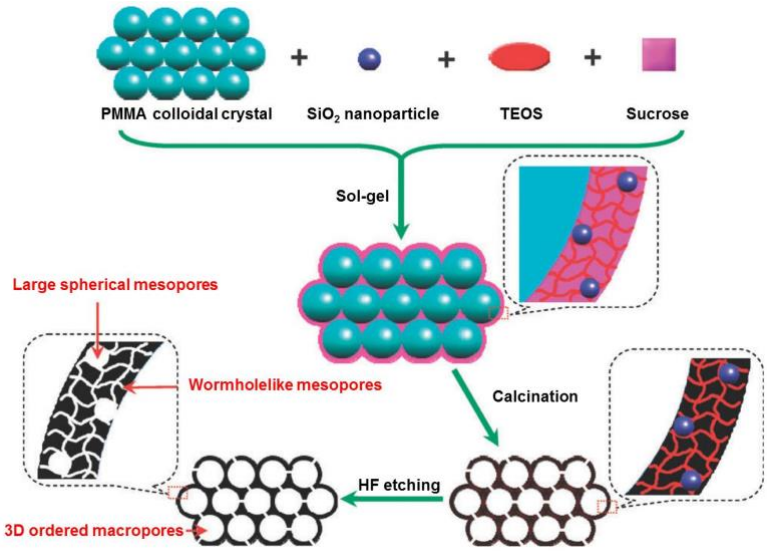

Figure 2.5 Synthesis of hierarchical porous carbons via a ternary-nanocasting strategy.[67]

Using the hard-template method is a route to obtain true negative replicas of template materials, thus likely offering the best porosity control compared to other methods. However, its major hurdles are the tedious preparation process of hard templates, as well as the use of hazardous chemicals (e.g., HF and NaOH) to remove templates, which could bar extensive scaled up usage of the hard-template technique.

2.1.3.2 Soft-Template Method. In comparison with the hard-template method, the soft-template strategy does not employ the synthesis and removal of a hard template. Instead, it constructs supramolecular arrangements of carbon precursor molecules using soft materials as templates, which typically include micelles or vesicles, macro and microemulsions, or polymers, as well as biological molecular assemblies.[68] Benefiting from the advantage that the template can be either consumed or destroyed during the carbonization process, and thus no chemical etching-off is involved, the soft-template method has been demonstrated as an

effective route to precise pore engineering toward multi-modal pore architecture and targeted surface/bulk functionalization for efficient electrocatalysis.[69]

Inspired by the pioneering works from Dai's group,[70] Zhao's group,[71] and Nishiyama's group,[72] research advancements of soft-template-derived porous carbons have been developed rapidly. For instance, a novel and facile self-assembly strategy based on benzoxazine chemistry was reported by Lu's group.[73] The obtained porous carbon monoliths possessed multiple-length-scale porosity (micro-, meso-, and macropores) and a N-containing framework (Figure 2.6a).

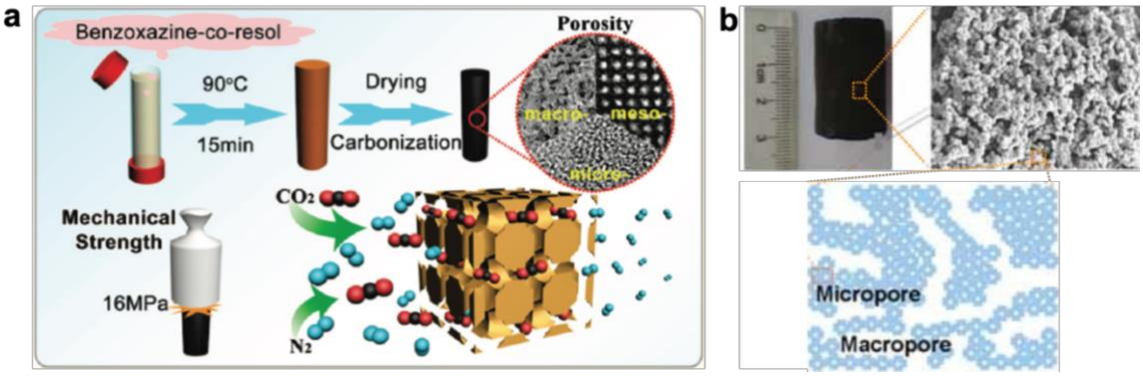

Figure 2.6 (a) Synthesis of porous carbon monoliths with multiple-length- scale porosity via a self-assembly strategy.[73] (b) Carbons fabricated via a template-free strategy, with a hierarchical porosity comprising macropores and micropores.[74]

In general, the soft-template method is relatively simple and applicable for fabricating porous carbons with complex structures, porosities as well as surface functionalities. However, this strategy entails a strong self-assembly ability that can withstand high-temperature thermal treatment (i.e., carbonization). The main challenges of the soft-template technique are low yield, limited choices of soft-template materials, and relatively high cost, meaning that its prospect for scale-up is still economically and environmentally questionable.

2.1.3.3 Template-Free Method. The template-free fabrication strategy utilizes sol–gel chemistry to obtain cross-linked organic gels from the molecular precursors. Motivated by the pioneering work of Pekala, who processed surface-functionalized polymer "clusters" derived from the polycondensation of resorcinol with formaldehyde to produce organic aerogels,[75] remarkable progress in advanced polymerization systems and surface functionalization has been made recently.[76,77] For instance, Zeng et al. developed a template-free route to fabricate hierarchical porous carbons via building intra- and inter-sphere carbonyl (–CO–) and $–C_6H_4–$ crosslinking bridges between polystyrene chains.[78] In addition, synergic assembly/copolymerization between carbon precursors and modifiers with heteroatom-containing groups can lead to the direct synthesis of functional carbons with significantly improved CO_2 capture performance.[79] Recently, Hao et al. prepared a new type of N-doped porous carbon monolith via a template-free strategy.[74] By employing sol–gel copolymerization of formaldehyde, L-lysine, and resorcinol, the resulting product carbons possessed hierarchical porosity consisting of both macropores and micropores (Figure 2.6b). The macropores could supply sufficient diffusion space for mass transport while micropores could serve as the ideal trapping sites toward reactants and intermediates, expediting the electrocatalytic kinetics. In addition, Sun's group recently reported a unique methodology which linked mesitylene, a representative heavy carbon by-product in the course of C1 chemical technologies, with flexible methylene groups to imitate the biomass-based macromolecules as the carbon precursor.[80] The developed carbons present large hierarchical porosity. This work endows mesitylene-based polymer with great potential as applicable carbonaceous precursor, enriching the big family of polymer-derived carbons.

The template-free synthesis strategy circumvents the use of any hard or soft templates, thereby delivering a relatively high cost-performance ratio. Therefore, exploring facile and efficient template-free methodologies should be continued to further develop various types of low-cost porous carbon materials for efficient and durable electrocatalysis applications.

Among the aforementioned three strategies used for fabricating polymer-derived carbons, soft-template and template-free method normally have high yield of carbon conversion. For example, using deep eutectic salts either as solvents, or as carbonaceous precursors and structure-directing agents, Monte's group prepared carbon monoliths with high yield (80 %) and tailored mesopore diameters.[81] In contrast, the use of hard-template method brings about a relatively low carbon yield because of the collapse of the carbon after etching off the template.

2.1.4 Metal-Organic-Framework-Derived Carbons

Metal organic frameworks (MOFs) have attracted great research interests as a new class of crystalline porous materials. Benefiting from the high carbon content in the organic ligands, MOFs can function as both carbon precursors and templates simultaneously. Porous carbon materials can be obtained via the direct carbonization of MOFs, which normally present nanopores of a precise and uniform size.[82]

With the use of pristine components, it is possible to tune the structural and chemical properties of MOFs to engineer an efficient electrocatalyst. Modifying the pore texture and surface chemistry is crucial to promote the electrocatalytic performances. For instance, isoreticular metal organic frameworks (IRMOFs), which are formed by bridging organic linking groups (e.g., pyridyl and carboxylate) with metal nodes via strong coordination bonds,

deliver a tunable pore size in the 3D organic–inorganic network.[83] IRMOFs modified with C_3N_4 were reported to exhibit a superior catalytic activity in alkaline electrolytes for ORR.[84]

One particular merit of MOF-derived carbons is that the morphology of MOFs can be facilely retained in the carbons, which provides more possibilities for the template-synthesis strategy to produce porous carbon materials. For example, the nanoporous carbons fabricated by a nanocasting pathway present prominent surface area of 4000 m^2 g^{-1} and finely tunable microporosity from 0.5 to 1.5 nm (Figure 2.7).[85] Zou's group investigated the effect of MOF functional ligands and topological structures on product carbons separately prepared from three kinds of ZIFs including ZIF-8, ZIF-68 and ZIF-69.[86] They concluded that the pore chemical environment and local structure play a crucial role in gas adsorption and capacitor behavior. The controlled carbonization of MOFs paves an avenue to fabricate hierarchically porous carbon materials, which shows great potential in material science and electrochemical energy research.

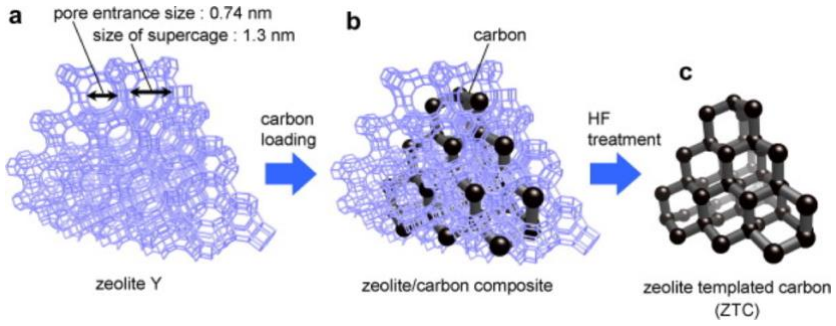

Figure 2.7 Synthesis of nanoporous carbons via the nanocasting method. (a) Crystal structure of the zeolite Y template and (b) illustration of the zeolite/carbon composite. Impregnated carbon is shown using a black framework and (c) framework structure of the liberated ZTC after HF washing.[85]

2.1.5 Graphitic Carbons

The porous carbon materials prepared by the previously discussed methods generally possess an amorphous nature with highly disordered and complicated structures. These amorphous carbons, which are composed of long-range randomly arranged stacked-carbon fragments, have lots of defects, curvatures, and edges.[87] In contrast, graphitic carbons possessing a high graphitization degree have also been widely investigated and are valuable for studying electrochemical behavior because of the ordered arrangement at the atomic scale. Various allotropes of nanoscale graphitic carbons are discussed in this subsection, including 3D graphite, 2D graphene, 1D carbon nanotubes, and 0D carbon fullerenes.

2.1.5.1 3D Bulk Crystalline Carbons. Graphitic carbons normally refer to soft carbons (i.e., graphitizable precursors) heated above 2000 °C. When the heating temperature reaches above 3000 °C, the well-known "turbostratic disorder" tends to disappear monotonically with the formation of graphite at this stage. Conceptually, graphite is a graphitic carbon with no or very little turbostratic disorder. Although the high-temperature heat treatment promotes the transition toward the graphitized phase, it may lead to the collapse of pore architecture, decreasing the accessible surface area. Fortunately, by using graphitization catalysts and/or modified processing techniques, graphitic porous carbons can be obtained under lower temperature conditions. Xing et al. developed a nanoporous graphite with a high degree of local crystallinity via the magnesiothermic reduction of CO_2 below 700 °C with the use of Cu as a catalyst.[88] By this strategy, both a highly graphitic structure and a high surface area are realized in a single carbon material. In another case, Lee's group reported an innovative and efficient strategy to achieve full graphitization by modified microwave heating with the help of a metal catalyst.[89] Using this method, amorphous carbons can be transformed into crystalline

graphite in an extremely short period of 5 min. The developed microwave graphitization is much more efficient, in terms of both energy and time demand, than the currently used industrial graphitization method, and thus this methodology has the potential to revolutionize the graphite industry. Another pioneering work was performed by Dai's group,[90] who developed ordered graphitic mesoporous carbons with tunable mesopore sizes via a "brick-and-mortar" self-assembly method at a relatively low temperature without the use of graphitization catalysts.

In addition, heteroatom-modification on a graphite split pore can effectively tune the adsorption energy between reactant molecules and the graphitic surface, thus further significantly improving its electrocatalytic activity and selectivity.[91] This provides more possibilities and routes to design high-performance graphitic carbon catalysts.

2.1.5.2 2D Carbons. The discovery of graphene has opened up an exciting new field in the science and engineering of 2D nanomaterials.[92,93] As a one-atom-thick allotrope of the carbon family containing strong sp^2-bonding in a honeycomb lattice, graphene possesses a range of unusual properties, such as high mechanical strength, relative inertness, impermeability to all standard gases, and a large theoretical surface area of 2630 $m^2\ g^{-1}$.[94] Graphene also essentially unfolds infinite possibilities for functionalization and modification of its carbon backbone to produce chemically modified graphene (CMG).[95] As such, these properties endow graphene-based 2D materials with great potential for new energy technologies.[96,97]

Graphite oxide (GO) is a graphene derivative comprising abundant O-containing functional groups on the edges and planes. Modification of the GO functional groups with amine-containing molecules can be easily achieved via the nucleophilic substitution reaction.[98] The

amine groups embellished GO can break the electro-neutrality of carbon to create positively charged sites and hold promise for various electrocatalytic systems. Moreover, high-surface area graphene oxide derived carbons (GODCs) were developed by Srinivas et al. who employed exfoliated graphene oxide as precursors treated through a KOH activation.[96] In the tunable synthesis, a surface area of 1900 m^2 g^{-1} and total pore volume of 1.65 cm^3 g^{-1} could be obtained, evidencing that producing highly porous carbon materials from a GO precursor is a viable strategy.

Inventively, Koenig et al. developed a new graphene membrane-based molecular sieve.[99] In this strategy, pores were generated in micrometre-sized graphene platelets by ultraviolet-induced oxidative etching, and the transport of gas molecules passing through pores was measured by both a pressurized blister test and mechanical resonance. By investigating various gases (CO_2, CH_4, H_2, N_2, Ar, and SF_6), this work demonstrated the efficient gas separation behavior of graphene membranes by molecular sieving, and presented a significant progress for realizing size-selective porous graphene membranes.

2.1.5.3 1D Carbons. Another relatively new member of the carbon family is carbon nanotubes (CNTs). Since the first synthesis of CNTs via arcing between graphite-like electrodes by Iijima in 1991,[100] 1D carbon materials have spurred intense research enthusiasm. By virtue of their extraordinary features such as unique pore structure and excellent thermal and mechanical stability, CNTs have been extensively studied in various fields.[101][102] One potential application is acting as the catalysts for oxygen electrocatalysis, owing to their facile functionalization, reduced size, as well as easy integration with extraneous active groups for efficient ORR.[102] Another representative example is the development of bundles of double-walled carbon nanotubes (DWCNTs) with inner diameter of 8 nm and different inter-tube

distances, which were employed for CO_2 capture by Rahimi et al.[103] Through the tunable synthesis, they found that reducing the inter-tube distance could result in a prominent increase in CO_2 adsorption capacity at ambient pressure. This work provided an instructive guideline to design multi-walled CNTs. Besides, performing rational surface modification of CNTs provides an alternative effective strategy to modulate the electron configuration of carbon atoms and improve their potential for electrochemical energy conversion and storage.[16,104]

Besides CNTs, other 1D carbon nanostructures have also been extensively reported such as carbon nanofibers,[105] carbon nanoribbons,[106] carbon nanoscrolls.[107] These 1D carbons enrich the massive carbon family and more importantly, their wide variety of physical properties hold great promise as favorable carbon materials for energy and environment applications.

2.1.5.4 0D Carbons. Fullerene is the representative 0D allotrope of carbon, representing the first known type of molecular solid comprising exclusively carbon, with the archetypes being C_{60} and C_{70}. The fullerene structure comprises carbon atoms clustering into closed cages, each of which constitutes a single molecule.[108] In the solid state, these pseudospherical molecules arrange in turn into different crystal structures, exemplified by a face-centered cubic structure in the case of C_{60}.[109] Fullerene has been extensively studied in various electrochemical energy systems such as Li-ion batteries,[110] Na-ion batteries,[111] flow batteries,[112] fuel cells,[113] and oxygen electrocatalysis (ORR & OER) in metal−air batteries.[114]

In recent years, heteroatom-decorated C_{60} fullerene has been a popular topic. For example, Gao et al. investigated the ORR on N-decorated fullerenes via the first-principles spin-polarized density functional theory (DFT) calculations.[115] Compared to the pristine fullerene, N-doping into C_{60} was found to facilitate O_2 adsorption on the N-C complex sites. When the

surface of C_{60} were embellished with N atoms, they found that N-C sites could significantly reduce not only the activation energy barrier of O_2 molecules but also the energy barrier of limiting-rate step in ORR. As another typical example, B-doped C_{60} fullerene was studied for lithium storage by means of the first-principle DFT calculations, in which a single C atom was substituted by a B atom.[116] It was found that there was a substantial increase in redox potential in the $C_{59}B$ system, demonstrating that the spin state is crucial to be considered to understand the relationship between electronic structure and redox properties. In this regard, introducing extra electrons to the fullerene system (i.e., e^--charged state) has been proven to be an effective strategy to tune the interactions with foreign molecules. This potentially would improve the electrocatalytic performance, and therefore the heteroatom-decorated e^--charged fullerene structure could serve as a promising electrocatalyst.

2.2 Impregnation Methods and Strategies

To make the most of the powerful confinement effect of nanopores, efficient impregnation of the metal precursors into the pores of porous matrices is pivotal to obtain encapsulated UMNPs with stable electrocatalytic behavior. The impregnation methods and strategies will be presented in this section.

2.2.1 Incipient Wetness Method

This approach is one of the most extensively used impregnation techniques to fabricate heterogeneous catalysts, which can be readily scaled up for industrial production.[117,118] Typically, the precursor solution is prepared by dissolving metal precursor in an aqueous/ organic solvent. When the defined amount of precursor solution, whose volume is equal to or less than the total pore volume of the porous support, is added to the porous support, capillary

force results in the impregnation of precursor into the pores. The subsequent reduction reaction with reductants (i.e., $NaBH_4$ solution and H_2 gas) produces UMNPs within the pores of porous support. With this approach, it is feasible to control the metal loading by tuning the concentration of precursor solution. Nevertheless, this method meets several potential issues. Partial metal precursors could be adsorbed on the external surface of the support due to the diffusion-resistance difference between internal and external surface, resulting in partial aggregation of MNPs.[13]

2.2.2 Chemical Vapor Deposition (CVD)

Another promising approach for the impregnation of UMNPs in porous supports is the solvent-free CVD technique, which combines successive reduction treatment or facile thermal decomposition.[119] Typically, the porous support and a volatile organometallic precursor are placed separately in a sealed tube furnace. The gas-phase precursor can be infiltrated into the pores of support by means of sublimation at a specific temperature that depends upon the vapor pressure of the precursor. This approach enables the synthesis of UMNPs within a wide range of organic and inorganic supports to produce efficient heterogeneous catalysts. However, because of the mobility of the primary metal nuclei or clusters, the diffusion of MNPs to the external surface could occur, leading to a broad range of MNPs dispersity and inefficient control of the metal loading. The CVD approach is also restricted by the vapor pressure of metal precursor and mass-transport-limited kinetics. In addition, the high precursor volatility normally demands the use of expensive and toxic carbonyl or fluorinated metal compounds, potentially causing adverse effluents.[13]

2.2.3 Double-Solvent Method

The double-solvent method can enable a quantitative impregnation of UMNPs inside porous support with hydrophilic pores, which is based on the immiscibility of the hydrophilic solvent and hydrophobic solvent.[120,121] When a hydrophilic precursor solution with a specific volume (smaller than the adsorbent pore volume) is slowly added to a hydrophobic suspension of the adsorbent under vigorous stirring, the well-dispersed precursor droplets completely diffuse into the hydrophilic pores of the adsorbent, notably minimizing the deposition of metal precursor on the external surface.[122] By combining with further reduction/pyrolysis treatment, this approach is capable of generating well-immobilized UMNPs within pores of porous support in a controllable and reproducible manner, effectively avoiding the MNPs agglomeration on the outer surface. However, this approach is only applicable to the support with hydrophilic pores, such as MOFs and silica.[13]

2.2.4 Solvent-Free Solid Grinding

Another impregnation method is solvent-free solid grinding of the porous support with a volatile organometallic metal precursor that possesses sufficient vapor pressure at room temperature. This method was initially proposed by Ishida et al.,[123] and now is widely used as a facile and efficient approach to immobilize UMNPs into the porous support. During grinding, the sublimated vapor of the metal precursor is readily infiltrated into the support pores, resulting in the uniform distribution of the metal precursor. UMNPs implanted inside the support can shape via the treatment of adsorbed species with reactive gas, for example, H_2. Nevertheless, this approach has a great limitation on the selection of metal precursor. So far, only dimethyl Au(III) acetylacetonate, which has a vapor pressure of 1.1 Pa at room temperature, has been employed as the metal precursor via this method.[124,125]

Chapter 3 “Ship in a Bottle” Design of Efficient Bifunctional Oxygen Electrocatalysts for Long-Lasting Rechargeable Zn−Air Batteries

3.1 Introduction

The recognition of global overconsumption of fossil fuels and associated environmental deterioration has spurred a strong imperative for the development of next-generation sustainable energy storage and conversion systems.[126,127] The urgency is to develop inexpensive renewable energy storage technologies with high energy densities to reduce dependence on conventional fossil fuels. Rechargeable metal−air batteries are attracting renewed interest as a promising energy storage system because of the high energy density and enhanced safety as well as environmental compatibility.[128] In particular, a Zn−air battery can theoretically store energy of as much as 1086 Wh kg^{-1}, up to 4 times higher than currently widely used lithium-ion batteries. The attractive energy density is derived from an open-cell configuration wherein a zinc anode is coupled with an air-breathing cathode that uses oxygen in atmospheric air as fuel for the electrochemical reactions.[129,130] However, their widespread practical applications are largely hindered by the unsatisfactory rechargeability (i.e., lifetime) and low energy conversion efficiency, which mainly stem from the challenges encountered at the air cathode with sluggish kinetics and poor electrochemical stability for the repeated ORR and OER.[131,132] Therefore, the development of efficient and durable bifunctional electrocatalysts for both ORR and OER plays a pivotal role. Up to now, noble-metal electrocatalysts, such as platinum (Pt) and iridium (Ir), have been intensively investigated and recognized as the most highly active electrocatalysts for ORR or OER.[133] Unfortunately, their

high cost, unsatisfactory catalytic bifunctionality, and stability inevitably preclude their widespread applications.[134,135]

Non-precious-metal based materials hybridized with carbon have become promising candidates for high-performance Zn−air batteries.[136,137] Recently, numerous synthesis strategies have been reported, mainly including metal deposition onto carbon-based supports or carbon coating on metal particles.[22,138] However, the former method cannot efficiently immobilize metal nanoparticles and control their growth during synthesis and even catalytic reactions, which may cause the loss or aggregation of nanoparticles and thus degrade their electrocatalytic durability and performance. Although the latter method can form a carbon-sealed confined space for metal-based particles, the absence of high and uniform porosity for sufficient mass transfer, as well as inefficient control of nanoparticle size and structural change due to poor consistency of the carbon-coating thickness, lead to limited electrocatalytic performance. Furthermore, numerous advantages of the carbon support should be exploited beyond its role as a nanomaterial carrier, which potentially include defect-induced modification and synergistic effects for enhanced electrocatalytic performance.[139,140] Therefore, a rational structural design combined with defect engineering is critical to achieve a high bifunctional catalytic activity with enhanced durability.

Herein, a “ship in a bottle” nanocatalyst design based on fine pyrite-phase transition metal dichalcogenide nanoparticles rooted inside defective carbon pores is proposed. The pores function as individual nanoreactors that are interconnected with one another, in which oxygen catalysis efficiently proceeds under the steric pore environment. As a proof-of-concept, cobalt pyrite (CoS_2) was selected as a model material because of its abundance and intrinsically conductive metallic nature.[141] This design delivers multiple advantages: (i) the nucleation of

CoS_2 nanoparticles is controlled due to the spatial confinement effect of the carbon pores, which not only restricts nanoparticle overgrowth to guarantee a high surface-to-volume ratio and increase numbers of exposed catalytic sites but also prevents nanoparticles from aggregating during catalysis, solving the long-term issue of nanocatalyst stability; (ii) the inter-penetrating and interconnecting porous carbon framework builds up a 3D conductive architecture as the nanoreactor to provide a "highway" for electron and mass transfer and facilitate fast catalytic kinetics; and (iii) the synergistic coupling effects between defect-rich interfaces and chemical bonding derived from sulfur doping boost the catalytic activity and prohibit the detachment of nanoparticles. The resultant catalyst presents a superior bifunctional electrocatalytic activity and durability toward ORR and OER and demonstrates excellent performance and long-term cyclability in the rechargeable Zn−air battery.

3.2 Experimental Section

3.2.1 Materials Synthesis

Preparation of CoS_2/SKJ: Ketjen Black EC600JD (KJ) was purchased from MTI Corporation, China. The other chemicals were purchased from Sigma-Aldrich and of analytical grade without further purification. In a typical synthesis, 80 mg KJ carbon with adsorbed water vapor was placed inside a fused quartz tube under ammonium gas flow for several minutes at room temperature. Subsequently, the sample was immersed into saturated cobalt(II) acetylacetonate/ethyl acetate solution for 10 h. Then, the solid sample was filtrated and washed with ethyl acetate several times. After drying at 80 °C for 8 h, the collected sample was transferred to the center of a tube furnace. An alumina boat containing 2 g of sulfur powder was placed at the farthest upstream position in the tube furnace. The tube was purged of air

with a steady flow of argon gas at 30 sccm, and the sulfurization process was performed at 400 °C for 2 h, resulting in the formation of the CoS_2/SKJ sample.

Preparation of CoS_2+SKJ: KJ was first mechanically mixed with commercial CoS_2 nanoparticles with the same CoS_2 content as CoS_2/SKJ. Then, the as-prepared sample underwent the above sulfurization process to obtain CoS_2+SKJ.

Preparation of SKJ: KJ carbon was directly subjected to the above sulfurization process to produce SKJ.

3.2.2 Materials Characterization

Microscopic morphology, energy-dispersive X-ray spectroscopy (EDS), and electron energy loss spectroscopy (EELS) data of materials were collected by scanning electron microscopy (SEM) using an FEI Quanta FEG 250 ESEM microscope and transmission electron microscopy (TEM) using a JEOL 2010F TEM and high-angle annular dark-field scanning transmission electron microscopy (HAADF-STEM) equipped with a large solid angle for high X-ray throughput, scanning, scanning and transmission, and a Gatan imaging filter for energy filtered imaging. X-ray diffraction (XRD) was carried out using a Rigaku MiniFlex 600 X-ray diffractometer equipped with a Cu Kα irradiation. To collect Raman spectra, a 532 nm laser source was employed. The Thermal Scientific K-α spectrometer was used to collect X-ray photoelectron spectroscopy (XPS) spectra. Thermogravimetric analysis (TGA) was performed on a TA Instruments Q500 under air atmosphere. Nitrogen adsorption−desorption isotherms were measured at liquid nitrogen temperature (−196 °C) by using the Micromertics ASAP 2020 analyzer; the Brunauer−Emmett−Teller (BET) equation was used to calculate the specific

surface area, and the Barrett−Joyner−Halenda (BJH) method was employed to determine the pore size distribution.

3.2.3 Electrochemical Measurements

The electrocatalytic performance was investigated using an electrochemical workstation (Biologic VSP 300) with a three-electrode configuration and rotating disk electrode (RDE). A glassy carbon electrode and a graphite rod were used as the working and counter electrodes, respectively. All of the results were obtained with reference to a saturated calomel electrode (SCE) followed by the calibration to the reversible hydrogen electrode (RHE) based on the Nernst equation: $E_{RHE} = E_{SCE} + 0.059 \times pH + 0.241$. The homogeneous catalyst ink was prepared by dispersing 2 mg of catalyst into 500 μL of 0.3 wt % Nafion ethanol solution under ultrasonication for 30 min. Then, a loading of 0.26 mg cm^{-2} was achieved by pipetting 13 μL of ink on GC surface. The commercial Pt/C and Ir/C catalysts were also prepared via the same procedure as respective ORR and OER benchmarks. The calculation of the electron-transfer number per oxygen molecule is based on the Koutecky-Levich (K-L) equation: $\frac{1}{j} = \frac{1}{j_k} + \frac{1}{B\omega^{1/2}}$, where j_k is the kinetic current and B is Levich slope: $B = 0.2nFD_0^{2/3}C_0v^{-1/6}$ (n is the number of transferred electrons, F is the Faraday constant, D_0 is the oxygen diffusion coefficient of 1.9×10^{-5} cm^2 s^{-1}, C_0 is the oxygen saturated concentration of 1.1×10^{-6} mol cm^{-3}, and v is the kinematic viscosity of 0.01 cm^2 s^{-1}).

3.2.4 Assembly of Zn−Air Batteries

The prototypes applied an open-cell configuration, which contain catalyst-sprayed gas diffusion layer (GDL, SGL Carbon 39 BC, Ion Power Inc.) with a catalyst loading of 1.0 mg cm^{-2} acting as the air electrode and a polished high-purity (99.99%) zinc plate acting as the

anode. The potassium hydroxide solution plus zinc acetate solution was filled into the prototypes as electrolyte and supplemented regularly. For comparison, the mixture of commercial Pt/C and Ir/C catalysts (1:1 mass ratio) was also sprayed on GDL with the same fabrication process as the performance benchmark. The battery testing was performed on a Land tester (Land Electronic Co., Ltd., Wuhan) under ambient atmosphere.

3.3 Results and Discussion

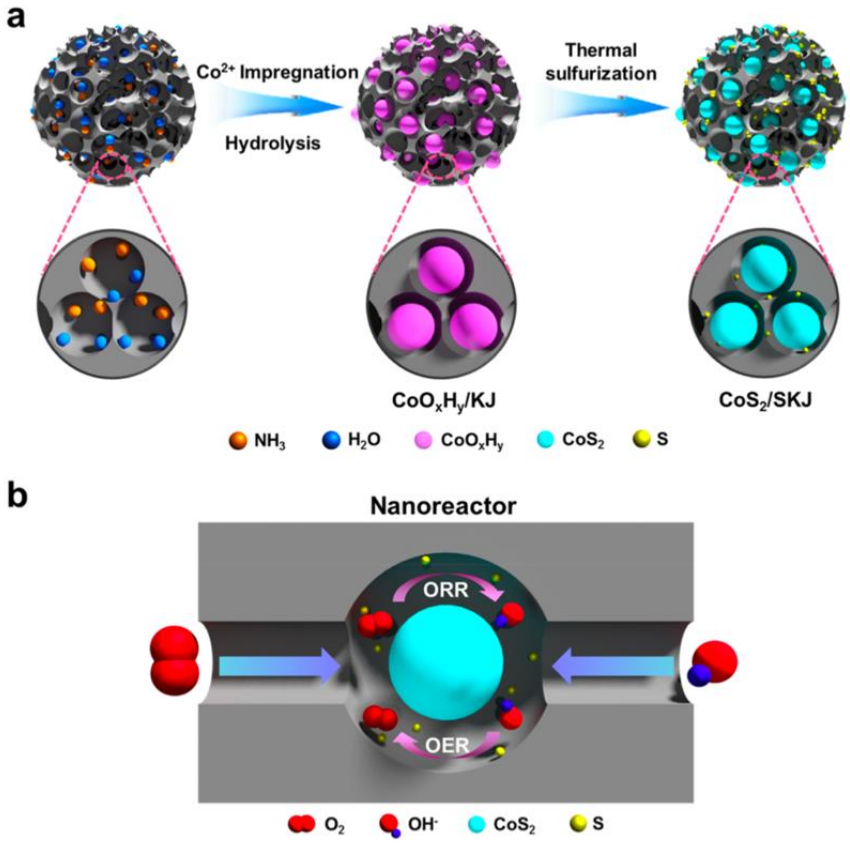

Figure 3.1 Schematic illustration of (a) the synthesis route of CoS_2/SKJ and (b) the individual pore acting as the nanoreactor for oxygen electrocatalysis.

A facile and universal impregnation strategy to achieve the recessed growth of CoS_2 nanoparticles inside heteroatom-doped, defective carbon pores is illustrated in Figure 3.1a. KJ

carbon with adsorbed water vapor and ammonia functions as a porous built-in reaction host, whose microscopic morphology is shown in Figure 3.2a-d. After KJ carbon was soaked in cobalt(II) acetylacetonate organic solution, the cobalt precursor is hydrolyzed inside the carbon pores under the alkaline environment derived from absorbed ammonia. Following this, the cobalt-hydrolyzed product undergoes thermal sulfurization, yielding the final product, in which CoS_2 is immobilized inside the S-doped, defective carbon pores (CoS_2/SKJ). Each individual pore acts as a nanoreactor, interconnecting with each other for efficient oxygen electrocatalysis, as illustrated in Figure 3.1b.

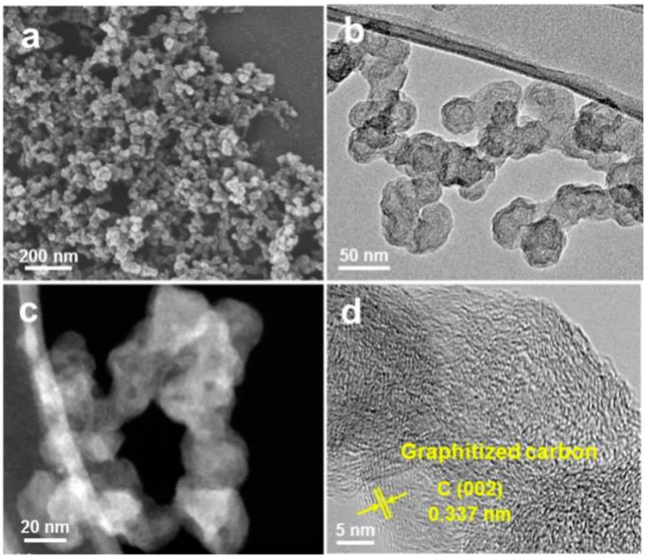

Figure 3.2 (a) SEM, (b) TEM, (c) HAADF-STEM, (d) HRTEM images of KJ.

SEM imaging (Figure 3.3a) reveals a uniform distribution and clean external surface for CoS_2/SKJ. No obvious morphology change is observed compared to KJ (Figure 3.2a), and no agglomeration forms on the external carbon surface, implying successful encapsulation of CoS_2 inside the carbon pores. As shown by the HAADF-STEM imaging (Figure 3.3b), the bright nanodomains are the CoS_2 phase, whereas the dark domains are mainly the C phase from

KJ carbon. The corresponding EDS mapping confirms the presence of Co, S, and C elements in CoS_2/SKJ, and the homogeneous distribution of Co and S demonstrates that abundant CoS_2 active sites are exposed and dispersed uniformly throughout the porous carbon host.

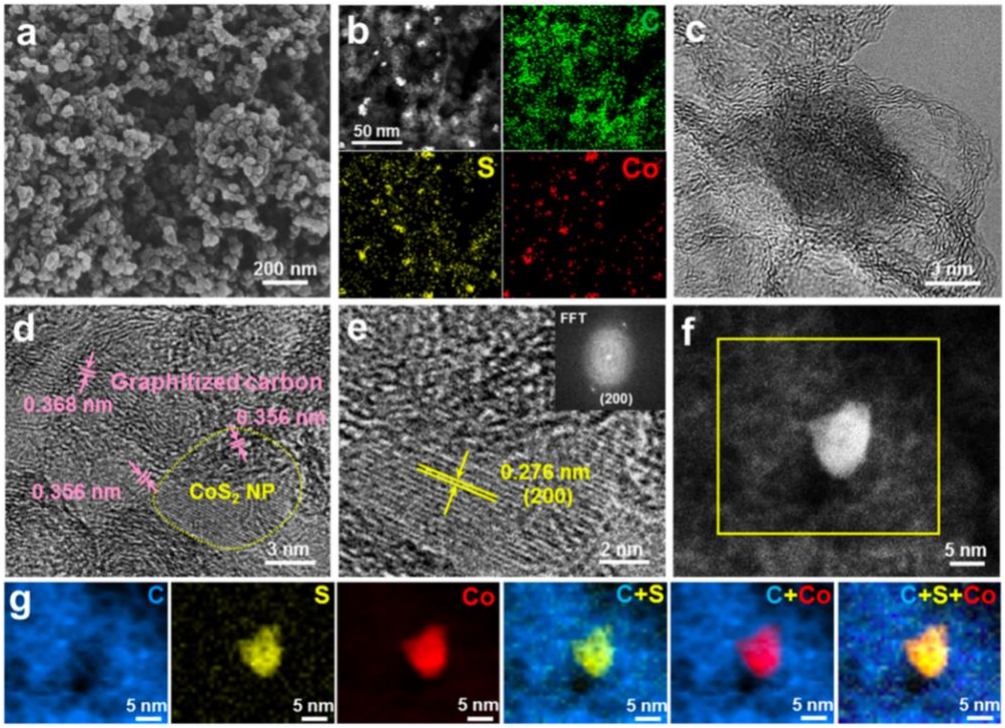

Figure 3.3 (a) Overview SEM and (b) HAADF-STEM images of CoS_2/SKJ as well as corresponding EDS mapping images. (c) TEM image of CoS_2/ SKJ. (d) HRTEM image of graphitized carbon intimately surrounding CoS_2 nanoparticles. (e) HRTEM image and corresponding FFT diffraction pattern. (f) HAADF-STEM image and (g) corresponding EELS elemental mapping and overlaid images of a single CoS_2 nanoparticle immobilized inside carbon pores.

As shown in Figure 3.3c, the high-resolution transmission electron microscopy (HRTEM) image provides explicit evidence that CoS_2 nanoparticles with a particle size of 8.0 nm are embedded in the carbon pores. Importantly, such small nanoparticles were maintained after a

heat treatment at 450 °C because of the carbon pore confinement effect, which deters the CoS_2 nanoparticles from agglomerating even at high temperatures. The HRTEM image in Figure 3.3d reveals that the carbon framework intimately contacted with CoS_2 nanoparticles is highly graphitized, and the graphitization occurs not only around the CoS_2-loaded pores but also throughout the entire composite, building up an interconnected conductive network to offer fast electron transfer. KJ carbon exhibits a typical C (002) facet with a d-spacing around 0.337 nm (Figure 3.2d), while the graphitized carbon in CoS_2/SKJ presents slightly larger d-spacing (Figure 3.3d), which is attributed to the successful S-doping within the graphitized carbon skeleton.[142] It is also noteworthy that the massive porous structures interpenetrate and interconnect with each other, creating a 3D nanoreactor architecture for ion transfer inside and through CoS_2/SKJ, which potentially provides significantly improved kinetics for electrocatalytic processes. The encapsulated CoS_2 demonstrates a high crystallinity of the primary particles, in which the lattice fringes with an interplanar distance of 0.276 nm correspond to the (200) crystal plane of CoS_2, which is evidenced by the fast Fourier transform (FFT) pattern (Figure 3.3e).[143,144] The HAADF-STEM image in Figure 3.3f shows one isolated CoS_2 nanoparticle with a diameter of around 8.0 nm immobilized within carbon pores, confirming the pore confinement effect, which is also reflected in the nanoparticle size distribution (Figure 3.4). As revealed in the corresponding EELS mapping (Figure 3.3g), the S element shows a homogeneous dispersion over the carbon skeleton in addition to the central CoS_2 phase, indicating the successful S-doping. The central-domain distribution of Co suggests the sole existence of intact cubic CoS_2.

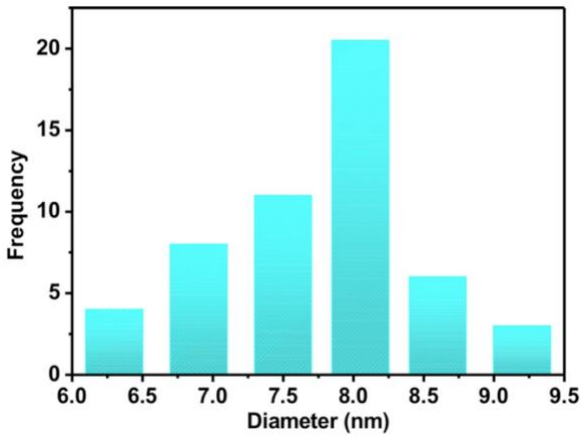

Figure 3.4 Size distribution of CoS_2 nanoparticles immobilized inside carbon pores as measured by HAADF-STEM imaging.

These results validate the encapsulation of immobilized CoS_2 into the interior pores of the S-doped carbon host. The morphology of commercial CoS_2 is shown in Figure 3.5a and b. For comparison, a control composite was prepared by mechanically mixing KJ with commercial CoS_2 followed by the same thermal sulfurization process (denoted as CoS_2+SKJ). Without the pore confinement effect, CoS_2+SKJ displays much larger CoS_2 particles with a diameter of 200 nm compared to CoS_2/SKJ (Figure 3.5c and d). Besides, obvious agglomeration occurs in CoS_2+SKJ, leading to a non-uniform distribution of CoS_2 and KJ carbon.

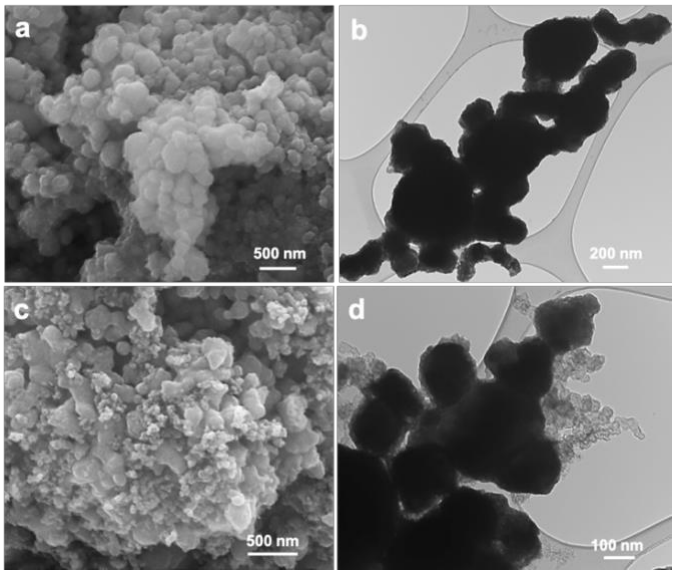

Figure 3.5 (a) SEM and (b) TEM images of commercial CoS_2. (c) SEM and (d) TEM images of CoS_2+SKJ.

The crystalline nature of the as-prepared materials is revealed by the XRD (Figure 3.6a). All the peaks can be unequivocally attributed to cubic CoS_2 with the space group $Pa\bar{3}$ (205) (JCPDS 41−1471),[141] confirming that the cobalt precursor was thermally sulfurized into cobalt sulfide. The crystal domain size of CoS_2 along the (200) direction is calculated to be 8.3 nm via the Scherrer equation, which coincides with the results observed in HRTEM. Moreover, the peak at 23.8° corresponds to a typical carbon (002) plane,[145] and its intensity in CoS_2/SKJ slightly decreased compared with that in KJ. This change reflects the weakened graphitic crystallinity, and correspondingly numerous defects along the (002) direction that were likely formed as a result of S doping in the carbon skeleton.[88] In addition to the XRD results, the existence of CoS_2 is also confirmed by the characteristic peak at 670 cm^{-1} in the Raman spectra for CoS_2/SKJ (Figure 3.6b).[146] The Raman spectra of both KJ and CoS_2/SKJ show two scattering peaks located at around 1340 and 1590 cm^{-1}, which can be assigned to the disorder-

induced D band with a A_{2g} vibration mode of a defective C_6 ring, and G band with a E_{2g} mode of sp^2-bonded C atoms, respectively.[46,147] The D/G intensity ratio (I_D/I_G) of CoS_2/SKJ is higher than that of KJ, thus further revealing its higher defective nature and structural distortion arising from the S doping. Besides, an obvious red shift of the G band is found in CoS_2/SKJ (1586 cm^{-1}) compared with KJ carbon (1592 cm^{-1}), which is a typical characteristic of n-type substitutional doping. Such a phenomenon can be attributed to the elongation of C−C bonds induced by the S-doping, which weakens the bond strength and thus decreases the vibrational frequency.[148,149] The XRD results coupled with Raman spectroscopy confirms that S atoms have been successfully incorporated into the carbon framework with the formation of numerous defects within CoS_2/SKJ, and that the S doping of graphitized carbon can be achieved by our approach.

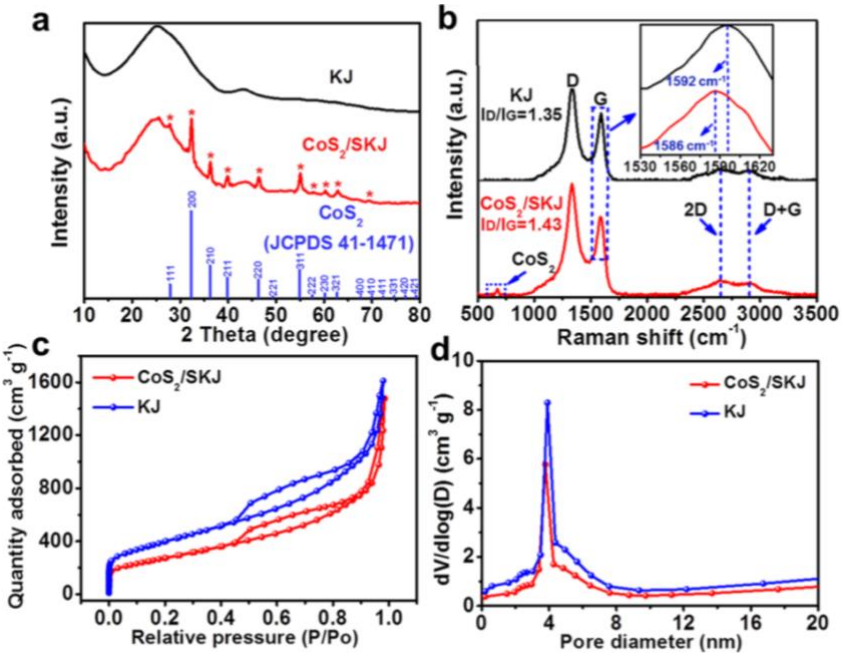

Figure 3.6 (a) XRD patterns, (b) Raman spectra with a magnified inset, (c) N_2 adsorption−desorption isotherms, and (d) pore size distribution of KJ and CoS_2/SKJ.

It is well-known that a high porosity and large surface area are crucial attributes of catalysts with good activity, and thus, the pore texture of the catalytic materials is investigated by N_2 adsorption and desorption measurement. As displayed in Figure 3.6c, a typical type-IV isotherm with a hysteresis loop in the medium pressure range reveals the mesoporous nature. The specific surface area of KJ is 1433 $m^2 g^{-1}$, and its pore volume is 2.6 $cm^3 g^{-1}$. Correspondingly, KJ exhibits narrow pore size distribution (PSD) that can effectively immobilize CoS_2 nanoparticles and prohibit detachment from the carbon pores, thus presenting a "ship in a bottle" design. After the thermal sulfurization with the formation of CoS_2 inside the pores, the specific surface area drops to 993 $m^2 g^{-1}$, while the pore volume decreases to 2.0 $cm^3 g^{-1}$. This high porosity of CoS_2/SKJ is favorable for exposing a high density of active sites and supplying large diffusion space for reactants, which are beneficial for its electrocatalytic performance. Compared to KJ, CoS_2/SKJ maintains similar shapes of the isotherm curve and PSD plots except with decreased pore volume, and there is no shift of the PSD peak position between CoS_2/SKJ and KJ. This strongly suggests that CoS_2 nanoparticles were immobilized within the pores. The small CoS_2 crystal size is derived from the adsorbed water vapor confined within the carbon pores, where its limited amount further determines the size of the cobalt-hydrolyzed product, followed by the sulfurization process, in which CoS_2 is formed without particle agglomeration and crystal growth owing to the pore confinement effect.

The loading amount of CoS_2 within the carbon pores is evaluated by TGA, as shown in Figure 3.7a. Commercially pure CoS_2 is also studied by TGA for determining the loaded CoS_2 content in CoS_2/SKJ, which is calculated to be 15.5 wt %, while the carbon content is 84.5 wt %. The calculation process of the CoS_2 loading content in CoS_2/SKJ is as below:

A hypothesis that the mass content of CoS_2 in CoS_2/SKJ is x while that of carbon in CoS_2/SKJ is y, and consequently x + y = 1, is made. According to the TGA curve of commercially pure CoS_2, it can be found that pure CoS_2 retains 64.5% of its original weight after a complex phase change process. From the TGA curve of KJ, it can be concluded that KJ carbon has almost completely burned out at 720 °C in air atmosphere. For CoS_2/SKJ with the residue weight percentage of 10.0%, consequently, an equation can be applied as follows, x × 64.5% + y × 0 = 1 × 10.0%. Based on the above two equations, x is calculated as 15.5 wt.% while y is 84.5 wt.%, indicating that CoS_2 accounts for 15.5 wt.% of the CoS_2/SKJ.

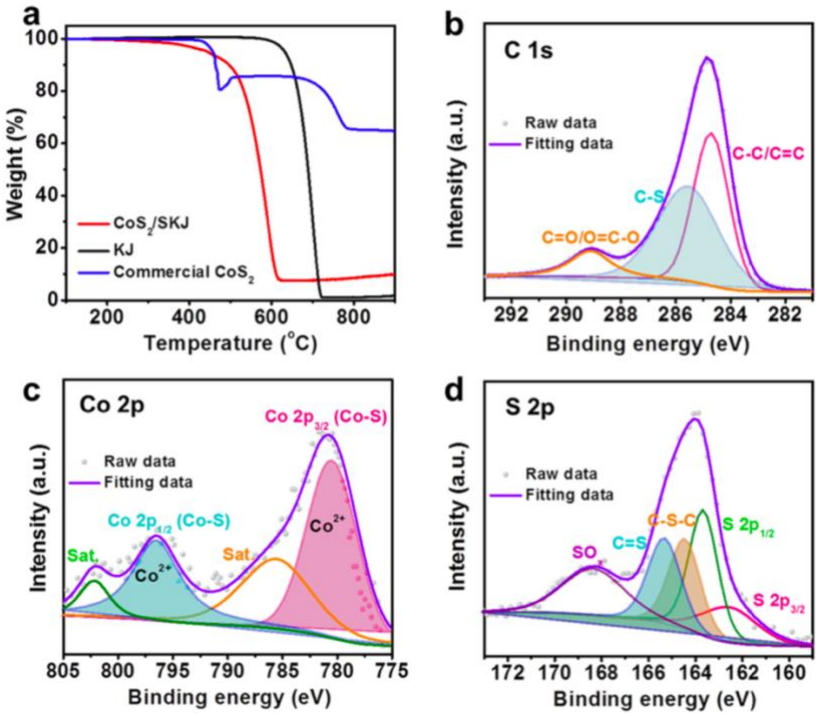

Figure 3.7 (a) TGA curves of CoS_2/SKJ, KJ, and commercial pure CoS_2 measured in air; high-resolution XPS spectra of (b) C 1s, (c) Co 2p, and (d) S 2p for CoS_2/SKJ.

To further investigate the elemental compositions and bonding configurations in CoS_2/SKJ, XPS is conducted (Figure 3.7b–d). The high-resolution C 1s spectrum (Figure 3.7b) not only

shows peaks corresponding to C−C at 284.8 eV and C=O at 289.0 eV but also exhibits an apparent C−S peak located at 285.6 eV, implying that S was successfully doped into the carbon lattice network by forming the C−S covalent bond.[150] In the high-resolution Co 2p spectrum (Figure 3.7c), a pair of characteristic peaks located at 780.5 and 796.5 eV are assigned to Co $2p_{3/2}$ and Co $2p_{1/2}$ with two satellite peaks at 785.5 and 802.2 eV, respectively, confirming the presence of Co^{2+} in the CoS_2 phase.[151,152] Figure 3.8 compares the Co 2p spectra of as-prepared CoS_2/SKJ and pure CoS_2. It is clearly seen that Co peaks in CoS_2/SKJ slightly shift to the lower energy region compared to those of pure CoS_2. This is because the electron cloud is expected to show a bias between CoS_2 and S-doping carbon framework, forming a strong electronic coupling between these two components. Figure 3.7d presents the S 2p spectrum, in which the peaks at 162.6 and 163.7 eV are attributed to S $2p_{3/2}$ and S $2p_{1/2}$, respectively, corresponding to the disulfide S_2^{2-}.[153] A pair of characteristic peaks appearing at 164.4 and 165.3 eV belong to C−S−C and C=S bonds, respectively, validating that our designed thermal sulfurization process leads to S incorporation into the carbon skeleton resulting in C−S bonded groups.[151,154] The existence of the C−S−C bond, which has been recognized as an effective active site, contributes to considerable catalytic activity.[155] The peak centered at 168.4 eV arises from a SO_x species, such as sulfonate or sulfate, which is probably formed by the surface oxidation of sulfur due to the exposure in air.[156,157] Therefore, the S-doping and carbon defective nature of CoS_2/SKJ have been unveiled by XRD, Raman, and XPS results, which plays a key role for enhancement of the electrocatalytic activity.

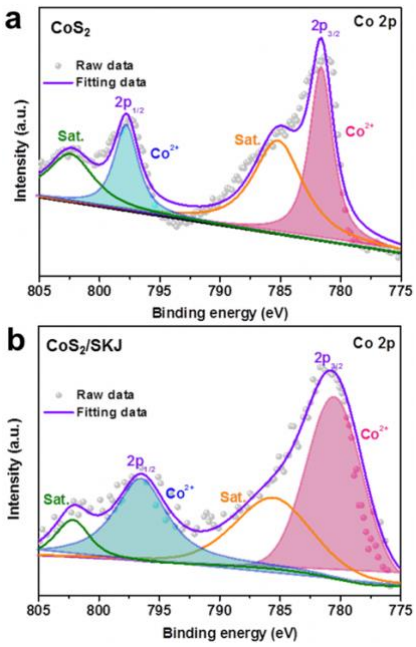

Figure 3.8 High-resolution XPS spectra of Co 2p for (a) commercial pure CoS_2 and (b) CoS_2/SKJ.

Hitherto, the above results and analysis have demonstrated that our designed small CoS_2 nanoparticles encapsulated inside pores of S-doped and highly defective carbon nanomaterials have been successfully prepared, thereby realizing a "ship in a bottle" design. All the exhibited features endow the product (CoS_2/SKJ) with great potential as an exceptional electrocatalyst for Zn−air batteries.

The bifunctional electrocatalytic performance of CoS_2/SKJ was evaluated via the linear sweep voltammetry (LSV) measurements. As a control, S-doped carbon was prepared by direct thermal sulfurization of KJ (denoted as SKJ). LSV measurements of CoS_2+SKJ, SKJ, commercial CoS_2 nanoparticles and KJ, as well as noble-metal catalyst (i.e., Pt/C and Ir/C) were conducted for comparison. The polarization curves of various prepared catalysts measured at a rotation speed of 1600 rpm are shown in Figure 3.9a. Compared to KJ, SKJ

shows a higher onset potential of 0.80 V (versus the reversible hydrogen electrode, RHE) and diffusion-limited current density of 4.8 mA cm^{-2}, which confirms the significant role of S-doping in enhancing ORR catalytic activity. CoS_2+SKJ shows a low onset potential of 0.82 V and diffusion-limited current density of 4.8 mA cm^{-2}, which is similar to the commercial CoS_2 nanoparticles (0.81 V and 4.1 mA cm^{-2}). By comparison, CoS_2/SKJ exhibits a prominent improvement on ORR performance, with a higher onset potential of 0.92 V and larger diffusion-limited current density of 5.2 mA cm^{-2}. Moreover, CoS_2/SKJ shows a half-wave potential ($E_{1/2}$) of 0.84 V, which is only about 10 mV more negative than that of commercial Pt/C catalyst but much higher than that of CoS_2+SKJ (0.76 V), SKJ (0.69 V), commercial CoS_2 nanoparticles (0.74 V), and KJ (0.66 V), highlighting the superior electrocatalytic activity of the CoS_2/SKJ catalyst. To further investigate the electron-transfer kinetics of the CoS_2/SKJ catalyst, polarization curves were measured at different rotation speeds. As shown in Figure 3.9b, CoS_2/SKJ shows a well-defined plateau of diffusion-limited currents at all rotation speeds, where, as expected, the current densities increases with the rise of rotation speeds, which is owing to the expedited mass transfer of oxygen molecules from the electrolyte to the electrode surface. More importantly, the K−L plots of CoS_2/SKJ present good linearity and near parallelism at different potentials, revealing the first-order reaction kinetics toward the concentration of dissolved oxygen.[158] The electron-transfer number (n) for CoS_2/SKJ obtained from the K−L plot slope is 4.0, signifying the fast kinetics with a four-electron-transfer reaction pathway to reduce oxygen directly to OH^-. The superior reaction kinetics are attributed to the fast electron transfer benefiting from an interconnected conductive carbon framework, which

not only surrounds the CoS_2-impregnated pores but also is present within the whole composite. These results confirm the superior ORR catalytic activity of CoS_2/SKJ.

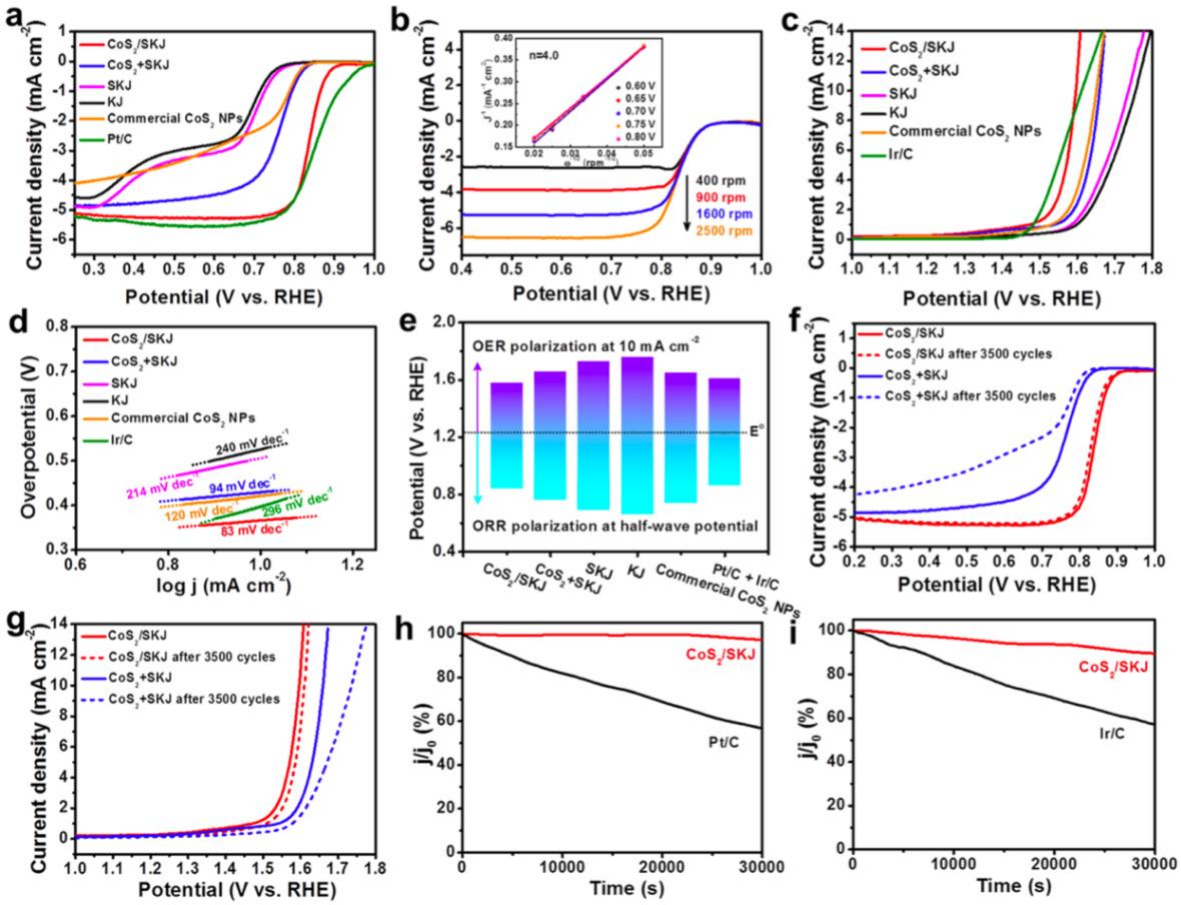

Figure 3.9 (a) ORR curves of various catalysts in O_2-saturated 0.1 M KOH solution at 1600 rpm. (b) LSV curves of CoS_2/SKJ at different rotating speeds (inset: K−L plots obtained under various potentials). (c) OER curves and (d) Tafel plots of various catalysts at 1600 rpm in N_2-saturated 0.1 M KOH electrolyte. (e) differences between the ORR $E_{1/2}$ and OER $E_{j=10}$ of different catalysts. (f) ORR and (g) OER activities of CoS_2/SKJ and CoS_2+SKJ before and after 3500 cycles, respectively. (h) ORR and (i) OER chronoamperometric response of CoS_2/SKJ and Pt/C, CoS_2/SKJ and Ir/C at a constant potential of 0.7 and 1.6 V, respectively.

Oxygen evolution activities are also investigated to confirm the suitability of CoS_2/SKJ as bifunctional electrocatalysts for both ORR and OER. Figure 3.9c illustrates the LSV behavior of the as-prepared catalysts in N_2-saturated 0.1 M KOH. As expected, CoS_2/SKJ exhibits a OER potential of only 1.58 V at the current density of 10 mA cm^{-2}, which is smaller than CoS_2+SKJ (1.66 V), SKJ (1.73 V), commercial CoS_2 (1.65 V), and KJ (1.76 V), demonstrating the smallest over-potential of CoS_2/SKJ among the obtained catalysts. In particular, the over-potential at 10 mA cm^{-2} ($\eta_{j=10}$) of CoS_2/SKJ (350 mV) is even smaller than that of commercial Ir/C catalyst (380 mV), revealing its excellent OER electrocatalytic activity. The fast OER kinetics of CoS_2/SKJ is further revealed by its smaller Tafel slope (83 mV dec^{-1}) relative to the other catalysts (Figure 3.9d). In addition, the activity improvement from KJ to SKJ reflects that S doping effectively contributes to OER catalytic activity enhancement.

To reveal the bifunctional activity of the CoS_2/SKJ catalyst, the potential difference ΔE between the ORR half-wave potential ($E_{1/2}$) and OER potential at 10 mA cm^{-2} ($E_{j=10}$) is assessed, with a smallest value of ΔE ($\Delta E = E_{j=10} - E_{1/2}$) indicating superior catalytic bifunctionality. The over-potential toward ORR and OER is reflected by comparing with the E^o (OH^-/O_2) = 1.23 V. As illustrated in Figure 3.9e and Table 3.1, CoS_2/SKJ exhibits a desirable ΔE of 0.74 V, smaller than Pt/C coupled with Ir/C, as well as the other as-prepared catalysts. More importantly, the low ΔE of CoS_2/SKJ outperforms the majority of well-developed bifunctional catalysts reported recently (Table 3.2), unveiling the superior bifunctional electrocatalytic nature of CoS_2/SKJ.

Table 3.1 Bifunctional activities for ORR and OER of as-prepared catalysts

Catalysts	ORR			OER	Bifunctionality
	Onset potential (V)	**Half-wave potential ($E_{1/2}$, V)**	**Limiting current density (mA cm^{-2})**	**Potential at 10 mA cm^{-2} ($E_{j=10}$, V)**	**$\Delta E = E_{j=10} - E_{1/2}$**
CoS_2/SKJ	0.92	0.84	5.2	1.58	0.74
CoS_2+SKJ	0.82	0.76	4.8	1.66	0.90
SKJ	0.80	0.69	4.8	1.73	1.04
KJ	0.78	0.65	4.6	1.76	1.11
Commercial CoS_2 NPs	0.81	0.74	4.1	1.65	0.91

To further reveal the significant role of pore spatial confinement in catalyst stability, the electrochemical durability of CoS_2/SKJ and CoS_2+SKJ was investigated. As shown in Figure 3.9f and Table 3.3, CoS_2/SKJ exhibits much better ORR stability than CoS_2+SKJ, with a smaller $E_{1/2}$ loss (1.2%) than CoS_2+SKJ (6.6%) after 3500 cycles. For the OER stability evaluation after 3500 cycles (Figure 3.9g and Table 3.3), CoS_2+SKJ shows a substantial increase in $\eta_{j=10}$ (500 mV), whereas CoS_2/SKJ mostly maintains its OER activity with a $\eta_{j=10}$ of 370 mV. The inferior stability of CoS_2+SKJ is precisely owing to the absence of the pore confinement effect, which results in a severe agglomeration after a long-term cycling (Figure 3.10), causing inevitable loss of catalytic activity. Furthermore, CoS_2/SKJ and noble-metal benchmark catalysts were also evaluated via a chronoamperometric (CA) measurement at 0.7 V (Figure 3.9h). CoS_2/SKJ retains 97.5% of the initial ORR current, far superior to the 57.0% retention of Pt/C. Likewise, the excellent OER stability of CoS_2/SKJ is also revealed by the

CA test at 1.6 V, with only 9.8% current decay after 30000 s, whereas Ir/C presents a much larger current decay of 42.0% (Figure 3.9i)

Table 3.2 Summary of the ORR and OER activities of recently reported bifunctional electrocatalysts

Catalyst	ORR: $E_{1/2}$ (V)	OER: $E_{j=10}$ (V)	$\Delta E = E_{j=10} - E_{1/2}$ (V)	Reference
CoS_2/SKJ	**0.84**	**1.58**	**0.74**	**This work**
3DOM-Co@TiO_XN_y	0.84	1.62	0.78	*Adv. Mater.* 2019, 31, 1806761
CoS_x@PCN/rGO	0.78	1.57	0.79	*Adv. Energy Mater.* 2018, 8, 1701642
NPMC-1000	0.85	1.75	0.90	*Nat. Nanotechnol.* 2015, 10, 444
Co-C_3N_4/CNT	0.82	1.61	0.79	*J. Am. Chem. Soc.* 2017, 139, 3336
Co_3O_4/NPGC	0.84	1.68	0.84	*Angew. Chem., Int. Ed.* 2016, 55, 4977
Co_3O_4/N-rmGO	0.83	1.59	0.76	*Nat. Mater.* 2011, 10, 780
Co@Co_3O_4/NC	0.80	1.65	0.85	*Angew. Chem., Int. Ed.* 2016, 55, 4087
NiCo/PFC	0.79	1.63	0.84	*Nano Lett.* 2016, 16, 6516
$CuCo_2O_4$/N-CNTs	0.80	1.69	0.89	*Adv. Funct. Mater.* 2017, 27, 1701833
Co_xO_y/NC	0.80	1.66	0.86	*Angew. Chem., Int. Ed.* 2014, 53, 8508
S/N_Fe-27	0.87	1.78	0.91	*J. Am. Chem. Soc.* 2014, 136, 14486
Co_3O_4/HPNC	0.84	1.65	0.81	*ACS Appl. Mater. Interfaces* 2017, 9, 30662
Co/N-C-800	0.74	1.60	0.86	*Nanoscale* 2014, 6, 15080

Table 3.3 Summary of ORR and OER activities of CoS_2/SKJ and CoS_2+SKJ before and after 3500 cycles of cyclic voltammetry between 0.7 and 1.6 V

Catalyst	ORR: $E_{1/2}$ (V)			OER: $\eta_{j=10}$ (mV)		
	Initial	After 3500 cycles	$\Delta E_{1/2}$ (%)	Initial	After 3500 cycles	$\Delta \eta_{j=10}$ (%)
CoS_2/SKJ	0.84	0.83	1.2	350	370	5.7
CoS_2+SKJ	0.76	0.71	6.6	430	500	16.3

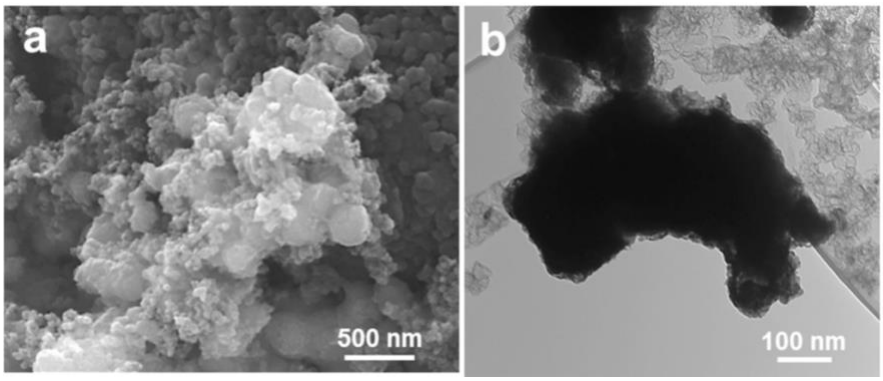

Figure 3.10 (a) SEM and (b) TEM images of CoS_2+SKJ after 3500 cycles of cyclic voltammetry between 0.7 and 1.6 V.

Building upon the promising ORR/OER electrocatalytic activity and durability presented above, CoS_2/SKJ was used as a bifunctional catalyst within the air cathode to assemble rechargeable Zn−air batteries. Figure 3.11a exhibits a schematic of the Zn−air battery system. Commercial Pt/C plus Ir/C were also assembled in the Zn−air battery under same technique condition as the reference. The galvanodynamic charge and discharge curves are illustrated in Figure 3.11b. Both Zn−air batteries deliver a similar open-circuit voltage of ca. 1.4 V, but CoS_2/SKJ exhibits more-desirable charging and discharging curves. A narrower voltage gap between charge and discharge polarization voltages is found for CoS_2/SKJ, which reveals its

better charge and discharge performance than the commercial Pt/C plus Ir/C mixture catalyst. Besides, CoS_2/SKJ delivers a higher power density (over 104 mW cm^{-2}) than Pt/C−Ir/C hybrid catalyst (84 mW cm^{-2}) (Figure 3.11b). This is because increased exposure of accessible active CoS_2 nanoparticles assures a higher power generation per unit area of electrode. At a certain current density, the battery energy efficiency is based on the ratio of the discharge potential to the charge potential.[160] As shown in Figure 3.11c, at the current density of 120 mA cm^{-2}, the energy efficiency of CoS_2/SKJ is 1.5 times higher than that of the noble-metal benchmark, which is attributed to its provision of unimpeded access for reactants reaching toward the active sites (i.e., the high-efficiency catalyst utilization). Moreover, the more salient electrochemical performance of the CoS_2/SKJ air electrode is also due to the interconnected conductive carbon network and interpenetrating porous structure, which guarantee fast charge transfer, as well as enhanced accessibility of oxygen species and electrolyte to the electrocatalytic sites.

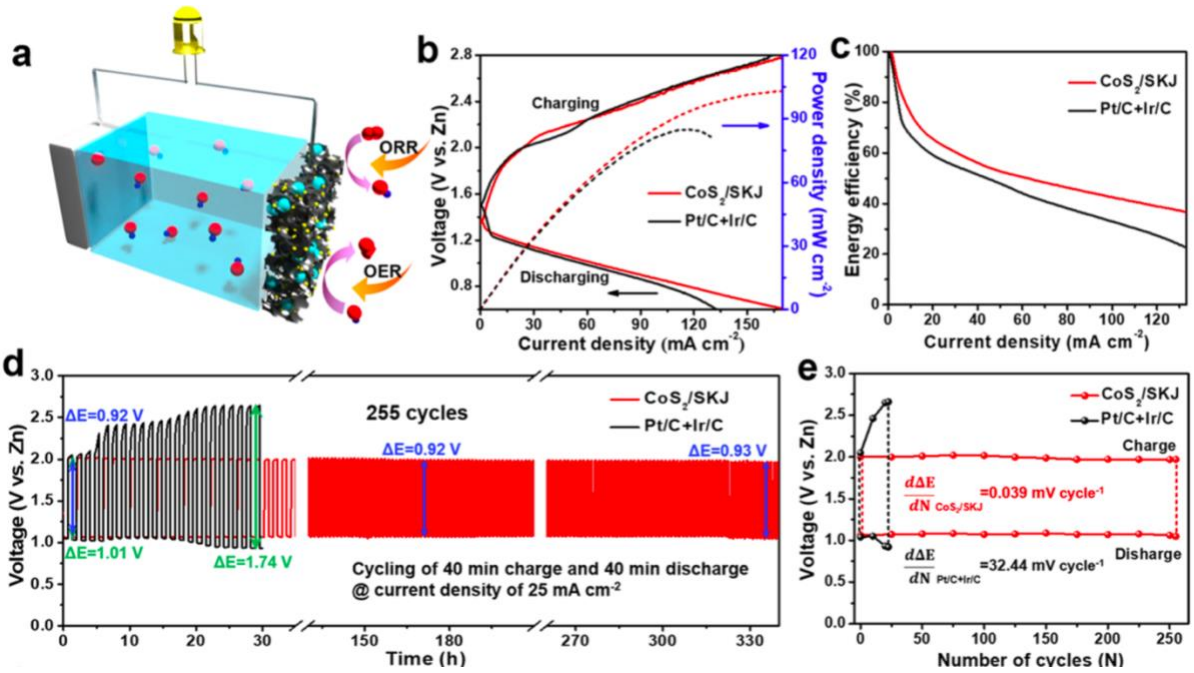

Figure 3.11 (a) Schematic illustration of the Zn−air battery configuration, (b) galvanodynamic charge and discharge polarization curves and corresponding power density plots, (c) energy-efficiency plots, (d) cycling performance, and (e) voltage variation with cycles for Zn−air batteries assembled using CoS_2/SKJ and noble-metal Pt/C plus Ir/C catalysts in ambient air.

To further investigate the efficiency and cycle stability of CoS_2/SKJ for the Zn−air battery, a galvanostatic charge−discharge test is performed at a high current density of 25 mA cm^{-2}, which cycles with 40 min charging and 40 min discharging. As illustrated in Figure 3.11d, the initial charge−discharge voltage gap of CoS_2/SKJ is 0.92 V, smaller than that of the noble-metal benchmark Pt/C plus Ir/C catalyst (1.01 V). More importantly, the Zn−air battery assembled with CoS_2/SKJ exhibits a superior durability without noticeable voltage fading for both charge and discharge processes over 340 h of continuous operation, whereas the battery using Pt/C plus Ir/C catalyst delivers a limited cyclability with operation time of less than 30 h. The poor stability of Pt/C plus Ir/C catalyst is because of the dissolution and redeposition, migration and aggregation, and sintering of the noble-metal particles as well as the formation of the insulating platinum oxides under operational conditions.[161] These could lead to an increase in the particles' size and the particle detachment, causing the irreversible loss of active sites and degradation of electrocatalytic performance.[162] The battery energy efficiency of Pt/C−Ir/C hybrid catalyst reduces far faster than that of CoS_2/SKJ, leading to significant charge and discharge performance losses. Particularly, the battery with CoS_2/SKJ can also withstand a very high current density (25 mA cm^{-2}), presenting an extremely low decaying rate of 0.039 mV per cycle and a small voltage gap of 0.93 V after 255 cycles, much better than the noble-metal benchmark with a high voltage decaying rate (32.44 mV per cycle) and voltage gap (1.74

V) (Figure 3.11e). Such long-lasting cyclability over this time scale in this work is evidently superior to other recently reported results, as summarized in Table 3.4.

Table 3.4 Summary of the cyclability of rechargeable Zn−air batteries assembled with state-of-the-art bifunctional oxygen electrocatalysts

Catalyst	Cyclability	Reference
CoS_2/SKJ	**lifetime of over 340 h @ 25 mA cm^{-2}**	**This work**
c-$Co_xMn_{3-x}O_4$	lifetime of over 17 h @ 10 mA cm^{-2}	*Nat. Commun.* 2015, *6*, 7345
$Pb_2Ru_2O_{6.5}$	lifetime of over 35 h @ 10 mA cm^{-2}	*Energy Environ. Sci.* 2017, *10*, 129
(Mg, Co)$_3O_4$@NGC	lifetime of over 200 h @ 10 mA cm^{-2}	*ACS Energy Lett.* 2017, *2*, 2706
3DOM-Co@TiO_xN_y	lifetime of over 300 h @ 20 mA cm^{-2}	*Adv. Mater.* 2018, *31*, 1806761
N-GRW	lifetime of over 150 h @ 2 mA cm^{-2}	*Sci. Adv.* 2016, *2*, e1501122
Co-N-CNTs	lifetime of over 15 h @ 2 mA cm^{-2}	*Adv. Funct. Mater.* 2018, *28*, 1705048
Co_3O_4/NPGC	lifetime of over 80 h @ 5 mA cm^{-2}	*Angew. Chem., Int. Ed.* 2016, *55*, 4977
C-MOF-C2-900	lifetime of over 120 h @ 2 mA cm^{-2}	*Adv. Mater.* 2018, *30*, 1705431
NCNT-CoO-NiO-NiCo	lifetime of 17 h @ 20 mA cm^{-2}	*Angew. Chem., Int. Ed.* 2015, *54*, 9654
Co_3O_4NC/N-CNT	lifetime of 100 h @ 20 mA cm^{-2}	*ChemSusChem* 2015, *8*, 3129
Co@Co_3O_4	lifetime of 40 h @ 20 mA cm^{-2}	*Small* 2016, *12*, 2580

Undoubtedly, the impressive stability and long-term rechargeability of CoS_2/SKJ can be attributed to the pore confinement design. Specifically, the carbon pores provide spatial confinement to restrict the overgrowth of active CoS_2 nanoparticles and prevent them from aggregating during the catalysis and cycle process. At the same time, S doping within the

carbon framework can modify the electronic and steric pore environment with the formation of the C−S bond, which may afford strong affinity toward CoS_2, which can, in turn, immobilize CoS_2 nanoparticles inside the pores. To affirm the structural evolution upon cycling as the evidence for the above analysis, SEM, TEM, and HAADF-STEM observations were carried out on the CoS_2/SKJ electrode after cycling over 340 h. Figure 3.12a demonstrates that the intact 3D architecture was retained during the battery cycling. CoS_2 nanoparticles are found still immobilized well inside the carbon pores with an original size of around 8.0 nm without obvious agglomeration or detachment (Figure 3.12b and c). This manifests the robust carbon framework structure and effective pore spatial confinement effect, which contributes to the excellent durability. Finally, the application prospect of the device is demonstrated in Figure 3.12d. A total of three CoS_2/SKJ-batteries power a mini-fan equipped with light-emitting diode (LED), which operates at a minimum voltage of 3.6 V.

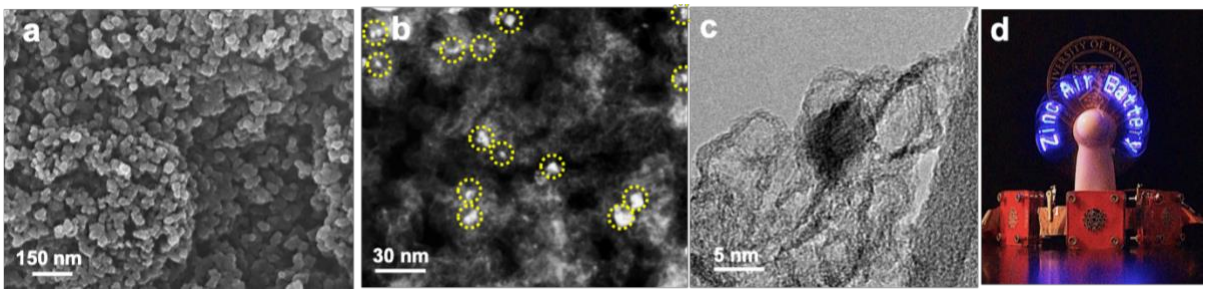

Figure 3.12 (a) SEM, (b) HAADF-STEM, and (c) TEM images of CoS_2/SKJ catalyst after galvanostatic charge−discharge cycling over 340 h (255 cycles) with (d) a demonstration of assembled Zn−air batteries operated in ambient air to power a mini-fan equipped with LEDs.

All of the above results highlight the excellent bifunctional electrocatalytic activity and long-term durability of CoS_2/SKJ, which profit from the following aspects. (i) The pore spatial confinement effect makes fine active CoS_2 nanoparticles root inside graphitized carbon pores,

which not only presents a high surface-to-volume ratio to facilitate the exposure of more catalytically active sites but also effectively inhibits overgrowth and agglomeration of nanocatalysts during a long-cycling catalytic process. (ii) The formation of the C−S−C bond derived from S doping into the carbon skeleton acts as an important catalytically active site for promoting ORR and OER. As per previous reports,[163] it can break the electro-neutrality of carbon to create positively charged sites favorable for O_2 adsorption, and this parallel diatomic adsorption can effectively weaken the O−O bonding to further promote the direct reduction of oxygen to OH^- via a four-electron process. Additionally, the S doping within the carbon framework can also enhance the spin density, which plays a pivotal role in determining the catalytically active sites.[164] (iii) The defect-rich interfaces function as atomic traps, which can effectively boost the localization of oxygen species toward active sites, promoting the catalytic activity and stability. (iv) The graphitized carbon framework not only intimately enfolds the CoS_2 nanoparticles but also interpenetrates over the whole composite, building up an interconnected conductive network to offer fast electron transfer. More importantly, the interpenetrating porous structures erect a robust 3D architecture as the nanoreactors for ion and oxygen species transfer inside and through the CoS_2/SKJ catalyst, which significantly improves the kinetics for electrocatalytic processes. This architecture capitalizes on the synergistic interactions between CoS_2 nanoparticles, carbon defects, and intimate covalent bonds (i.e., C−S bonding) from S doping under the steric pore environment, which endow CoS_2/SKJ with prominent catalytic performance.

3.4 Conclusions

In this work, an exquisite bifunctional catalyst consisting of fine CoS_2 nanoparticles encapsulated inside the defective carbon pores is designed and successfully accomplished via precursor impregnation, hydrolysis and subsequent thermal sulfurization. This methodology realizes the combination of excellent catalytic kinetics and electrical conductivity provided by the interconnecting porous carbon framework acting as a nanoreactor, which effectively restricts the nucleation (i.e., overgrowth) and agglomeration of nanoparticles during catalysis. Therefore, this elaborately designed catalyst, harvesting the synergistic effect between defect-rich interfaces (i.e., S-doped pores) and effective catalytic active sites (CoS_2 and C−S−C bonding) guarantees superior electrochemical performance. The as-developed CoS_2/SKJ catalyst exhibits excellent catalytic activity and durability for both ORR and OER with a ΔE of 0.74 V, unveiling its excellent bifunctional catalytic ability for rechargeable Zn−air batteries. Encouragingly, when integrated within an air electrode, CoS_2/SKJ exhibits low charge and discharge over-potential (i.e., high energy efficiency), large peak power density, and exceptionally stable cyclability of over 340 h at a very high current density of 25 mA cm^{-2}, outperforming noble-metal benchmarks and other recently reported results. This work provides a guide to designing efficient and durable non-precious-metal bifunctional electrocatalysts for metal−air batteries, and we believe that such a universal “ship in a bottle” design of impregnating fine metal nanoparticles inside pores will deliver an instructive model of material engineering for implementation in various fields.

Chapter 4 Synergistic Engineering of Defect and Crystallinity Manipulation on Tantalum-Based Electrocatalyst for Polysulfide Catalysis and Retention for High-Performance Li-S Batteries

Based on the proposed "ship in a bottle" design strategy in Chapter 3, Chapter 4 will further take advantage of this strategy to manipulate the crystallinity of metal nanoclusters and introduce defect engineering, promisingly enabling an efficient electrocatalyst for polysulfide conversion and retention in Li-S batteries.

4.1 Introduction

The burgeoning energy demand of modern society has been spurring extensive research interests in pursuit of next-generation high-energy-density energy-storage systems.[165,166] Li-S batteries present one of the most promising solutions to high-efficiency and cost-effective energy storage.[167,168] Yet, despite their intriguing merits including high energy density and low cost, progress toward the widespread commercialization of Li-S batteries is impeded by several technical challenges. The intrinsic poor electrical conductivity of sulfur and discharge products (Li_2S/Li_2S_2), the shuttling behavior derived from the dissolution of lithium polysulfide (LPS), and more importantly, the sluggish kinetics for LPS conversion reactions, result in poor sulfur utilization, rapid capacity decay, and unsatisfactory cycle life.[169,170] Strategies to address these issues rely mostly on the following. (i) A well-designed electrode structure is expected to effectively retain LPS to suppress the shuttling effect and mitigate the S volume expansion during lithiation for enhanced cycle stability.[171,172] (ii) Besides, the establishment of a pass-through system enables fast electron and ion conduction for sufficient LPS redox

reactions.[173,174] (iii) More importantly, an efficient electrocatalyst, such as transition metal oxides and sulfides,[175,176] accelerates the reaction kinetics of soluble LPS conversion into insoluble Li_2S/Li_2S_2 to reduce their dissolution and diffusion in the electrolyte. This could promote both sulfur utilization and battery cycle life. Additionally, the catalytic activity for a reaction is correlated with the exposed active sites that have unique chemical and electronic structures.[177,178] Defect engineering and crystallinity tuning, which possess good capability of altering the electronic environment for enhanced LPS adsorptive and catalytic features,[179,180] provide a promising approach to improving Li-S electrochemistry.

In the search for an efficient electrocatalyst for LPS conversion in the Li-S system, tantalum oxide (Ta_2O_5) is found to be an attractive candidate. Ta_2O_5 possesses high thermodynamic stability due to the strong Ta–O bonding, and a high dielectric constant.[181] The synergism between the Ta d-orbital and the unsaturated O atom results in an effective d-band structure,[182] potentially imparting catalytic characteristics with suitable valence band maximum (VBM) and conduction band minimum (CBM) straddling the polysulfide redox potentials. Besides, the introduction of surface defects is capable of further tailoring band structure toward desirable electron mobility and catalytic activity.[183] Here, this study provides the first rational application of amorphous oxygen-defective Ta_2O_{5-x} as an electrocatalyst in Li-S batteries. Ultrafine amorphous Ta_2O_{5-x} nanoclusters are implanted within the micropores of carbon nanospheres (a-Ta_2O_{5-x}/MCN). The elaborate design presents multiple merits to fulfill the aforementioned rules. (i) The Ta_2O_{5-x}-in-pore strategy presents a ‘‘ship in a bottle’’ structure, shaping a 3D conductive nanoreactor, which not only guarantees a high surface-to-volume ratio to offer abundant polysulfide-retaining and catalytically active sites but also prevents the agglomeration of nanoclusters during synthesis and catalysis, potentially addressing the long-

term issue of nanocatalyst stability. (ii) The interconnected porous conductive network promotes the penetration of electrolytes and charge transfer, leading to fast motion of ions and electrons throughout the framework. (iii) The tailored pitaya-like architecture promotes sulfur homogenization and buffers their volume expansion during cycling. (iv) The nucleation process of Ta_2O_{5-x} nanoseeds is constrained by the nanopores to realize crystallinity tuning, which alters the Ta–O bond length and provides increased binding energy (BE) between Ta_2O_{5-x} and LPS. (v) Oxygen deficiencies in the Ta_2O_5 nanoclusters manipulate the local coordination environment and electron band structure, which significantly ameliorate the intrinsic conductivity and function as catalytic centers to accelerate LPS conversion. Ex situ X-ray absorption spectroscopy (XAS) and theoretical calculations demonstrate the enhanced LPS-retaining and electrocatalytic features driven by pore-guided amorphous structure and oxygen defects. The a-Ta_2O_{5-x}/MCN-based sulfur electrode presents excellent Li-S performance, i.e., superb rate capability up to 5 C, long-term cyclability over 1,000 cycles with an ultralow capacity fading rate of 0.029% per cycle, and high areal capacity of 5 mAh cm^{-2} under raised sulfur loading of 5.6 mg cm^{-2} and lean electrolyte/sulfur ratio of 3.6 mL g^{-1}.

4.2 Experimental Section

4.2.1 Materials Synthesis

Preparation of Microporous Carbon Nanosphere (MCN). In a typical synthesis, a 70-mL aqueous solution of 0.7 M glucose was sealed in a Teflon-lined stainless-steel autoclave and hydrothermally treated at 185 °C for 6 h. The collected precipitate was washed several times with deionized water. After drying at 80 °C for 12 h, small amount of $ZnCl_2$ aqueous solution was added to the carbonaceous powder at a 5:1 weight ratio of $ZnCl_2$ to powder under stirring

for 6 h. The suspension was dried in an oven at 110 °C to vaporize the visible water, after which the collected solid was vacuum dried for 20 h. Following this, the powder underwent pyrolysis at 850 °C for 2 h in the CO_2 atmosphere. The obtained samples were immersed in dilute hydrochloric acid under stirring and then washed with deionized water, resulting in the formation of MCN.

Preparation of a-Ta_2O_{5-x}/MCN and a-Ta_2O_5/MCN. Typically, tantalum(V) chloride was added into the anhydrous ethanol under ultrasonication for 2 h. A small amount of the prepared solution was then added to MCN in a well-dried glass vial, which was quickly capped and underwent ultrasonication for 3 h. After drying at 85 °C in vacuum for 12 h, the powder was transferred to the tube furnace and pyrolyzed in the hydrogen atmosphere (reducing environment) at the flow rate of 80 sccm at 650 °C for 2 h to yield a-Ta_2O_{5-x}/MCN. The control sample, a-Ta_2O_5/MCN, was synthesized using the above method except for annealing in the inert Ar atmosphere.

Preparation of a-Ta_2O_5 and a-Ta_2O_{5-x}. The prepared tantalum(V) chloride ethanol solution was directly dried at 80 °C under vacuum overnight. The collected solid was then heated in Ar atmosphere at 450 °C for 1 h to obtain the amorphous Ta_2O_5 (a-Ta_2O_5).[184] The control sample, a-Ta_2O_{5-x}, was prepared by the same method as a-Ta_2O_5 except for annealing in the H_2 atmosphere.

Preparation of a-Ta_2O_5+MCN. The prepared tantalum(V) chloride ethanol solution was directly dried at 80 °C in vacuum for 12 h. Next, the obtained powder was mechanically mixed with MCN with the same Ta_2O_5 content as a-Ta_2O_{5-x}/MCN and a-Ta_2O_5/MCN. The as-prepared sample was heated in Ar atmosphere at 450 °C for 1 h to yield a-Ta_2O_5+MCN.

4.2.2 Materials Characterization

N_2 adsorption-desorption isotherm analysis (ASAP 2020 micromeritics) was performed to study the pore structures. The surface area was calculated using the BET theory; pore size distribution was determined via the quenched solid state density functional theory (QSDFT) method. SEM images were collected by FEI Quanta FEG 250 ESEM while TEM images and HAADF-STEM images were collected by Phillip CM-12, JEOL JEM-2010F and FEI Titan 80-300 LB. TGA was conducted on a TA instrument Q500. UV-vis spectra were collected by Thermal Scientific GENESYS 10S spectrophotometer. The Thermal Scientific K Alpha spectrometer was employed to conduct XPS. XRD patterns were collected by MiniFlex 600 Rigaku diffractometer. The Raman spectra were obtained by a 532 nm laser source. Electron paramagnetic resonance (EPR) spectra was conducted on a Bruker EMX spectrometer at 77 K with a microwave frequency of 9.4 GHz and microwave power of 2 mW. Ta L_3-edge XAS were collected on the IDEAS beamline in Canadian Light Sources. All the XAS data were processed using the Athena program.

4.2.3 Electrochemical Measurements

a-Ta_2O_{5-x}/MCN was impregnated with sulfur of 67 wt.% via a thermal treatment at 155 °C for 6 h. The same procedures were used to prepare a-Ta_2O_5/MCN, a-Ta_2O_5+MCN, a-Ta_2O_5 and T-Ta_2O_5 sulfur composites. The composite powder, Super P and poly(vinylidene fluoride) (PVDF) were mixed in a weight ratio of 8:1:1 and dispersed in *N*-Methyl-2-pyrrolidone (NMP). The obtained slurry was coated on aluminum foil substrates (MTI Corporation), and then dried at 80 °C for 12 h. The electrochemical performance test was carried out in CR2032 type coin cell and the cells were assembled with the prepared sulfur composite cathodes, lithium plate anodes, electrolyte and polypropylene separators (Celgard 2400) in an Ar-filled

glovebox. The used electrolyte was 1 M lithium bis(trifluoromethanesulfony) imide (LiTFSI) (LiTFSI) dissolved in a mixed solvent of 1,3-dioxolane (DOL) and dimethoxymethane (DME) (1:1, v/v) with 2 wt.% $LiNO_3$ as additive. The average areal sulfur loading was ~1 mg cm^{-2} and ~5.6 mg cm^{-2} for high loading test with a decreased electrolyte/sulfur ratio of 3.6 mL g^{-1}. For symmetric cell, 30 μL electrolyte containing 0.5 mol L^{-1} of Li_2S_6 and 1.0 mol L^{-1} of LiTFSI in a 1:1 (v/v) mixture of 1,3-dioxolane (DOL) and dimethoxyethane (DME) was used as electrolyte. The cyclic voltammetry (CV) measurements of the symmetric cells were performed at the scan rate of 5 mV s^{-1}. The frequency range of the electrochemical impedance spectroscopy (EIS) tests was from 100 kHz to 1 Hz.

The LSV tests were performed to evaluate the catalytic activity of various samples in a three-electrode configuration. The cells consisted of various samples as the working electrode, saturated Ag/AgCl as the reference electrode, platinum sheet as the counter electrode, and 0.1 M Li_2S/methanol solution as the electrolyte. For the working electrode preparation, the slurry containing sample materials and PVDF at a weight ratio of 5:1 was coated on bare glassy carbon surface. The LSV measurements were conducted using electrochemical workstation (Biologic VSP 300) at a scanning rate of 5 mV s^{-1} from -0.8 V to -0.15 V.

4.2.4 DFT Calculations

The Perdew-Burke-Ernzerhof function was used for the exchange and correlation energy terms. Li_2S_6 was selected as lithium polysulfide model and studied the absorption of Li_2S_6 on T-Ta_2O_5 (001), a-Ta_2O_5 and T-Ta_2O_{5-x} (001) surfaces. A vacuum slab of about 23 Å was performed. The cell parameter of (1×2) supercell is 11.520 Å × 11.610 Å × 25.565 Å. For T-Ta_2O_5 (001) and T-Ta_2O_{5-x} (001), the bottom two atomic layers were fixed at the bulk position

whereas the remaining layers and the adsorbates were allowed to relax while for a-Ta_2O_5, all layers and the adsorbates were allowed to relax. The BE was calculated as BE = E_{total} - E_{ads} - E_{surf}, where E_{total} is the total energy of the absorbed system, E_{ads} is the energy of the optimized Li_2S_6 in vacuum and E_{surf} is the energy of the optimized bare surface. More negative BE of the metal oxide-Li_2S_6 complex indicates its stronger interactions.

4.3 Results and Discussion

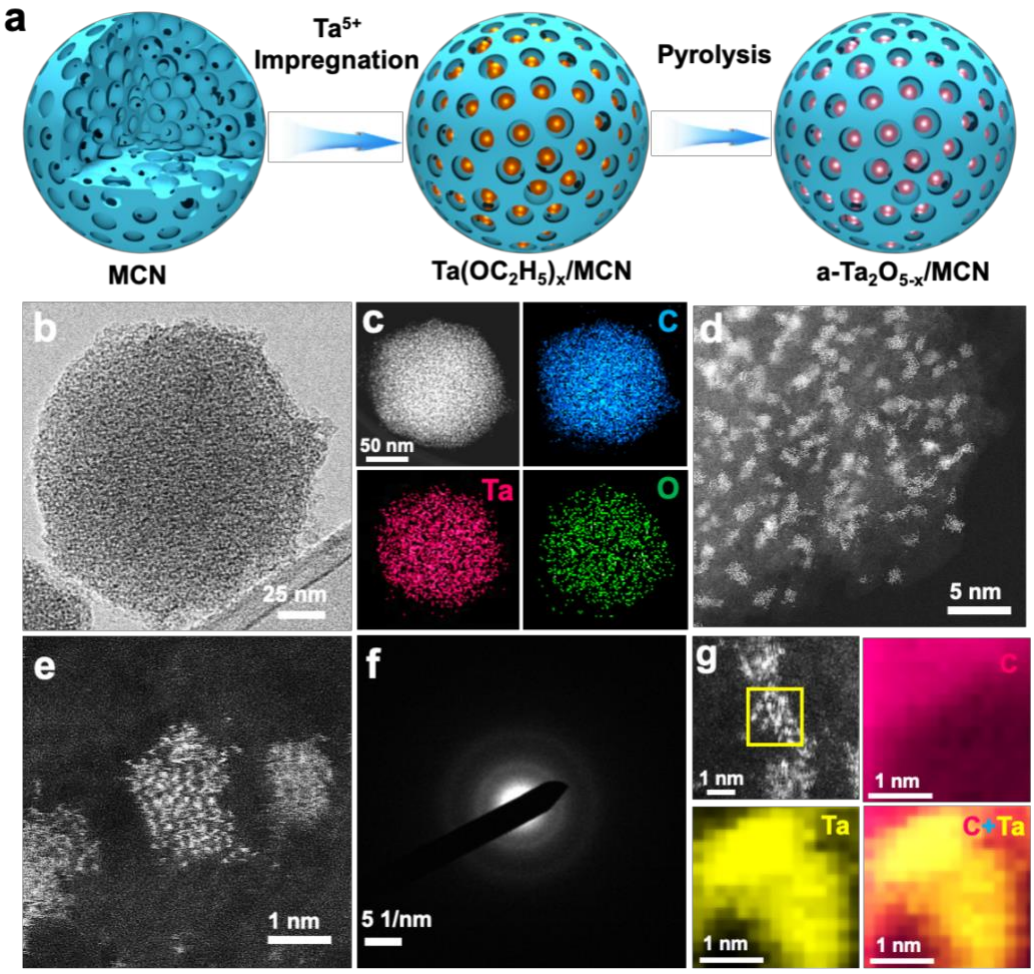

Figure 4.1 (a) Schematic illustration of the formation of a-Ta_2O_{5-x}/MCN/S; (b) TEM image, (c) EDS elemental mapping images, (d-e) HAADF-STEM images, (f) SAED pattern of a-

Ta_2O_{5-x}/MCN; (g) HAADF-STEM image and corresponding EELS elemental mapping of individual Ta_2O_{5-x} nanocluster accommodated inside carbon pores.

The synthesis strategy of a-Ta_2O_{5-x}/MCN is illustrated in Figure 4.1a. The initial microporous carbon nanosphere (MCN) was prepared by a unique dual-activation technique involving chemical and physical activation simultaneously. MCN presents regular sphericity with a uniform diameter of 150 nm (Figure 4.2a). By means of a wet-impregnation strategy, MCNs were immersed in tantalum(V) chloride ethanol solution to lead the built-in implantation of tantalum-alcoholysis product inside pores of MCN (denoted as $Ta(OC_2H_5)_x$/MCN).[185] Following this, the Ta^{5+}-impregnated MCN was pyrolyzed in the H_2 atmosphere, in which amorphous tantalum oxide with rich oxygen vacancies is shaped and immobilized within the pores (a-Ta_2O_{5-x}/MCN). Figure 4.2b displays the typical SEM image of a-Ta_2O_{5-x}/MCN, which holds a spherical morphology with uniform size and clean surface. No undesirable particle aggregation is observed on the external surface of carbon nanospheres. As displayed in TEM image (Figure 4.1b), a-Ta_2O_{5-x}/MCN exhibits the same diameter (ca. 150 nm) as MCN without apparent structure change after impregnation of Ta_2O_{5-x}. The EDS mapping (Figure 4.1c) manifests the homogeneous distribution of a-Ta_2O_{5-x} throughout the MCN matrix. As demonstrated by the HAADF-STEM image (Figure 4.1d), the bright Ta_2O_{5-x} nanocluster seeds are uniformly rooted inside the pores of MCN, presenting a pitaya-like structure. The implanted amorphous Ta_2O_{5-x} nanoclusters possess a size of around 1.2 nm (Figure 4.1e) that is consistent with the nanocluster size distribution (Figure 4.2c). It is worth noting that such tiny nanoclusters could be retained during the high-temperature treatment benefiting from strong spatial confinement effect of carbon pores, which effectively inhibits Ta_2O_{5-x} nanoclusters from agglomeration. Selected area electron diffraction (SAED) pattern

(Figure 4.1f) shows the diffused ring without observable diffraction spots, confirming the amorphous structure of Ta_2O_{5-x} that arises from its confined nucleation by carbon micropores. The HAADF-STEM image in Figure 4.1g focuses on one individual Ta_2O_{5-x} nanocluster. The corresponding EELS mapping demonstrates the intimate contact between built-in Ta_2O_{5-x} nanoclusters and carbon framework, which provides an interconnected conductive network for expediting electron transfer. These results consistently confirm the successful implantation of ultrafine, uniform, and amorphous Ta_2O_{5-x} within MCN matrix. The mass loading of Ta_2O_{5-x} in the composite is determined to be 23.5 wt.% by TGA (Figure 4.2d).

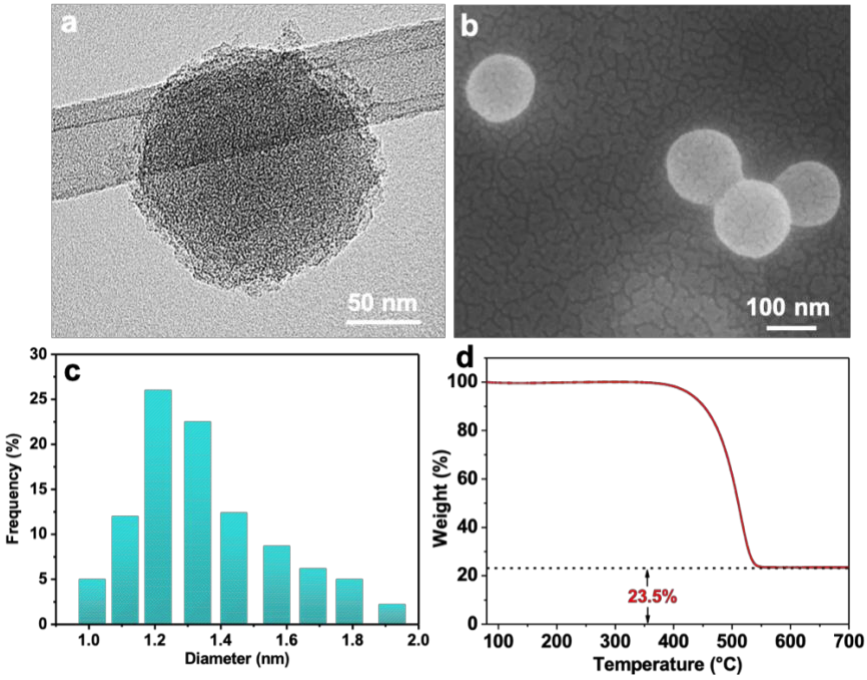

Figure 4.2 (a) TEM image of MCN. (b) SEM image, (c) Ta_2O_{5-x} nanoclusters size distribution, and (d) TGA curve of a-Ta_2O_{5-x}/MCN.

To demonstrate the important role of oxygen vacancies in Ta_2O_5 for Li-S chemistry, the control sample, a-Ta_2O_5/MCN, was prepared by annealing $Ta(OC_2H_5)_x$/MCN in Ar atmosphere at the same temperature with a-Ta_2O_{5-x}/MCN. The mass loading of Ta_2O_5 in a-Ta_2O_5/MCN is

23.3wt.% (Figure 4.3a), which is almost consistent with a-Ta_2O_{5-x}/MCN. To further show the structural merits of a-Ta_2O_{5-x}/MCN as sulfur host, three other control samples were also prepared. First, amorphous Ta_2O_5 (a-Ta_2O_5) was obtained by annealing $Ta(OC_2H_5)_x$ in Ar atmosphere at a low temperature (450°C), as confirmed by XRD (Figure 4.4a). a-Ta_2O_5 exhibits a large bulk morphology (Figure 4.3c). The second control sample was obtained by mechanically mixing $Ta(OC_2H_5)_x$ with MCN followed by the same pyrolysis process as a-Ta_2O_5 (denoted as a-Ta_2O_5+MCN). a-Ta_2O_5+MCN has a Ta_2O_5 loading of 23.2wt.% (Figure 4.3b). Devoid of the pore spatial confinement effect, a-Ta_2O_5+MCN exhibit much larger Ta_2O_5 particles with a micro-scale size (Figure 4.3d) compared to a-Ta_2O_{5-x}/MCN. Serious aggregation appears in a-Ta_2O_5+MCN, resulting in an uneven distribution of Ta_2O_5 and carbon nanospheres. Besides, the commercial Ta_2O_5 particles with a high crystallinity as shown in Figure 4.4a, are applied as another control group (T-Ta_2O_5). The amorphous nature of a-Ta_2O_{5-x}/MCN is clearly unveiled by XRD in Figure 4.4a. The two peaks of a-Ta_2O_{5-x}/MCN appearing at 23 and 43° can be indexed to the characteristic (002) and (100) plane of graphitic carbons, respectively.[186] The orthorhombic lattice structure of Ta_2O_5 possesses a long rod-shaped unit cell of 22 Ta atoms and 55 O atoms (lattice parameters: a = 6.198 Å, b = 40.290 Å, c = 3.888 Å).[187] Although the pyrolysis temperature of a-Ta_2O_{5-x}/MCN (i.e., 650 °C) is enough for the formation of Ta_2O_5 crystal,[187] the carbon micropores with the narrow space confine the nucleation of Ta_2O_{5-x} nanoclusters, which shape an incomplete unit cell in the amorphous structure even at a high temperature.

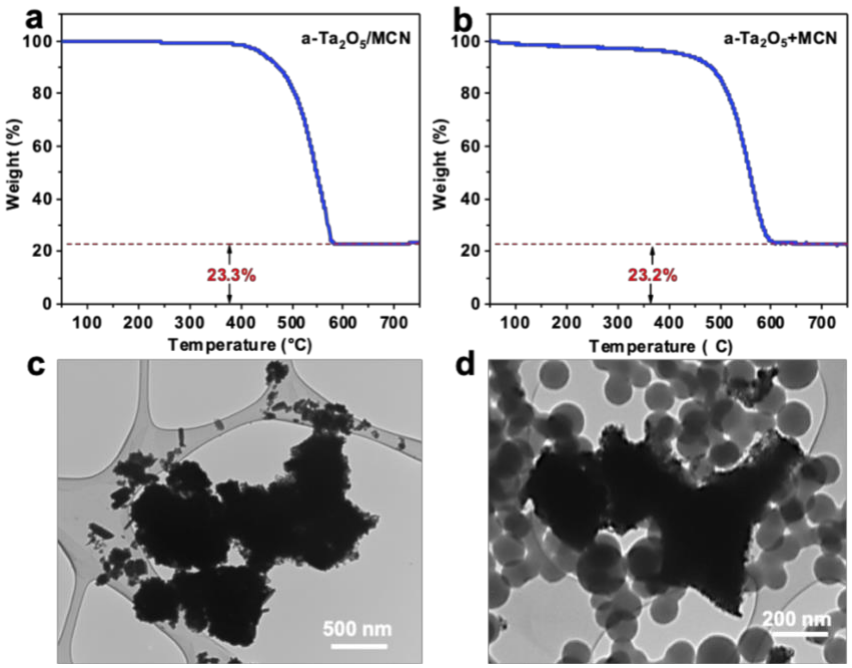

Figure 4.3 TGA curves of (a) a-Ta_2O_5/MCN and (b) a-Ta_2O_5+MCN. TEM images of (c) a-Ta_2O_5 and (d) a-Ta_2O_5+MCN.

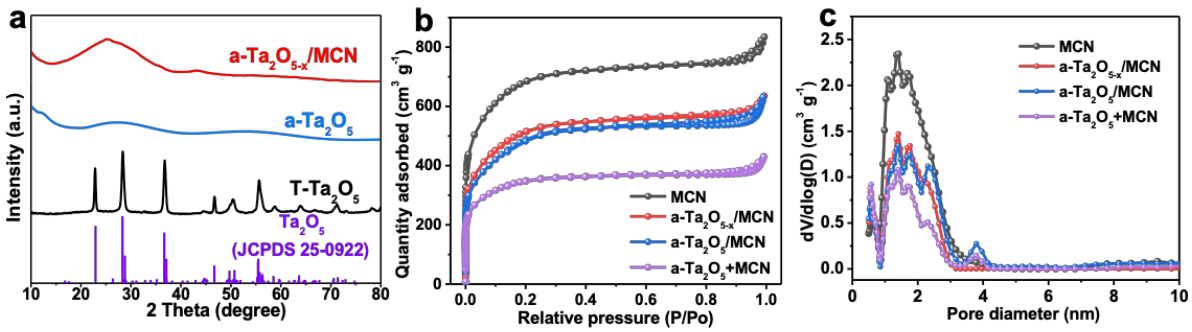

Figure 4.4 (a) XRD patterns, (b) N_2 adsorption-desorption isotherms, and (c) PSD plots of various samples.

The pore structures of as-prepared samples were studied by N_2 adsorption-desorption analysis. A characteristic type-I and type-II combined adsorption isotherm in Figure 4.4b reveals the dominant microporous nature of MCN,[46] which exerts a pore volume of 1.52 cm^3 g^{-1} and specific surface area of 2501 m^2 g^{-1}. The narrow PSD (Figure 4.4c) of MCN (ca. 1.3

nm) coincides with the size of Ta_2O_{5-x} nanoclusters implanted inside pores. The desirable pore size is capable of potently immobilizing Ta_2O_{5-x} nanoclusters to prevent their detachment, and restricting their nucleation process to tune crystallinity. After loading of Ta_2O_{5-x} nanoclusters, the a-Ta_2O_{5-x}/MCN inherits well the original porous structure of MCN, but with a slight reduction in pore volume (1.23 $cm^3\ g^{-1}$) and surface area (1880 $m^2\ g^{-1}$). Besides, a-Ta_2O_5/MCN also shows consistent isotherm with a similar adsorption plateau to a-Ta_2O_{5-x}/MCN. a-Ta_2O_5/MCN possesses a high surface area of 1846 $m^2\ g^{-1}$ and pore volume of 1.20 $cm^3\ g^{-1}$, both of which are close to those of a-Ta_2O_{5-x}/MCN with 1880 $m^2\ g^{-1}$ and 1.23 $cm^3\ g^{-1}$, respectively. The consistent shapes of sorption isotherms and PSD curves with the same peak position between MCN, a-Ta_2O_{5-x}/MCN and a-Ta_2O_5/MCN strongly manifest that Ta_2O_5 nanoclusters root inside the pores. Owing to the strong physical and chemical confinements of the structure, the Ta_2O_{5-x}-loaded micropores can effectively restrain the dissolution of LPS in organic electrolyte. In contrast, a-Ta_2O_5+MCN shows a different PSD plot with decreased pore volume and surface area, implying that the non-uniform mechanical mixing may cause the blockage of pores, and thus lower the porosity.

The defect engineering strategy by introducing oxygen vacancies into amorphous Ta_2O_{5-x} aims to improve the intrinsic conductivity and enhance the electrocatalytic activity for sulfur species. In the XPS spectra of Ta 4f (Figure 4.5a), a-Ta_2O_5/MCN exhibits the Ta $4f_{7/2}$ and $4f_{5/2}$ peaks at 26.6 and 28.5 eV, respectively, confirming the dominant oxidation state of Ta^{5+}.[188] While for a-Ta_2O_{5-x}/MCN, these two peaks shift to lower BE of 26.0 and 27.8 eV, respectively, implying the lower valence state of Ta species arising from the oxygen vacancies. In the O 1s spectra (Figure 4.5b), three deconvoluted peaks (O1, O2, O4) appear on both of a-Ta_2O_{5-x}/MCN and a-Ta_2O_5/MCN. For the strongest O1 peak, it appears at 530.3 eV in a-Ta_2O_5/MCN

ascribed to the Ta-O bond,[189] while there is a positive shift toward a higher BE (530.8 eV) in a-Ta_2O_{5-x}/MCN, strongly evidencing the modified chemical state of Ta-O bond induced by the successful introduction of oxygen vacancies. Besides, the shoulder O2 peak centered at around 531.5 eV indicates the hydroxylated surface, which is conducive to attracting polysulfides;[190] O4 peak appearing at 533.1 eV is associated with the adsorbed moisture.[191] It is particularly noteworthy that a-Ta_2O_{5-x}/MCN presents a distinct O3 peak emerging at 532.4 eV, which is attributed to defects with a low oxygen coordination.[192] This directly suggests the formation of oxygen defects in a-Ta_2O_{5-x}/MCN, which can be further corroborated by EPR spectroscopy (Figure 4.5c). a-Ta_2O_{5-x}/MCN shows a conspicuous signal with a g value of 2.003, signifying the higher oxygen-vacancy concentration in a-Ta_2O_{5-x}/MCN compared with that of a-Ta_2O_5/MCN.[193] These results all suggest the highly oxygen-deficient nature of a-Ta_2O_{5-x}/MCN.

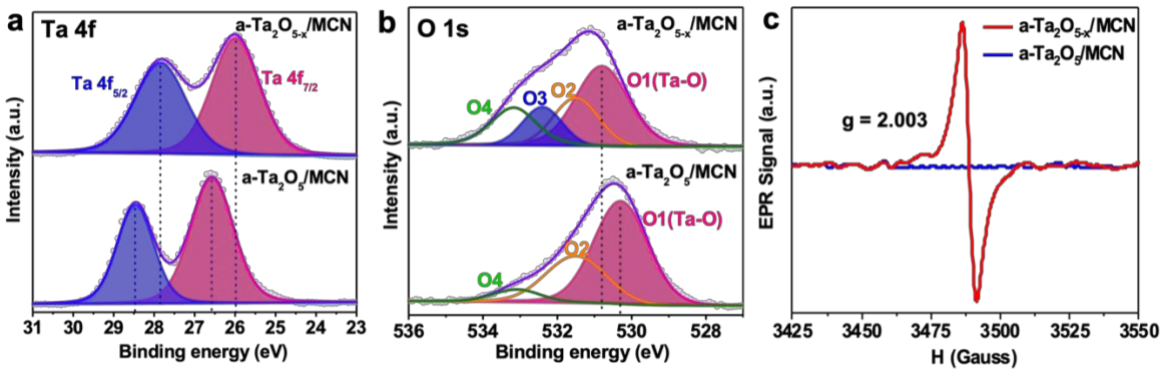

Figure 4.5 High-resolution XPS spectra of (a) Ta 4f, (b) O 1s, (c) EPR patterns for a-Ta_2O_{5-x}/MCN and a-Ta_2O_5/MCN.

Further identifications of the electronic structure and local coordination environment were demonstrated by synchrotron-radiation-based X-ray absorption near-edge structure (XANES) and extended X-ray absorption fine structure (EXAFS) spectroscopy. In the XANES spectra (Figure 4.6a), the absorption edge of a-Ta_2O_{5-x}/MCN is consistent with Ta_2O_5, indicating the

predominant valence state of Ta^{5+}. The white line at the Ta L_3-edge XANES represents the dipolar transition from 2p core levels to unoccupied Ta 5d states.[194] a-Ta_2O_{5-x}/MCN shows the highest white-line intensity, which demonstrates the increased density of Ta 5d unoccupied states near the Fermi level probably induced by the oxygen-vacancy defect.[195] Besides, the Ta L_3 absorption edge energy (E_0), reflects the CBM.[196] The E_0 of a-Ta_2O_{5-x}/MCN and a-Ta_2O_5/MCN is 9882.75 eV and 9883.82 eV, respectively, which implies a-Ta_2O_{5-x}/MCN possesses a lower CBM, desirable for electron transition. In the Fourier-transformed (FT) k^3-weighted EXAFS as shown in Figure 4.6b, Ta_2O_5 exhibits a single peak with the average bond length of 1.53 Å, corresponding to the Ta-O bond coordination. For a-Ta_2O_5/MCN, benefiting from the spatial confinement effect, the narrow carbon pore restricts the nucleation and growth of Ta_2O_5, thus resulting in an incomplete unit cell with a short-range ordered structure (i.e., amorphous structure). As such, a reduced Ta-O bond length (1.51 Å) can be found in a-Ta_2O_5/MCN. Besides, the oxygen deficient environment in a-Ta_2O_{5-x}/MCN further partially disrupts the incomplete amorphous structure, which may impel Ta-O bond coordination to tend towards octahedral TaO6 (short-range order). As a result, this further shortens the Ta-O bond length (1.47 Å) and enhances the Ta 5d-O 2p orbital overlap with the increased bond covalency around Ta.[197] A Cauchy wavelet transform plot (Figure 4.6c) creates a 2D map of the transform space to highlight the contribution of multiple scattering paths to the EXAFS spectra. The Ta_2O_5 exhibits two scattering paths from R = 1 to 2 Å in the first coordination shell, which correspond to the Ta-O bond coordination of TaO6 octahedra and TaO7 pentagonal bipyramids in the Ta_2O_5 crystal.[198] Despite the fact that the obtained a-Ta_2O_5/MCN nanocluster is amorphous and lacks long-range order, it still exhibits the building blocks of TaO6 and TaO7 polyhedrons inside the incomplete unit cell. A slightly negative shift of radial distance is

observed in a-Ta_2O_5/MCN (Figure 4.7), corresponding to the bond length variation attributed to amorphous structure.[199] With the introduction of oxygen vacancies into Ta_2O_5, the oxygen-deficient environment weakens partial Ta-O coordination and reduces its radial distance, provoking the severe structure distortion,[200] and thus there is only one scattering path corresponding to the dominant TaO6 octahedra present in a-Ta_2O_{5-x}/MCN (Figure 4.6c).

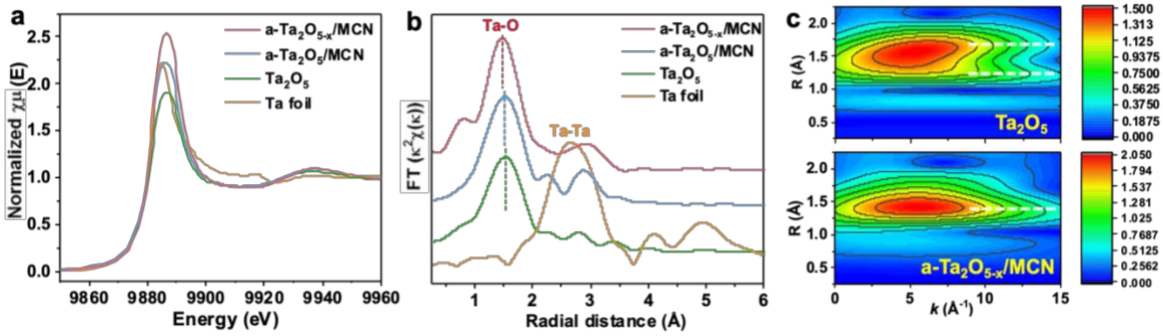

Figure 4.6 (a) Ta L_3-edge XANES spectra, (b) FT k^3-weighted Ta L_3-edge EXAFS spectra of various samples, (c) wavelet transforms for the k^3-weighted Ta L_3-edge EXAFS signals of a-Ta_2O_{5-x}/MCN and Ta_2O_5.

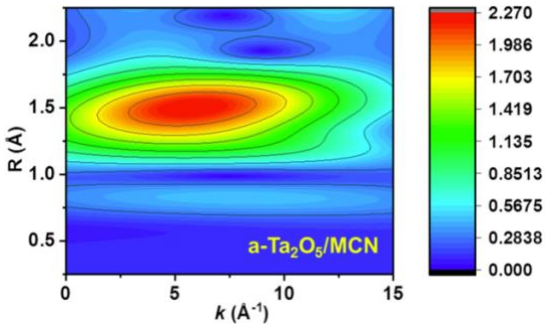

Figure 4.7 Wavelet transforms for the k^3-weighted Ta L_3-edge EXAFS signal of a-Ta_2O_5/MCN.

To elucidate the role of oxygen vacancies in the electrical conductivity, valence band XPS was performed to investigate the electron band configuration. Figure 4.8a exhibits the valence band XPS spectra and shows the edge of the maximum energy located at 2.39 eV for a-

Ta_2O_5/MCN; while the VBM of a-Ta_2O_{5-x}/MCN moves toward 1.80 eV. Such a blue-shift can be associated with band bending for promoted charge transfer induced by oxygen vacancies.[183] The Kubelka-Munk plot (Figure 4.8b) demonstrates the band gap values of a-Ta_2O_5/MCN and a-Ta_2O_{5-x}/MCN are 4.50 and 3.80 eV, respectively. The narrower band gap of defect-engineered a-Ta_2O_{5-x}/MCN confirms the efficient band engineering. Accordingly, the energy band diagram is illustrated in Figure 4.8c. a-Ta_2O_{5-x}/MCN presents a lower CBM than a-Ta_2O_5/MCN, which coincides with the XANES results. Another control sample, a-Ta_2O_{5-x}, was prepared via the same method as a-Ta_2O_5 except for annealing in the H_2 atmosphere to introduce oxygen vacancies. As shown in Figure 4.8d, the oxygen-deficient a-Ta_2O_{5-x} possesses much higher electrical conductivity of 2.1×10^{-2} S m^{-1} than a-Ta_2O_5 with 4.2×10^{-7} S m^{-1} and T-Ta_2O_5 with 3.4×10^{-7} S m^{-1}. This demonstrates the crucial role of oxygen vacancies on improving the intrinsic electrical conductivity of Ta_2O_5. In addition, the impact from carbon-defect structure was excluded by Raman spectroscopy (Figure 4.9). Both a-Ta_2O_5/MCN and a-Ta_2O_{5-x}/MCN present similar D/G intensity ratio, indicating their similar degree of carbon defects which could not contribute to the distinction on band configuration.[5] These evidences indicate that oxygen vacancies lead to the formation of new electronic states located in the band gap of Ta_2O_5, which leads to the enhancement of electrical conductivity and fast electron transfer for sulfur electrochemistry.

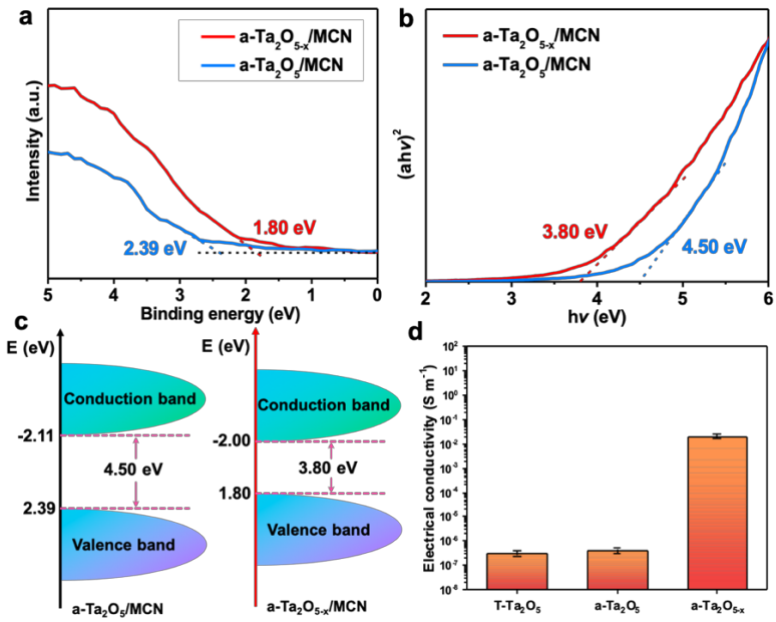

Figure 4.8 (a) Valence band XPS spectra, (b) Kubelka-Munk plot, (c) band diagram of a-Ta_2O_{5-x}/MCN and a-Ta_2O_5/MCN. (d) Electrical conductivities of T-Ta_2O_5, a-Ta_2O_5, and a-Ta_2O_{5-x}.

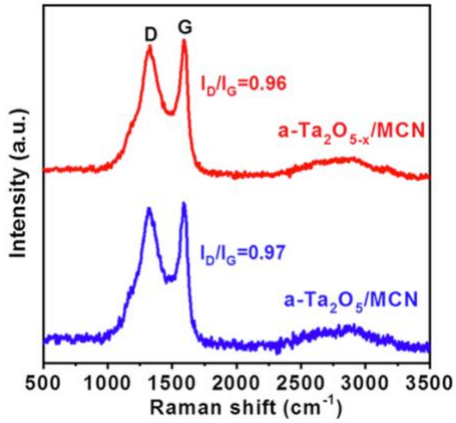

Figure 4.9 Raman spectra of a-Ta_2O_{5-x}/MCN and a-Ta_2O_5/MCN.

UV-vis and XPS measurements were performed to elucidate the LPS adsorption abilities toward enhanced sulfur entrapment. As shown in Figure 4.10a, the UV-vis spectrum of the pristine Li_2S_6 shows two peaks at 275 and 422 nm, which can be assigned to S_6^{2-} and S_4^{2-}, respectively.[201] a-Ta_2O_{5-x}/MCN exhibits the largest reduction in peak intensity, suggesting its strongest LPS adsorption capabilities. In the XPS spectra of S 2p (Figure 4.10b), pristine Li_2S_6

demonstrates two sets of peaks located between 161.8 and 163.3 eV, which correspond to the terminal sulfur (S_T) and bridging sulfur (S_B) of LPS, respectively.[202] After interacting with a-Ta_2O_{5-x}/MCN, a large positive shift can be observed in LPS@a-Ta_2O_{5-x}/MCN, confirming the strong chemical interactions between a-Ta_2O_{5-x}/MCN and LPS. Two pairs of broad peaks emerging at the high BE region can be assigned to the formation of sulfite and sulfate on the surface, which offers strong chemical interaction to LPS.[203] Besides, the O1 peak of LPS@a-Ta_2O_{5-x}/MCN in Figure 4.10c shifts toward higher BE corresponding to the reduced electron cloud density of oxygen, demonstrating the "lithium bond"-like interaction.[204] The O2 and O3 peaks shift towards lower BE, revealing the coordination between sulfur and oxygen-vacancies, corresponding to LPS adsorption on defects.[205] The enhanced LPS adsorption of amorphous and defective structure were examined by DFT calculations based on the Vienna ab initio Simulation Package (VASP) (Figure 4.10d-f). The configuration optimization of a-Ta_2O_5 was based on the T-Ta_2O_5 configuration where all atoms were allowed to relax. T-Ta_2O_5 and a-Ta_2O_5 employed the same cleave surface for comparing their surface adsorbability. The crystalline T-Ta_2O_5 (001) shows a relatively low Li_2S_6 adsorption energy (E_{ads}) of -0.83 eV with a Li-O bond length of 2.52 Å, corresponding to its limited chemical confinement of LPS. Meanwhile, a-Ta_2O_5 exhibits a stronger E_{ads} of -1.22 eV and shorter Li-O bond length of 2.25 Å, suggesting enhanced LPS adsorption capability of amorphous structure. The higher adsorption energy of amorphous structure could be attributed to the polar surface rearrangement, which strengthens the chemical affinity to LPS. Moreover, the defective structure greatly improves the Li_2S_6 BE by offering a higher E_{ads} (-2.0 eV) and significantly strengthened Li-O bond (1.86 Å), revealing the excellent LPS confinement on oxygen defects of Ta_2O_{5-x}. The higher E_{ads} of amorphous and defective structure ensures a highly reversible

LPS adsorption-conversion-desorption process, which could be utilized as electrocatalyst to accelerate LPS conversion kinetics in Li-S batteries.[206]

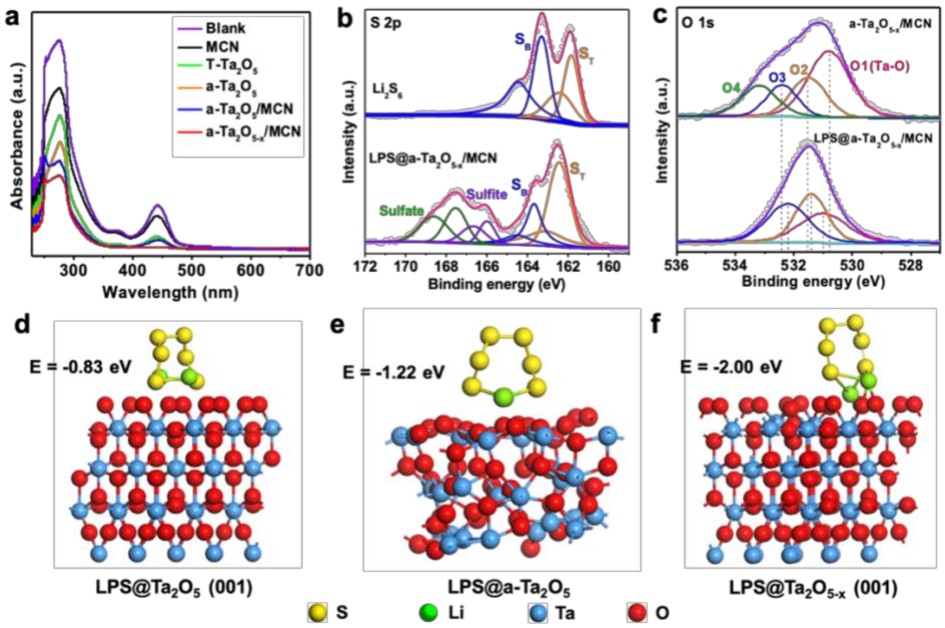

Figure 4.10 (a) UV-vis spectra of LPS solution absorbed by various samples; high-resolution XPS spectra of (b) S 2p for pristine Li_2S_6 and LPS@a-Ta_2O_{5-x}/MCN, (c) O 1s for a-Ta_2O_{5-x}/MCN and LPS@a-Ta_2O_{5-x}/MCN; DFT optimized binding geometric configurations and energies of Li_2S_6 on (d) LPS@Ta_2O_5 (001), (e) LPS@a-Ta_2O_5, (f) LPS@Ta_2O_{5-x} (001).

The corresponding sulfur electrodes of various samples were developed via a melt-impregnation method. The TGA analysis (Figure 4.11a) indicates a sulfur content of 66.2 wt.% in the sulfur composite. As shown in Figure 4.11b, there is no apparent structure change or particle agglomeration after impregnation of sulfur, which was uniformly confined within pores of a-Ta_2O_{5-x}/MCN. As revealed by XRD (Figure 4.11c), a-Ta_2O_{5-x}/MCN/S still exhibits an amorphous structure, and no crystalline S peaks are observed. The characteristic *Fddd* orthorhombic crystal structure peaks of element S disappear from the XRD pattern of a-Ta_2O_{5-x}/MCN/S, which indicates that embedded S existed in ultrafine particles and a highly dispersed

amorphous state. This is due to the spatial confinement of nanosized S inside the micropores, which could have prohibited the crystallization of nanosulfur.[207] In the Raman spectra (Figure 4.11d), the characteristic S-S band of the a-Ta_2O_{5-x}/MCN/S is not detected, which coincides with the XRD results. The above evidences confirm that S was strongly confined within the micropores of a-Ta_2O_{5-x}/MCN/S in a homogenous distribution and was hardly exposed to the external surface by virtue of the pitaya-like architecture.

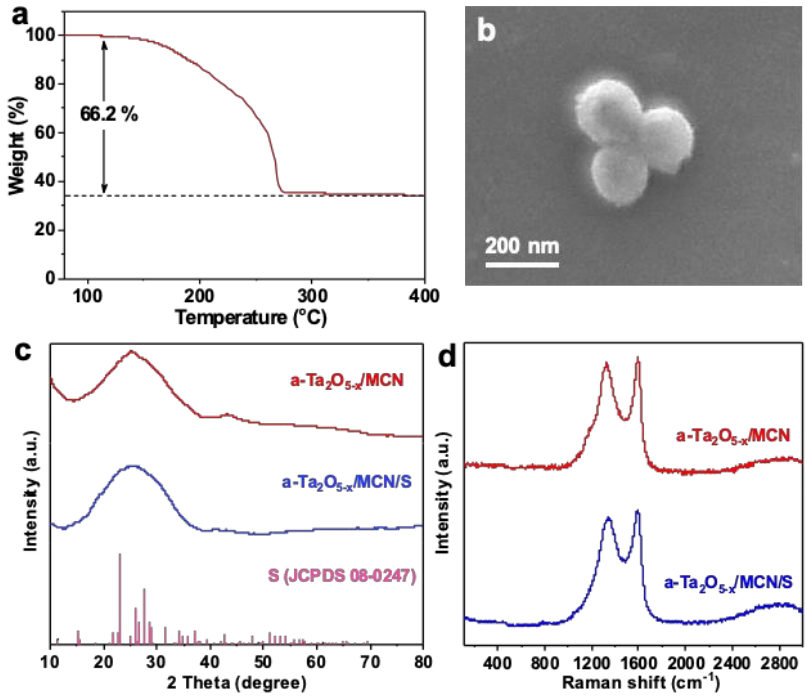

Figure 4.11 (a) TGA curve and (b) SEM image of a-Ta_2O_{5-x}/MCN/S. (c) XRD patterns and (d) Raman spectra of a-Ta_2O_{5-x}/MCN and a-Ta_2O_{5-x}/MCN/S.

The ex situ Ta L_3-edge XANES and EXAFS of a-Ta_2O_{5-x}/MCN/S at different applied potentials in the first cycle were used to determine the valence and chemical environment change during charge-discharge process. In XANES spectra (Figure 4.12a), a-Ta_2O_{5-x}/MCN/S shows the white line peaks of 9886.3 eV at status i, ii, which positively shift to 9887 eV at status iii, iv and shifts back to 9886.8 eV at status v, indicating the reversible Ta valence change

during the lithiation-delithiation process. Correspondingly, the FT k^3-weighted EXAFS spectra (Figure 4.12b) reveal a short radial distance of 1.47 Å at status i, ii and enlarge to 1.53 Å at status iii and iv, confirming strong chemical interaction between LPS and a-Ta_2O_{5-x}/MCN. Moreover, the radial distance switches back to 1.43 Å after charging to 2.6 V (status v). The reversible bond length variation suggests the reversibility of structure change during charge-discharge process, revealing the stability of oxygen-deficient structure.

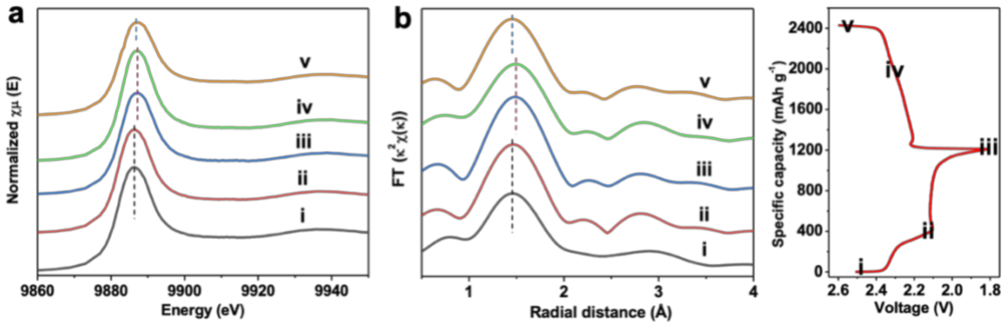

Figure 4.12 Ex situ Ta L_3-edge (a) XANES spectra and (b) FT k^3-weighted Ta L_3-edge EXAFS spectra of a-Ta_2O_{5-x}/MCN/S at different discharge/charge states in first cycle: i) pristine, discharge to ii) 2.1 V, iii) 1.8 V, and charge to iv) 2.3 V, v) 2.6 V.

The above evidences imply that a-Ta_2O_{5-x}/MCN could function as a promising electrocatalyst for sulfur redox reactions. The nanopores loaded with amorphous Ta_2O_{5-x} nanoclusters function as a 3D nanoreactor for fast and durable LPS catalytic conversion (Figure 4.13a). Symmetrical cells were assembled using a-Ta_2O_{5-x}/MCN, a-Ta_2O_5/MCN and a-Ta_2O_5+MCN identical electrodes and Li_2S_6 electrolyte to investigate the LPS conversion kinetics. As displayed in Figure 4.13b, a-Ta_2O_{5-x}/MCN presents strong redox peaks with the highest current response among different samples, suggesting its faster and more efficient LPS conversions. Besides, EIS spectra shows the lowest electrochemical resistance for a-Ta_2O_{5-x}/MCN (Figure 4.13c), further confirming its fast charge transfer and facile sulfur redox

reactions. In addition, three-electrode LSV measurements were conducted to specifically investigate the Li_2S oxidization behavior (Figure 4.13d). a-Ta_2O_{5-x}/MCN delivers the highest current response and the lowest onset potential of -0.56 V in comparison with a-Ta_2O_5/MCN (-0.45 V) and a-Ta_2O_5+MCN (-0.4 V), implying the lowest energy barrier for Li_2S oxidation conversion and revealing the superior catalytic activity of a-Ta_2O_{5-x}/MCN. This result can be further supported by the Tafel plot (Figure 4.13e), which shows a much smaller Tafel slope of 117 mV dec^{-1} for a-Ta_2O_{5-x}/MCN compared with those for a-Ta_2O_5/MCN (166 mV dec^{-1}) and a-Ta_2O_5+MCN (348 mV dec^{-1}), confirming the remarkable kinetic enhancement owing to the defect-rich and Ta_2O_{5-x}-loaded nanoreactor design. All these results strongly reveal the superior catalytic activity of the a-Ta_2O_{5-x}/MCN toward expedited LPS conversion.

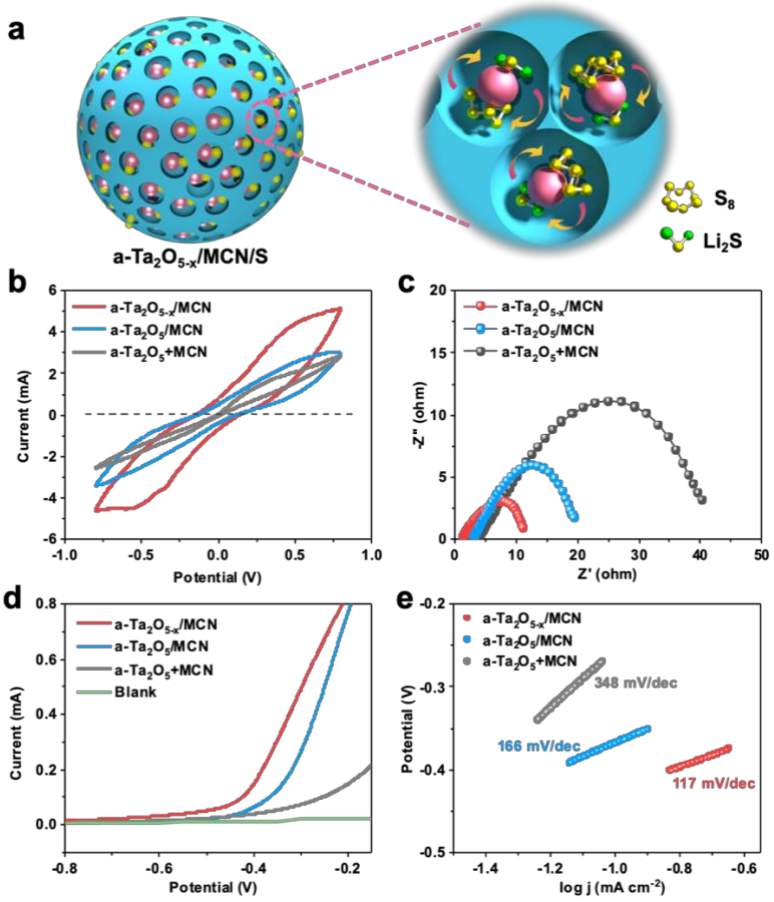

Figure 4.13 (a) Scheme illustration of LPS catalytic conversion in nanoreactor; (b) CV curves, (c) EIS spectra of Li_2S_6 symmetrical cells, (d) LSV curves, (e) Tafel plots of Li_2S oxidization on a-Ta_2O_{5-x}/MCN, a-Ta_2O_5/MCN and a-Ta_2O_5+MCN.

Electrochemical evaluations were performed to demonstrate the enhanced Li-S performances for a-Ta_2O_{5-x}/MCN/S. The charge-discharge profiles of sulfur composites display two plateaus curves (Figure 4.14a). The discharge plateaus at 2.3 and 2.1 V (vs. Li^+/Li) are associated with the electroreduction of sulfur into long-chain LPS and further reduction to Li_2S_2/Li_2S, corresponding to the CV results that show two major reduction peaks and two oxidation peaks (Figure 4.15a). Compared with T-Ta_2O_5/S, the a-Ta_2O_5/S electrode displays higher discharge capacity and smaller polarization, suggesting the contribution of amorphous structure to improved Li-S performance. Moreover, a-Ta_2O_{5-x}/MCN/S exhibits the lowest potential hysteresis in charge-discharge profiles and CV curve with enhanced discharge capacity (around 1200 mAh g^{-1}) and current response, respectively. The defect-rich amorphous Ta_2O_5 implanted within the interconnected micropores of MCN strengthens its ionic/electronic conductivity, which acts as the nanoreactor to accelerate LPS redox reaction, leading to fast and durable electrochemical performance. Figure 4.14b exhibits the Nyquist plots of various sulfur electrodes, where the semicircle at the medium frequency region corresponds to the charge-transfer impedance, and the slope at low frequency region corresponds to Warburg impedance for diffusion process.[208] a-Ta_2O_{5-x}/MCN/S presents the smallest charge-transfer and Warburg resistance, indicating its best charge and mass transfer features. The rate performances and corresponding charge-discharge profiles are displayed in Figure 4.14c and d. a-Ta_2O_{5-x}/MCN/S delivers the best rate performance with the highest discharge capacity of 766 mAh g^{-1} at 5 C compared with a-Ta_2O_5/MCN/S (600 mAh g^{-1}) and a-Ta_2O_5+MCN/S (380 mAh g^{-1}),

and the reversible capacity of 1080.9 mAh g^{-1} when current returns to 0.2 C. These results congruously confirm that the enhanced catalytic activity and kinetics for LPS conversion are due to the elaborate design of a-Ta_2O_{5-x}/MCN/S composite. The cycling performances are compared at a current density of 0.2 C (Figure 4.14e). a-Ta_2O_{5-x}/MCN/S presents the best cyclability with a high discharge capacity of 913.7 mAh g^{-1} and high coulombic efficiency after 300 cycles. In the long-term cycling testing, a-Ta_2O_{5-x}/MCN/S exhibits superior cyclic stability over 1000 cycles with a remarkably low capacity fading rate of 0.029% per cycle (Figure 4.14g). As shown in Figure 4.15b, a-Ta_2O_{5-x}/MCN/S still exhibits a decent capacity of 680 mAh g^{-1} after 1000 cycles. This performance is very competitive compared with other reported electrodes based on transition metal/porous carbon composites (Table 4.1). a-Ta_2O_{5-x}/MCN with a pitaya-like nanoreactor guarantees sulfur homogenization and facilitated ion/electron conduction, and offers strong chemical and physical confinements to suppress LPS shuttle effect. The successful introduction of oxygen vacancies further improves electronic conduction within electrode and provides electrocatalytic sites promoting the chemical interaction with LPS and sulfur redox kinetics.

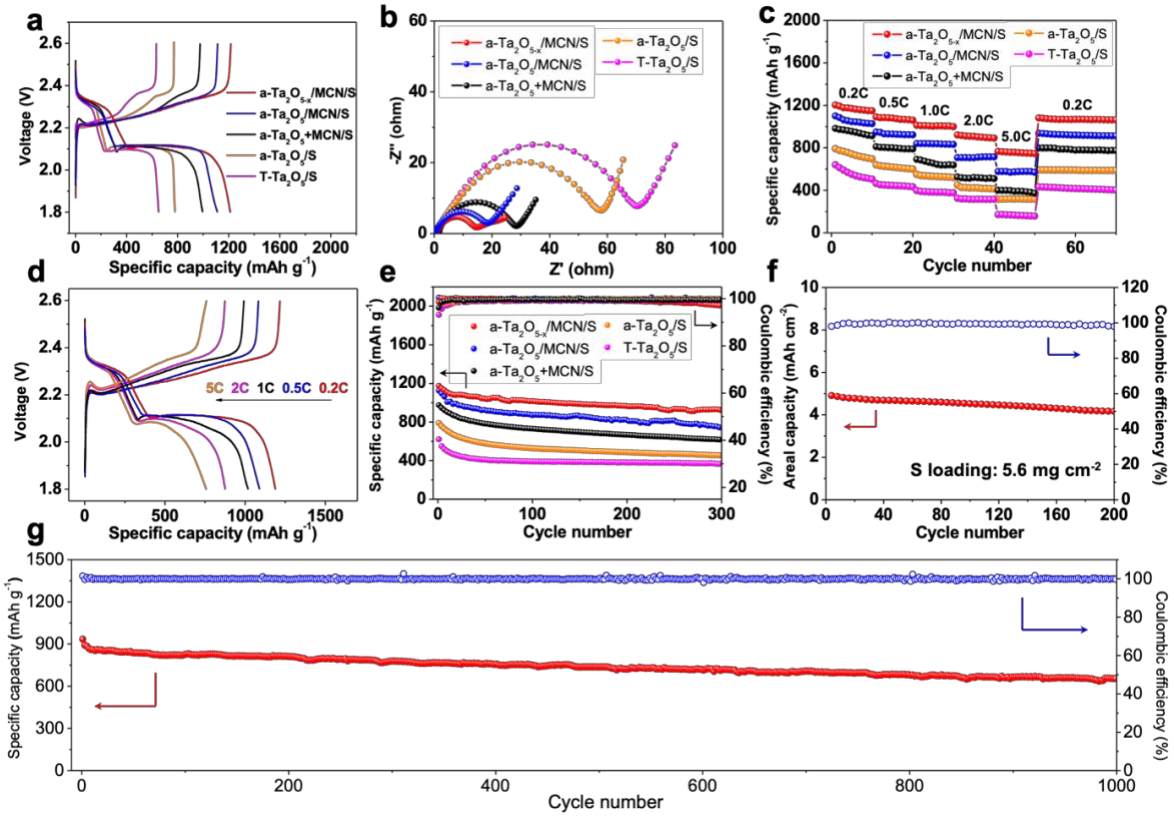

Figure 4.14 (a) Charge-discharge profiles at 0.2 C, (b) Nyquist plots, (c) rate performance, (e) cycle performances at 0.2 C of various sulfur electrodes. (d) Multi-rate discharge-charge profiles, (f) areal capacities and cycle performances with high sulfur loading of 5.6 mg cm^{-2} and low E/S ratio of 3.6 mL g^{-1} at 0.2 C, and (g) long cycling performances at 1 C of a-Ta_2O_{5-x}/MCN/S electrode.

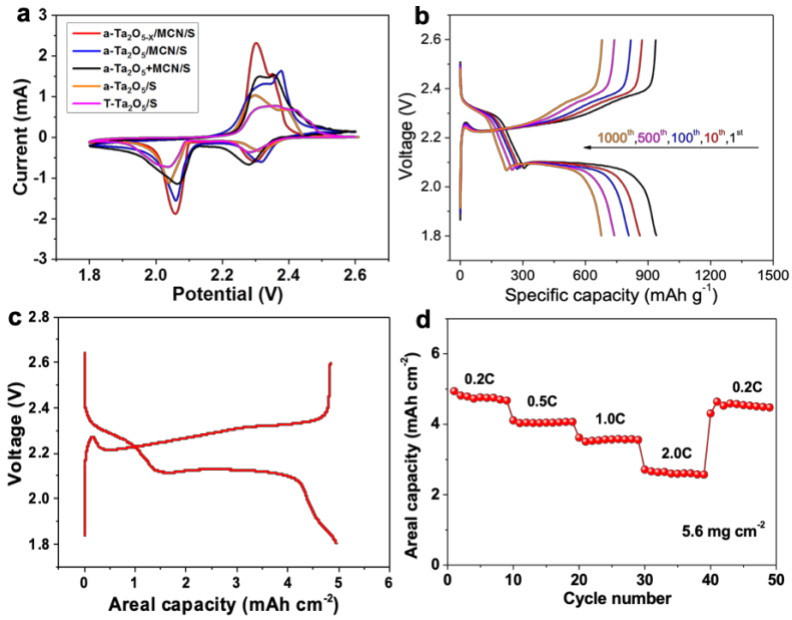

Figure 4.15 (a) CV curves of various sulfur electrode materials. (b) Charge-discharge profiles of long cycling for various cycles of a-Ta_2O_{5-x}/MCN/S electrode at 1 C. (c) Galvanostatic discharge-charge profile at 0.2 C and (d) rate performance of a-Ta_2O_{5-x}/MCN/S electrode under raised sulfur loading of 5.6 mg cm^{-2} and decreased E/S ratio of 3.6 mL g^{-1}.

High sulfur loading and low electrolyte/sulfur (E/S) ratio are critical for achieving high areal capacity and energy density toward Li-S battery practicalization. The charge-discharge profile of a-Ta_2O_{5-x}/MCN/S electrode for high-sulfur-loading performance (Figure 4.15c) delivers a high areal capacity (5 mAh cm^{-2}) under high sulfur loading (5.6 mg cm^{-2}) and low E/S ratio (3.6 mL g^{-1}). a-Ta_2O_{5-x}/MCN/S exhibits an excellent cyclability with high areal capacity over 4 mAh cm^{-2} after 200 cycles (Figure 4.14f). The rate performance of a-Ta_2O_{5-x}/MCN/S was also investigated at the practically relevant condition. As shown in Figure 4.15d, a-Ta_2O_{5-x}/MCN/S delivers a decent capacity over 2.5 mAh cm^{-2} under a high current density of 2 C, and the reversible capacity of 4.7 mAh cm^{-2} when current returns to 0.2 C. The excellent cyclability and rate capability of a-Ta_2O_{5-x}/MCN/S benefit from its potent shuttling

inhabitation and superior electrocatalytic activity and kinetics for fast LPS conversion to facilitate sulfur utilization. These results reveal a good promise in practical application of Li-S batteries.

Table 4.1 Performance comparison with other sulfur electrodes based on metal compounds implanted within carbon

Sulfur host	Cycle number	Rate	Capacity fading rate	Reference
a-Ta_2O_{5-x}/MCN/S	**1000**	**1C**	**0.029%**	**This work**
$Na_2Fe[Fe(CN)_6]$@PEDOT/S	100	2C	0.15%	[209]
$Ti_3C_2T_x$@Meso-C/S	300	0.5C	0.14%	[210]
RGO/C-Co-S	300	1C	0.074%	[211]
TiO_2@NC/S	500	1C	0.058%	[212]
$ZnCo_2O_4$@N-RGO/S	200	0.5C	0.2%	[213]
Co-N-PCNSs/S	200	1C	0.09%	[214]
NbS_2@IG/S	350	0.5C	0.075%	[215]
TSC/NbC/S	500	0.1C	0.037%	[216]
Rf-TiN/S	800	1C	0.039%	[217]

4.4 Conclusions

Taking advantage of the electronic properties specific to tantalum, we developed amorphous tantalum oxide with oxygen vacancies implanted inside a microporous carbon matrix as a new electrocatalyst for polysulfide catalysis and retention. Carbon nanopores restrict the nucleation of Ta_2O_{5-x} nanoseeds to shape the incomplete unit cell in an amorphous structure with enlarged

active surfaces, which reduces the Ta-O bond length and provides strong chemical affinity for LPS. The oxygen vacancies further tune the Ta-O local coordination environment and electron band structure of Ta_2O_{5-x} to improve the intrinsic electrical conductivity and function as catalytic centers. The engineered 3D conductive nanoreactor loaded with Ta_2O_{5-x} nanoclusters efficiently inhibits LPS shuttling and promotes LPS catalyzation with fast redox kinetics. Meanwhile, the sulfur agglomeration and volume expansion are well suppressed in the pitaya-like structure. These featuring superiorities endow the developed sulfur electrode with outstanding rate capability and cyclability even at practically relevant sulfur loading and electrolyte content. We believe our identification of tantalum as a new catalyst material for Li-S batteries will stimulate more efforts on the specific selection of transition metals based on their electronic structures. The unique "ship in a bottle" strategy offers the guidance for rational structural design in energy conversion and storage systems.

Chapter 5 “Two Ships in a Bottle” Design for Zn−Ag−O Catalyst Enabling Selective and Long-Lasting CO_2 Electroreduction

The “ship in a bottle” concept conceived and developed in Chapter 3 and Chapter 4, respectively, is based on the monometallic design. Chapter 5 further optimizes this concept to a bimetallic design by a “two ships in a bottle” strategy to meet higher electrocatalyst requirements, promisingly enabling selective and durable CO_2 electroreduction.

5.1 Introduction

Electrochemical conversion of CO_2 into value-added chemicals and fuels, coupled with renewable energy sources (e.g., solar photovoltaic, wind, and tide), represents a promising and potent solution to both emission-control and energy-supply challenges toward a sustainable future for humankind.[219,220] As the technoeconomic viability of the direct electrosynthesis of multicarbon products demands considerable decline in overpotentials, the yields of C_1 products (i.e., CO and formate) are more economically practical for electrochemical CO_2 valorization.[220,221] However, the conversion process, involving the transfer of two electrons and protons activation, generally suffers from high thermodynamic and kinetic barriers and unsatisfied selectivity, on account of the restructuring of energy between the extremely stable linear molecule and bent radical anion as well as the difficulty in assembling the nuclei and breaking chemical bonds for the desired products.[222,223] Hence, the fundamental understanding for rationally designing CO_2RR catalysts with enhanced activity, selectivity, and durability is imperative.

Zn-based materials represent one of the most promising non-noble metal catalysts in the CO-generating class, albeit it does not possess optimal levels of activity and selectivity.[224,225] The addition of a second metal to Zn-based materials is an effective theoretical approach to tune the reactivity and selectivity through tailoring the binding strength and binding configuration of intermediates on the catalytic surfaces.[226,227] However, the practical challenge of this strategy is the synthesis of such bimetallic catalysts in a controllable fashion. The design principles rely on the following: (i) exposing abundant catalytically active sites to efficiently stabilize the key intermediates;[10] (ii) constructing heterogeneous interfaces with tunable active centers that have a favorable electronic structure to improve the selectivity;[228] (iii) tailored structure engineering that bolsters the stability of catalysts;[229] and (iv) guaranteeing sufficient porosity for mass transport to expedite the kinetics.[230]

Recently, we proposed a unique "ship in a bottle" concept in catalyst design to impregnate metal nanoparticles/nanoclusters inside the pores of a nanoporous carbon matrix to improve the activity and stability of catalysts. This concept has been applied in a variety of catalytic systems such as ORR,[5,231] OER,[5,232] and polysulfide conversion in Li-S batteries.[7,233] However, such monometallic design confronts big limitations for achieving highly efficient and selective CO_2RR, especially when surviving the associated harsh cathodic potentials. In this study, enlightened by the theoretical analyses of thermodynamic reaction energetics and electronic structure modulation, we strategically develop a bimetallic catalyst comprising ultrafine twinned ZnO and Ag nanoparticles impregnated inside the nanopores of ultrahigh-surface-area carbon nanospheres (ZnO-Ag@UC) for the selective and durable CO_2 reduction to CO, which represents a concept of "two ships in a bottle". This elaborate design demonstrates multiple merits to fulfill the aforesaid principles: (i) The tailored heterointerface between ZnO and Ag

sparks the electron donation from Zn and Ag to O, which tunes the bonding strength with the carbon atom in *COOH, the oxygen atom in HCOO*, and the hydrogen atom in *H and thus significantly improves the selectivity toward CO over formate and H_2. (ii) The ultrahigh-surface-area (4115 $m^2 g^{-1}$) carbon is fabricated as a host to load ultrafine ZnO-Ag nanoparticles with good dispersion inside the nanopores, which controls the particle size and guarantees an ultrahigh surface-to-volume ratio to offer abundant active sites, significantly promoting catalytic activity. (iii) The ZnO-Ag-in-pore structure potently inhibits the agglomeration and detachment of nanoparticles during both synthesis and CO_2RR, greatly prolonging catalyst lifetime. (iv) The interconnected porous conductive network facilitates mass transport and electron mobility throughout the framework, expediting catalytic kinetics. Theoretical calculations and in situ XAS studies unveil the enhanced reactivity and selectivity driven by a combination of geometric and electronic effects. Therefore, this study presents a high-performance ZnO-Ag@UC electrocatalyst that efficiently converts CO_2 into CO at high selectivity (94.1 ± 4.0%) and high energy efficiency (60.9%) over an extended period of time (over 150 h).

5.2 Experimental Section

5.2.1 Computation Methods

The first-principles calculations were based on DFT with the projector augmented wave method as implemented in the VASP.[234–236] Steady surfaces of Ag (111) (containing 64 Ag atoms), ZnO-Ag (containing 80 Zn atoms, 80 O atoms, and 4 Ag atoms), and ZnO (101) (containing 20 Zn atoms and 20 O atoms) with vacuum thickness of 15 Å were used in this work. The Perdew-Burke-Ernzerhof spin-polarized generalized gradient approximation was

used for the exchange-correlation potential. The calculation was performed using generalized gradient approximation by DFT+*U* with *U*-*J* = 9.3 eV for Zn 3d.[237] A G-centered 3 × 3 × 1 k mesh together with an energy cut-off of 400 eV was used in the geometry optimization process and static calculations (7 × 7 × 7 k mesh for density of state calculations). The convergence criteria for the total energy was 10^{-5} eV. All the atoms were relaxed until Hellmann-Feynmann forces on each atom were reduced to less than 0.02 eV·$Å^{-1}$.

The adsorption energy, E_{ads}, was calculated to estimate the strength of a molecule-surface interaction and to seize the most energetically stable adsorption model. The E_{ads} could be calculated by:

$$E_{ads} = E_{system} - E_{surf} - E_{adsorb}$$

where E_{system}, E_{surf}, and E_{adsorb} are the energy of adsorption structure, surface, and adsorbent, respectively.

Free energy changes (ΔG) for the intermediates at P_{H2} = 1 bar, were calculated using:

$$\Delta G = \Delta E + \Delta ZPE - T\Delta S$$

where ΔE is the reaction energy determined from DFT, and ΔZPE is the difference in zero-point energies due to the reaction between the adsorbed and the gas phase by setting H_2O and H_2 in the gas phase as reference states. ΔZPE of various surfaces was calculated using DFT calculations. ΔS is the change in entropy, computed using DFT calculations of the vibrational frequencies and standard tables for gas phase molecules. All values of ΔG were computed at T = 298 K, and pH = 0.

The deformation charge density Δρ(r) was calculated via $\Delta\rho(r) = \Delta\rho_{ZnO\text{-}Ag}(r) - \Delta\rho_{ZnO}(r) - \Delta\rho_{Ag}(r)$, where $\Delta\rho_{ZnO\text{-}Ag}(r)$, $\Delta\rho_{ZnO}(r)$ and $\Delta\rho_{Ag}(r)$ are the electron density of ZnO-Ag, ZnO and Ag group, respectively.

5.2.2 Materials Synthesis

Preparation of Ultrahigh-Surface-Area Carbon (UC). A 55 mL aqueous solution containing 0.65 M glucose underwent the hydrothermal treatment at 190 °C for 350 min. The precipitate was collected and washed by deionized water, followed by vacuum drying at 60 °C overnight. The powder was then added into a small amount of $ZnCl_2$ solution with a mass ratio of 1/5 (powder/$ZnCl_2$) and stirred for 5 h. Then, the suspension was dried at 105 °C to evaporate visible water, followed by the vacuum drying for one day. Next, the solid was ground under the inert atmosphere and quickly transferred to a tube furnace, followed by an initial activation at 500 °C for 1 h under argon atmosphere. The temperature was then raised to 980 °C, after which the gas flow was switched to CO_2 and the activation was continued for several hours. The 2 M HCl was then added to the collected solids under stirring for 1 h; UC was ultimately obtained after washing with ethanol and deionized water.

Preparation of ZnO-Ag@UC. First, 150 μmol mL^{-1} $Zn(NO_3)_2$ ethanol solution was prepared by adding 0.224 g zinc nitrate hexahydrate into 5 mL ethanol; 150 μmol mL^{-1} $AgNO_3$ aqueous solution was prepared by adding 0.128 g silver nitrate into 5 mL deionized water. Subsequently, 184 μL of prepared $Zn(NO_3)_2$ ethanol solution and 139 μL of prepared $AgNO_3$ aqueous solution were simultaneously added to 25 mg of UC under ultrasonication for 250 min. After the vacuum drying overnight, the powder was pyrolyzed in argon atmosphere at 500 °C for 90 min to yield ZnO-Ag@UC. ZnO-Ag@UC based catalysts with various ZnO and Ag ratios (i.e.,

$ZnO_{0.75}$-$Ag_{0.25}$@UC and $ZnO_{0.25}$-$Ag_{0.75}$@UC) were prepared via the same method except for altering the amount of precursor solution.

Preparation of ZnO@UC and ZnO+UC. 368 μL of prepared $Zn(NO_3)_2$ ethanol solution was added to 25 mg of UC under ultrasonication for 250 min. After the same drying and pyrolysis method with ZnO-Ag@UC, ZnO@UC was yielded. As per the ZnO content (15.5 wt%) in ZnO@UC determined by inductively coupled plasma optical emission spectrometer (ICP-OES), ZnO+UC was prepared by mechanical mixing of 16.8 mg zinc nitrate hexahydrate and 25 mg UC, followed by the same pyrolysis process as ZnO@UC to guarantee the same ZnO content as ZnO@UC.

Preparation of Ag@UC. 278 μL of prepared $AgNO_3$ aqueous solution was added to 25 mg of UC under ultrasonication for 250 min. After the same drying and pyrolysis method with ZnO-Ag@UC, Ag@UC was yielded.

Preparation of ZnO-Ag+UC. As per the content of ZnO (7.8 wt%) and Ag (7.5%) in ZnO-Ag@UC determined by ICP-OES, ZnO-Ag+UC was prepared by mechanical mixing of 17 mg zinc nitrate hexahydrate, 7 mg silver nitrate, and 50 mg UC, followed by the same pyrolysis process as ZnO-Ag@UC, to guarantee the same ZnO and Ag content as ZnO-Ag@UC.

Preparation of ZnO-Ag. ZnO-Ag was prepared by mechanical mixing of 53 mg zinc nitrate hexahydrate and 23 mg silver nitrate, followed by the same pyrolysis process as ZnO-Ag@UC.

5.2.3 Materials Characterization

The morphology and microstructures of materials were investigated by SEM with a FEI Quanta FEG 250 ESEM, and TEM and STEM with a Talos F200X G2. The crystal structures were characterized by XRD using a MiniFlex 600 Rigaku diffractometer. Pore structures were

studied by N_2 adsorption-desorption measurements using ASAP 2020 micromeritics; the surface area was calculated using the BET theory, and pore size distribution was determined via the QSDFT method. XPS was conducted with a Thermal Scientific K Alpha spectrometer. The metal content of materials was determined with the ICP-OES. XAS for the Zn K-edge and Ag K-edge was performed on the BioXAS-Spectroscopy (07ID-2) beamline at Canadian Light Source. All the XAS data were processed using the Athena program.

5.2.4 Electrochemical Measurements

CO_2RR was performed in a gas-tight H-type cell with Nafion 117 membrane to separate the two compartments. To prepare the working electrode, 150 µl of homogeneous ink, which was prepared by dispersing 10 mg of the sample and 80 µl Nafion solution (5 wt%) in 1 mL ethanol-water solution with volume ratio of 1:1, was loaded onto carbon paper (Sigracet 29 BC) with dimensions of 1.0 × 1.0 cm. A platinum wire and SCE were employed as counter and reference electrode, respectively. The calibration of the reference electrode to RHE was based on the Nernst equation: $E_{RHE} = E_{SCE} + 0.0591 \times pH + 0.241$. The electrolyte was a 0.5 M $KHCO_3$ solution which was saturated with CO_2 by being purged with CO_2 for 1 h prior to measurement. The CO_2RR was carried out for 2 h at various potentials in the electrolyte. The electrochemical measurements were carried out using a Gamry potentiostat. The current densities reported in this work were normalized to the geometric surface area. Three independent measurements were performed, and the results presented are the averaged values. All the experiments were performed at room temperature and under ambient pressure.

5.2.5 Products Analysis

A 500 MHz ^{1}H liquid nuclear magnetic resonance (NMR) spectrometer (Bruker Advance) using the water suppression method was employed to detect the concentration of reaction products in the liquid electrolyte. On-line gas chromatography (GC, SRI 8610C) was used to quantify gas products. The GC is equipped with a packed Molecular Sieve column and Helium ionization detector. Helium (Praxair Gas, 99.999%) was used as the carrier gas. The Faradaic efficiency (FE) was calculated by the equation as below:

$$FE = \frac{znF}{Q}$$

where z is the number of exchanged electrons in the reaction, n is mole number of the formed product, F is the Faradaic constant, and Q is the amount of passed charge. The partial current density was determined by multiplying FE with the average current density.

5.2.6 Energy Efficiency Calculation

The cathodic energy efficiency (EE_{ca}) for the electroreduction of CO_2 toward CO is calculated using the following equation:[238,239]

$$EE_{ca} = \frac{E_{eq,cell} \cdot FE}{E_{eq,cell} + \eta_{cathode}}$$

Where $E_{eq,cell}$ is the thermodynamic equilibrium potential between the anode and cathode reactions, $E_{eq,cell} = E_{eq,anode} + (-E_{eq,cathode})$ wherein $E_{eq,anode}$ is the thermodynamic equilibrium potential for the anode reaction (i.e. oxygen evolution reaction) equal to 1.23 V (vs. RHE), $E_{eq,cathode}$ is the thermodynamic equilibrium potential for the cathode reaction ($E_{eq,cathode,CO} = -0.11\,V$, $E_{eq,cathode,formate} = -0.03\,V$). $\eta_{cathode}$ is the cathode

overpotential, which is the potential difference between $E_{eq,cathode}$ and the applied cathode potential.

5.3 Results and Discussion

The first-principles calculations based on DFT were conducted to investigate the reaction energetics and atomic interactions within the Zn-Ag-O metal-oxide heterointerface. The facet of (101) was employed for modeling ZnO (Figure 5.1a), which is favorable to stabilize *COOH while possessing a high energy barrier for the competing hydrogen evolution reaction.[240,241] To represent the metallic Ag surface, we used the Ag (111) surface which has been reported to be the most thermodynamically stable facet (Figure 5.1b).[242,243] Accordingly, the modeling for ZnO-Ag was built by arranging a Ag cluster from the Ag (111) facet onto the ZnO (101) surface (Figure 5.1c). All the modeling configurations were optimized by DFT calculations (details are provided in the Experimental Section). Starting from the adsorption of the bicarbonate (CO_3H*) species, which has been demonstrated as the primary carbon source for CO_2 electroreduction,[244,245] we investigated two main pathways for generating CO and formic acid (HCOOH) (Figure 5.2a). *COOH and HCOO* are the key intermediates in the reaction pathway toward CO or HCOOH, with the C atom or O atom bonding to the ZnO-Ag surface, respectively.

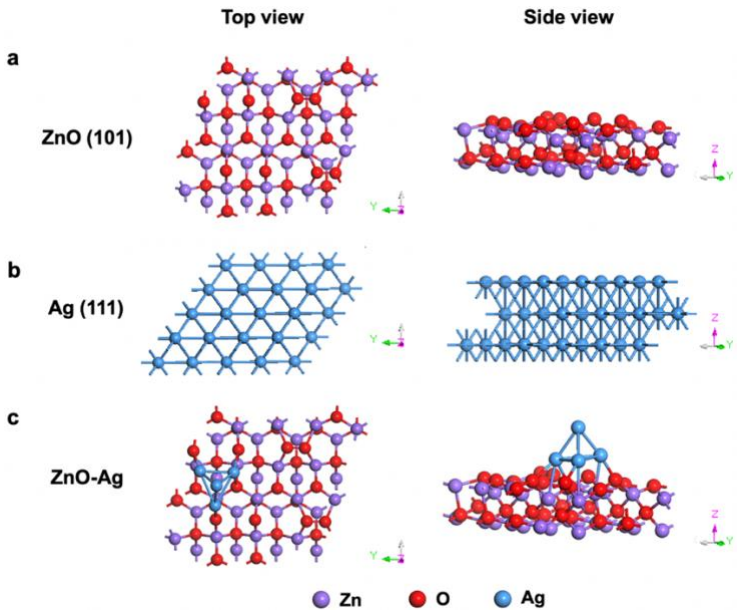

Figure 5.1 DFT optimized model structure from the top and side views for (a) ZnO (101), (b) Ag (111), and (c) ZnO-Ag.

The interactions and electronic structure between Zn, Ag, and O atoms were explored by the calculated charge density reconfiguration as demonstrated in Figure 5.2b. The charge density is depleted around Zn and Ag atoms, while accumulated around O atoms. This infers Zn and Ag atoms tend to delocalize charge by releasing electrons to the O atoms, manifesting the electron transfer effect. The electron density transfer from Zn and Ag to O was further analyzed by the projected density of states (PDOS) (Figure 5.2c-e), which has three important impacts on CO_2RR: (i) Promoting CO production. Compared to the Ag model, the Ag d-band center of ZnO-Ag exhibits a conspicuous upshift toward the Fermi level (Figure 5.2c), which enables the stronger binding ability to the *COOH intermediate, resulting in higher catalytic activity for CO production.[243,246] The calculated free energy profiles also coincide with the PDOS features. As displayed in Figure 5.2f and h, the addition of Ag on the ZnO surface alters the rate-limiting step from α2/β2 to α1/β1, where ZnO-Ag exhibits a lower energy barrier for the

generation of *COOH than for HCOO*. By contrast to the ZnO model, the free-energy step becomes more thermodynamically facile for the second proton-coupled electron transfer for the adsorbed *CO in the ZnO-Ag model. Hence, the Ag decoration on ZnO improves the catalytic activity, facilitating CO production. (ii) Suppressing HCOOH production. Compared with the ZnO model, the Zn d-band and O p-band centers of ZnO-Ag present marked downshifts away from the Fermi level (Figure 5.2d and e), suggesting a strong interaction between Zn, Ag, and O atoms due to the increased electron filling of antibonding states.[247,248] The electron density of Ag atoms is depleted after interfacing with Zn atoms, which enables the ZnO-Ag surface to tune the affinity for HCOO*.[249,250] As revealed by the free energy analysis (Figure 5.2g), the metallic Ag model exhibits overlapping pathways for *COOH and HCOO* in the rate-limiting step (α1/β1), causing poor selectivity. By contrast, ZnO-Ag not only presents a large energy difference between these two competing intermediates (Figure 5.2h), allowing more selective production of CO, but also increases the energy barrier for forming HCOO* to suppress HCOOH generation. (iii) Suppressing H_2 evolution. As displayed in Figure 5.2i, ZnO-Ag exhibits the highest energy barrier in the step of H^+ conversion to adsorbed *H, suggesting that a competitive hydrogen evolution reaction (HER) is more difficult to occur on ZnO-Ag compared to that on ZnO and Ag. The electron density reconfiguration around Zn, Ag, and O atoms in ZnO-Ag significantly weakens the binding of the intermediate *H, resulting in superior inhibition of H_2 evolution.

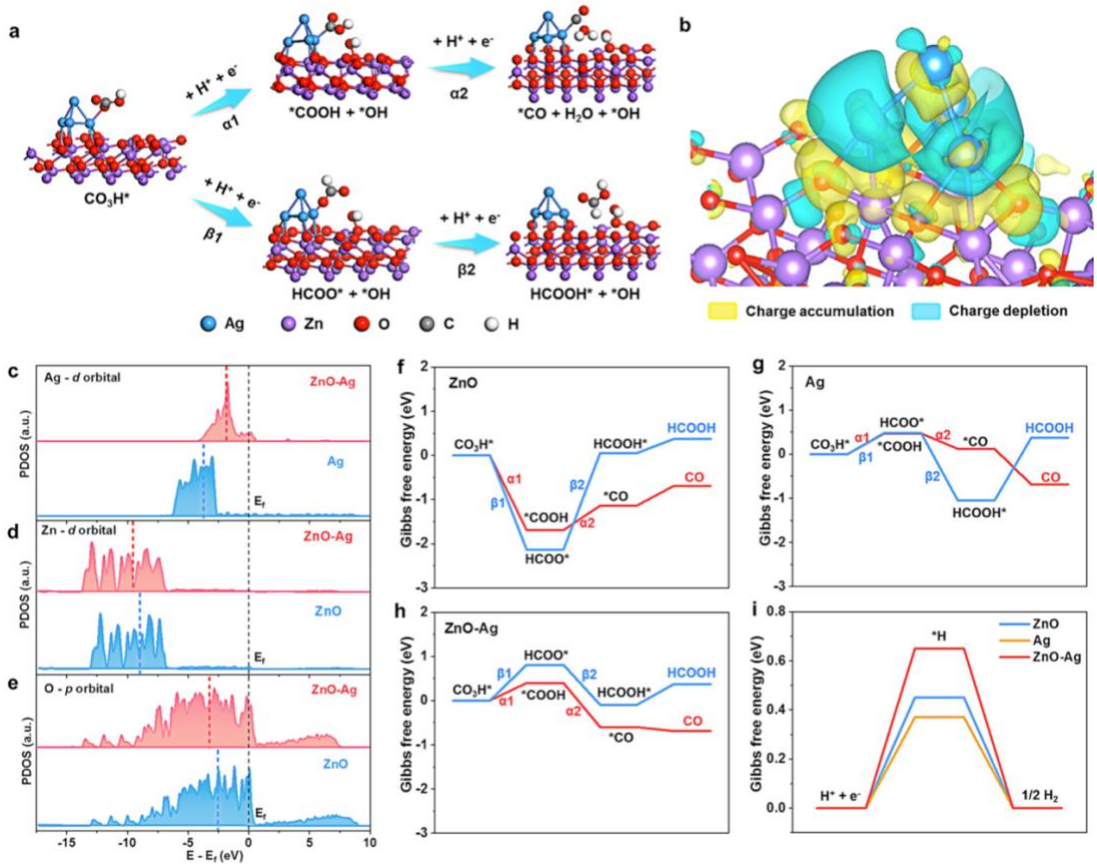

Figure 5.2 Theoretical calculations. (a) Simulation considering two pathways for CO and HCOOH production, respectively. (b) Schematic of calculated charge densities among Zn, Ag, and O atoms. PDOS of the d-band for (c) Ag and (d) Zn atoms and the p-band for (e) O atoms on three various models; black dashed lines indicate the Fermi energy level; red and blue dashed lines indicate the corresponding orbital band centers. Free energy diagrams of CO_2 reduction to CO and HCOOH on the models of (f) ZnO, (g) Ag, and (h) ZnO-Ag and (i) for the HER process on ZnO, Ag, and ZnO-Ag.

As unveiled by theoretical calculations, with proper construction of the Zn-Ag-O heterointerface, Zn and Ag atoms tend to delocalize charge by releasing it to O atoms. This electronic delocalization may unravel the enhancement of activity and selectivity toward CO rather than formate and H_2.

Inspired by the above theoretical calculations, we developed a “two ships in a bottle” design for fabricating ZnO-Ag bimetallic catalyst, whose synthesis strategy is illustrated in Figure 5.3a. First, to guarantee good catalyst dispersion and high active surface area, we prepared ultrahigh-surface-area carbon (UC) nanospheres by an innovative dual-pore-forming technique. Carbonaceous precursors derived from the hydrothermal treatment of glucose underwent a dual-activation process, wherein zinc chloride and CO_2 were employed as the pore-forming agents for simultaneous chemical and physical activation, respectively. The UC possesses regular sphericity with a uniform size of approximately 150 nm (Figure 5.3b and c). Next, a high dispersion of zinc nitrate and silver nitrate precursors implanted inside the UC pores was achieved by means of a wet-impregnation strategy. Following this, the Zn^{2+}-Ag^{+}-impregnated UC underwent pyrolysis in an argon atmosphere where zinc nitrate and silver nitrate completely decomposed to ZnO and Ag, respectively, as per the reactions in Figure 5.3d. The designed bimetallic catalyst comprised ultrafine ZnO and Ag nanoparticles impregnated within the nanopores of UC (ZnO-Ag@UC), illustrating a concept of “two ships in a bottle” (Figure 5.4a).

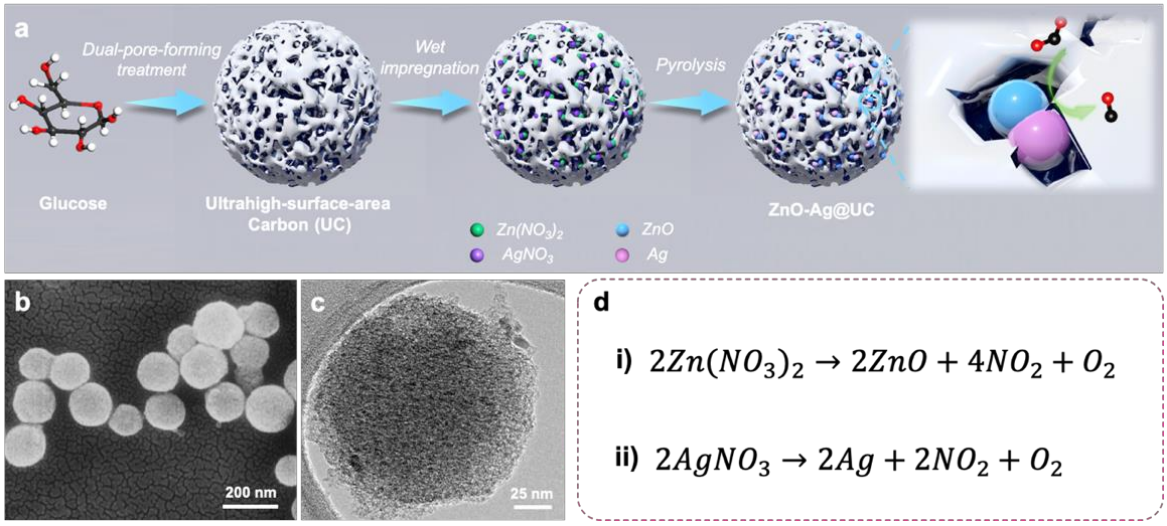

Figure 5.3 (a) Schematic of the synthesis route of ZnO-Ag@UC. (b) SEM image and (c) TEM image of UC. (d)Reaction equations for forming (i) ZnO and (ii) Ag.

SEM imaging of ZnO-Ag@UC presents a spherical morphology with a clean surface and uniform size (Figure 5.4b). There is no particle agglomeration found on the external surfaces of the UC nanospheres. ZnO-Ag@UC maintains a consistent morphology with UC, with no apparent change after the impregnation of ZnO-Ag. TEM imaging (Figure 5.4c) reveals a homogeneous distribution of ZnO-Ag nanoparticles throughout the UC matrix. The HRTEM image in Figure 5.4d distinctly exhibits a zone of interfacial contact between two different crystal plane structures with lattice interplanar spacings of 0.23 and 0.25 nm, corresponding to the (111) plane of Ag and the (101) plane of ZnO, respectively. FFT patterns (Figure 5.4e and f) in the interfacial region manifest the presence of segregated Ag and ZnO rather than an alloyed interface with Ag and Zn atoms interdiffusion. As illustrated by the HAADF-STEM imaging (Figure 5.4g), bright ZnO-Ag nanoparticles are uniformly accommodated within the pores of UC with an average size of 3.1 nm. It is noteworthy that such small nanoparticles could be maintained in high-temperature pyrolysis by virtue of the strong spatial confinement effect of the UC pores that potently prohibit ZnO-Ag nanoparticles from agglomeration. The tailored bimetallic heterointerfaces are also identified in the HAADF-STEM image (Figure 5.4h) and corresponding EDS mapping (Figure 5.4i-n). It clearly shows that the two discrete phases of Ag and ZnO are twinned in one nanoparticle, and the entire nanoparticle is embedded within the UC framework, which offers an interconnected porous conductive network to expedite mass transport and electron mobility. This evidence demonstrates the successful impregnation of ultrafine ZnO-Ag nanoparticles within the UC pores with the well-tailored Zn-Ag-O heterointerfaces. ICP-OES reveals the content of Ag (7.5 wt%) and Zn (6.3 wt%), by

which the ZnO content is calculated to be 7.8 wt%; thus Ag and ZnO have an almost identical mass loading in ZnO-Ag@UC.

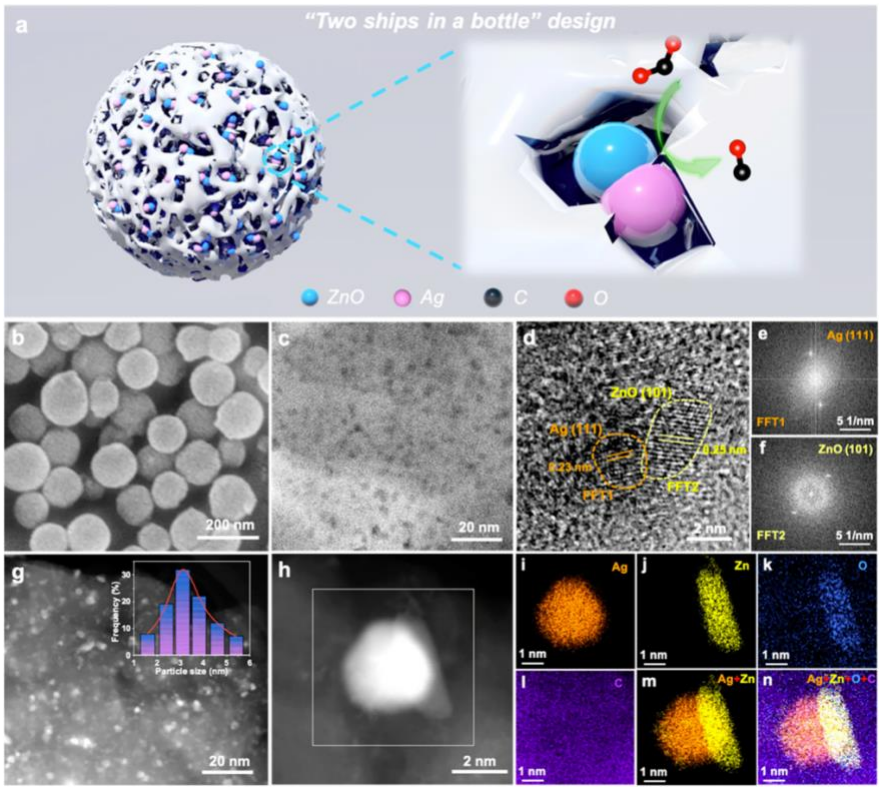

Figure 5.4 Design concept and structural characterizations. (a) Schematic of the "two ships in a bottle" design. (b) SEM image, (c) TEM image, (d) HRTEM image, and corresponding FFT diffraction patterns for (e) Ag (111) and (f) ZnO (101), (g) HAADF-STEM image (inset: size distribution histogram), (h) HAADF-STEM image, and (i-n) corresponding EDS element mapping of individual twinned ZnO-Ag nanoparticle accommodated within carbon pores of ZnO-Ag@UC.

XRD patterns confirm the coexistence of ZnO and Ag phases in ZnO-Ag@UC with the predominant crystal planes of (101) and (111), respectively (Figure 5.5a), which correspond with the modeling of theoretical calculations. To investigate the important role of introducing

Ag to engineer ZnO-Ag heterointerfaces for CO_2RR, we also obtained a control sample, ZnO@UC, by implanting only a zinc nitrate precursor into the UC pores followed by the same pyrolysis treatment as ZnO-Ag@UC. The ZnO loading in ZnO@UC is 15.5 wt%, which is calculated from the Zn content of 12.5 wt% according to ICP-OES. ZnO@UC possesses a pure ZnO crystal structure as confirmed by XRD (Figure 5.5a). The HAADF-STEM image and corresponding EDS mapping for ZnO@UC explicitly show that the ultrafine ZnO nanoparticles are impregnated within the carbon pores, while maintaining a homogeneous distribution throughout the UC matrix (Figure 5.5b-f). This strongly validates the general feasibility of our developed "ship in a bottle" design concept. To further demonstrate the structural merits of our design, we prepared another control sample, ZnO+UC, by mechanically mixing zinc nitrate solid with UC, followed by the same pyrolysis process. The ZnO content of ZnO+UC is controlled to be the same as that of ZnO@UC. Absent of the pore spatial confinement effect, ZnO+UC shows large ZnO bulk at a micrometer size and serious aggregation (Figure 5.6), which causes the uneven distribution of ZnO and UC nanospheres. The crystal structure of ZnO+UC, which is identical to that of ZnO@UC, is shown in Figure 5.5a.

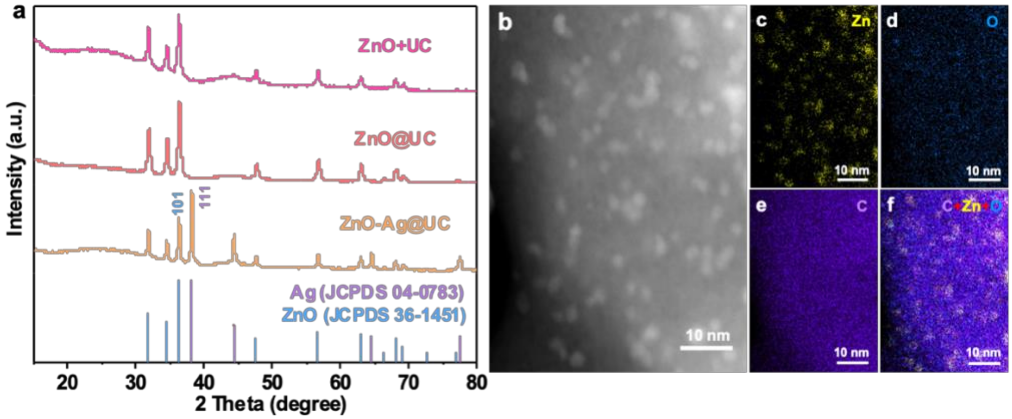

Figure 5.5 (a) XRD patterns of various samples. (b) HAADF-STEM image and (c-f) corresponding EDS elemental mapping of ZnO@UC.

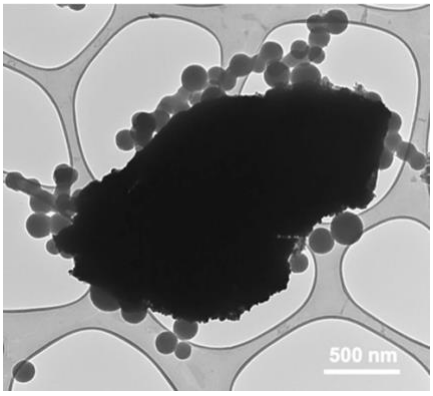

Figure 5.6 TEM image of ZnO+UC.

The well-developed pore texture of UC is demonstrated in Figure 5.7a, showing a typical type-I and type-II combined adsorption isotherm and a characteristic H4 hysteresis loop, both of which feature the hierarchical nature of micropores and small mesopores.[46] Remarkably, UC possesses an ultrahigh specific surface area of 4115 $m^2 g^{-1}$ and a large pore volume of 2.43 $cm^3 g^{-1}$, which guarantee good dispersion for the ZnO-Ag nanoparticles. The unprecedented surface area, arising from our innovative dual-pore-forming technique, surpasses the previous record of 4073 $m^2 g^{-1}$ for porous carbon materials reported by Bao's group.[251] As revealed by the pore size distribution plots (Figure 5.7b), UC shows two sets of prominent pore sizes involving a narrow diameter of 2 nm and a relatively large diameter of 3.1 nm. The latter exactly coincides with the size of ZnO-Ag nanoparticles impregnated within the pores, while the former could potently immobilize ZnO-Ag nanoparticles to preclude their detachment and restrict their growth to regulate the nanosize, demonstrating the "two ships in a bottle" design concept. Besides, the pore size distribution of ZnO-Ag@UC ranges from 1 to 7 nm, exactly corresponding to the nanoparticle sizes as revealed in Figure 5.4g. ZnO-Ag@UC inherits the

well-developed pore structure of UC, delivering an ultrahigh-surface-area (3615 m^2 g^{-1}) and a large pore volume (2.07 cm^3 g^{-1}), which is favorable for exposing a high density of active sites and guaranteeing fast mass transfer. As expected, ZnO@UC presents a similar surface area of 3821 m^2 g^{-1} and pore volume of 2.32 cm^3 g^{-1}. However, ZnO+UC possesses relatively poor pore texture, signifying uneven mechanical mixing could cause pore-blockage and hence diminish the porosity.

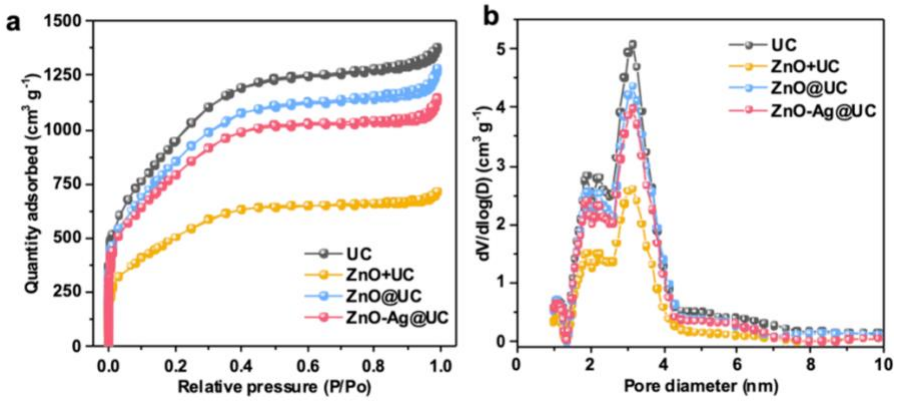

Figure 5.7 (a) N_2 adsorption-desorption isotherms and (b) pore size distribution of various samples.

Further insight into the chemical composition and valence states of ZnO-Ag@UC was obtained by XPS. In the Zn 2p spectra (Figure 5.8a), ZnO@UC displays two peaks of Zn $2p_{3/2}$ and $2p_{1/2}$, which confirm the oxidation state of Zn^{2+},[252] whereas for ZnO-Ag@UC, these two peaks shift to higher binding energy, implying a depletion of electron density around Zn atoms. In comparison to the O 1s spectra of ZnO@UC (Figure 5.8b), which show three peaks presenting the Zn-O, Zn-OH, and C=O bonds,[253] ZnO-Ag@UC spectra show the same three peaks except for a pronounced lower-energy shift of Zn-O and Zn-OH. Such a phenomenon is attributed to the covalent bonds between Zn and O, wherein electrons are transferred from Zn to O.[254] Additionally, the Ag 3d spectrum of ZnO-Ag@UCexhibits Ag $3d_{5/2}$ and Ag $3d_{3/2}$ peaks

at 368.7 and 374.7 eV (Figure 5.9), respectively, both of which have higher binding energy than those of Ag@UC and previously reported results for Ag,[255–257] indicative of the electron depletion of Ag atoms. These shifts are ascribed to the electron transfer effect within the Zn-Ag-O heterointerface.

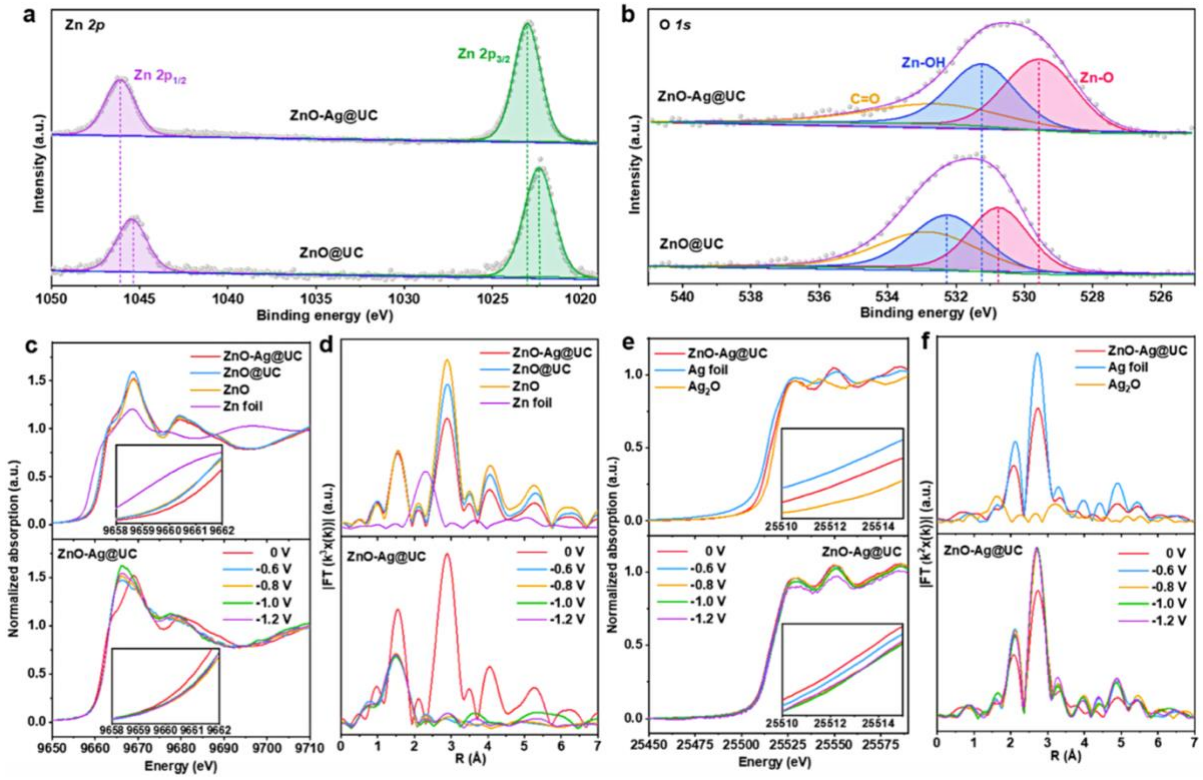

Figure 5.8 Chemical environment and electron density transfer analysis. XPS spectra of (a) Zn 2p and (b) O 1s for ZnO-Ag@UC and ZnO@UC. In situ (c) Zn *K*-edge XANES and (d) corresponding Fourier-transform k^3-weighted EXAFS spectra, (e) Ag *K*-edge XANES, and (f) corresponding Fourier-transform k^2-weighted EXAFS spectra for various samples at different applied potentials during CO_2RR.

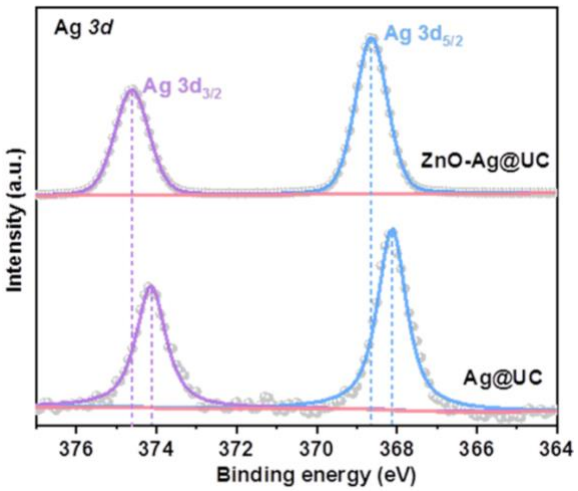

Figure 5.9 XPS spectra of Ag 3d for ZnO-Ag@UC and Ag@UC.

To unravel the electron density configuration and coordination environment of ZnO-Ag@UC during CO_2RR, we performed in situ XANES and EXAFS spectroscopy under operating conditions at various applied voltages. In the Zn K-edge XANES spectra (Figure 5.8c), Zn foil and ZnO were employed as references for metallic Zn^0 and Zn^{2+}, respectively. Surprisingly, ZnO-Ag@UC shows a higher oxidation state than Zn^{2+}. The existence of Ag triggers the electron transfer and rearranges the electron distribution, potentially allowing Zn atoms to release more electrons from the d orbital in addition to the two electrons in the s orbital. A similar result inferring a higher oxidation state for Zn was previously reported by Jena and Samanta.[258] Upon application of a potential from -0.6 to -1.2 V (vs. RHE), the Zn absorption edge of ZnO-Ag@UC positively shifts to even higher oxidation states, confirming enhanced electron density depletion around Zn atoms during CO_2RR. In the corresponding Fourier-transform k^3-weighted EXAFS spectra (Figure 5.8d), before the voltage was applied, ZnO-Ag@UC shows two prominent peaks corresponding to the first and second neighboring Zn atoms in the ZnO phase, where Zn is coordinated to 4 O atoms (Zn-O) with a bond length of 1.98 Å in the first shell while the second neighboring Zn is bounded by 12 Zn atoms (Zn-

Zn) with a bond length of 3.21 Å.[259,260] Compared to ZnO@UC, ZnO-Ag@UC displays a lower coordination number for the Zn-O bond derived from the effective coordination regulation from Ag. Especially, on application of a potential, the second peak for 12 Zn atoms almost disappears, while the first peak for Zn-O coordination shows a significantly increased Debye-Waller factor along with reduced coordination number and bond length, implying an intensified structural disorder in the Zn-O coordination with the possible formation of Zn-O-Ag coordination during CO_2RR.[261] The Ag near-edge position of ZnO-Ag@UC is between that of Ag foil and Ag_2O (Figure 5.8e), indicating that the Ag valence state is intermediate to Ag^0 and Ag^+, which probably arises from the electron donation from Ag to O. The electron transfer effects are more pronounced at the applied potentials where the Ag absorption-edge shifts toward higher energy. In the Ag EXAFS spectra (Figure 5.8f), ZnO-Ag@UC shows peaks consistent with Ag foil, but it displays a lower coordination number. The low-coordinated surface Ag atoms in ZnO-Ag@UC are conducive to reducing the activation energy of forming *COOH, potentially improving the CO production rate and selectivity.[262] In addition to the Ag-Ag bond appearing at 2.87 Å, both ZnO-Ag@UC and Ag foil show a weak peak at 2.23 Å corresponding to the Ag-O species that is different from the Ag-O bond in Ag_2O.[263,264] This observed oxygen species, which might originate from the bound interaction of Ag with O from ZnO and/or air,[255] has a longer Ag-O distance than the Ag-O bond length in Ag_2O. This phenomenon signifies the electron sharing between the Ag and O is smaller than that in the pure silver oxide.[255] Under CO_2RR conditions at applied potentials for ZnO-Ag@UC, the Ag-O bond displays a higher coordination number and increased bond length (Figure 5.8f), whereas the Zn-O bond weakens the coordination and reduces the bond length (Figure 5.8d), which suggests the possible shift of partial O from ZnO toward Ag to spark the electron

delocalization within the Zn-Ag-O heterointerface. Additionally, the Ag-O coordination which shapes under the electrocatalytic conditions, probably resulting from the bonding of Ag and CO_2RR intermediates, could help to activate CO_2 on the surface at the initial step.[265]

Taken together, the above evidence confirms the electron density reconfiguration among Zn, Ag, and O atoms. Specifically, Zn and Ag atoms delocalize charge by releasing electrons to the O atoms, which is consistent with the theoretical calculations. These results justify the correlation between the theoretical models and experimental structures.

The CO_2 electroreduction performances were investigated in the CO_2-saturated 0.5 M $KHCO_3$ electrolyte with an H-type cell. To demonstrate the crucial role of the Zn-Ag-O heterointerface, another control sample, Ag@UC, was prepared by the same synthesis route with ZnO-Ag@UC except that only silver nitrate was added as precursor. The Ag content in Ag@UC is 15.8 wt% determined by ICP-OES. Ag@UC shows the pure metallic Ag phase as confirmed by XRD (Figure 5.10a). Figure 5.10b-e exhibit the morphology of Ag@UC, where ultrafine Ag nanoparticles are implanted inside the carbon pores and meanwhile maintain a uniform distribution over the UC matrix. This also demonstrates the proposed "ship in a bottle" design.

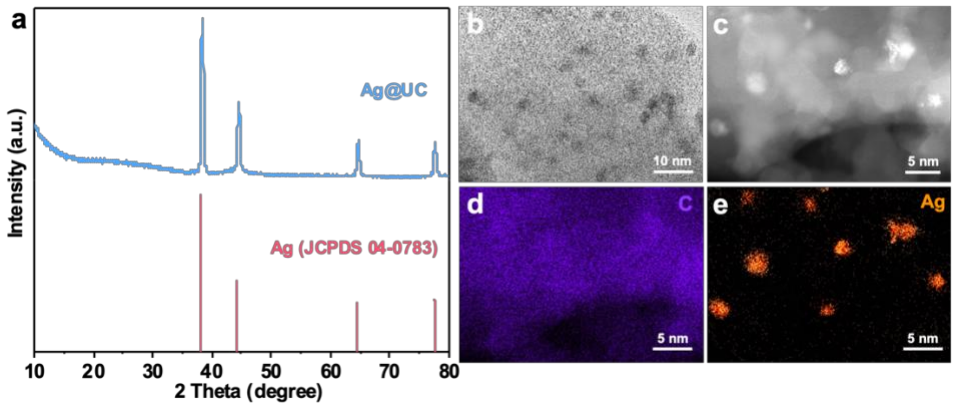

Figure 5.10 (a) XRD pattern of Ag@UC. (b) TEM image, (c) HAADF-STEM image and (d,e) corresponding EDS elemental mapping of Ag@UC.

LSV curves demonstrate ZnO-Ag@UC to have the lowest onset potential and highest current densities among various samples (Figure 5.11a). Figure 5.12a revealed a dramatic current increase for ZnO-Ag@UC in CO_2-saturated electrolyte compared to the Ar-saturated case, demonstrating that CO_2RR occurs readily on the ZnO-Ag@UC catalyst. CO, formate, and H_2 were the only products detected in the production distribution of ZnO-Ag@UC (Figure 5.11b). ZnO-Ag@UC reaches a remarkable CO FE of 94.1 ± 4.0% at a low potential of -0.93 V, which outperforms the vast majority of reported Zn-based catalysts (Table 5.1). At -0.93 V, ZnO@UC shows a relatively lower CO FE and more competing production of formate and H_2 than ZnO-Ag@UC (Figure 5.12b), because of the absence of electron density reconfiguration manipulated by Ag. In addition, ZnO-Ag@UC realizes an extremely low H_2 yield of 4.1% at -0.93 V, demonstrating its excellent capability of suppressing HER that outperforms recently reported Zn-based catalysts (Table 5.1). The energy conversion efficiency of ZnO-Ag@UC is projected to reach 60.9% (details are provided in the Experimental Section), surpassing previously reported Zn-based catalysts (Table 5.1) and satisfying the basic requirement for electrosynthesis to compete with fossil-fuel-derived feedstocks.[218] It is important to note that ZnO-Ag@UC, which delivers strong electron transfer effects within the Zn-Ag-O heterointerface, favors CO production over formate, as confirmed by the low formate FE at all potentials, which coincides with the theoretical predictions. Moreover, to demonstrate the role of UC matrix, we investigated two additional control samples, ZnO-Ag and ZnO-Ag+UC. The former was prepared by mechanically mixing zinc nitrate and silver nitrate solids followed by the same pyrolysis process. The latter was synthesized by mechanically mixing zinc nitrate,

silver nitrate, and UC followed by the same pyrolysis process, where the ZnO and Ag content of ZnO-Ag+UC is controlled to be the same as that of ZnO-Ag@UC.

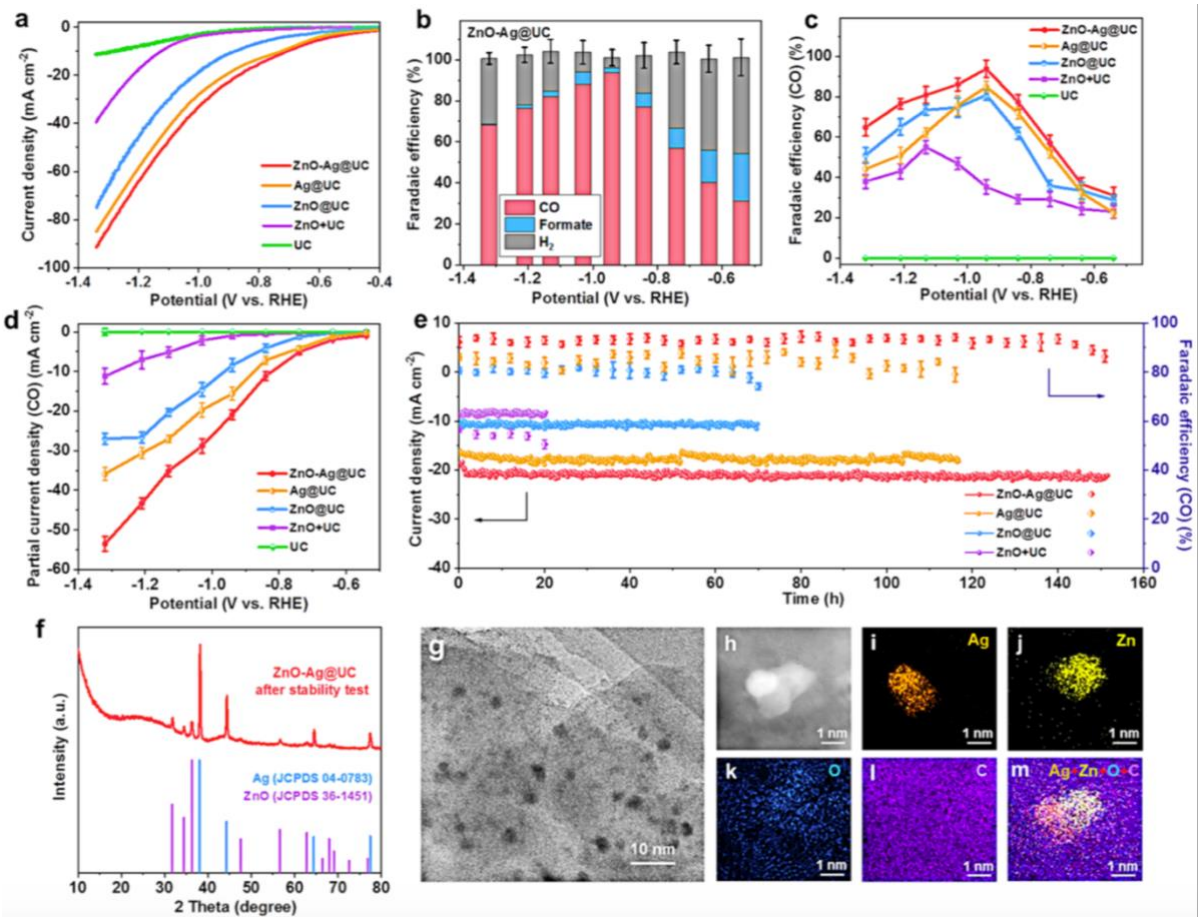

Figure 5.11 CO_2RR performances and post-test characterizations. (a) LSV curves for various samples; (b) FE toward CO, formate, and H_2 for ZnO-Ag@UC; (c) FE of CO, (d) CO partial current density, and (e) stability testing at -0.93 V for various samples. Ex situ (f) XRD pattern, (g) TEM image, (h) HAADF-STEM image, and (i-m) corresponding EDS elemental mapping of ZnO-Ag@UC after a stability test.

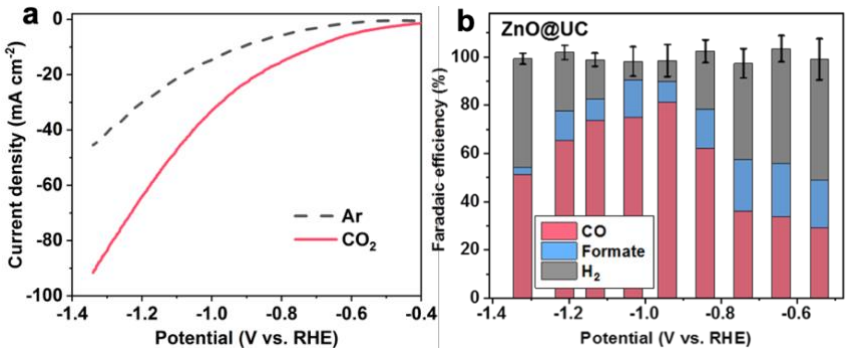

Figure 5.12 (a) LSV curves of ZnO-Ag@UC in Ar- and CO_2-saturated 0.5 M $KHCO_3$ electrolyte. (b) FE toward CO, formate and H_2 for ZnO@UC.

In a comparison of various catalysts toward CO formation (Figure 5.11c and Figure 5.13a), ZnO+UC has a very low FE of 52.4 ± 2.8%, while ZnO@UC and Ag@UC show improved FE of 79.3 ± 2.5% and 84.2 ± 3.0%, respectively. Combining the elaborate structure and Zn-Ag-O interplay, ZnO-Ag@UC obtains an optimum selectivity for CO (94.1 ± 4.0%). In contrast, devoid of spatial confinement by UC and a tailored "two ships in a bottle" structure, ZnO-Ag+UC cannot control the sizes of ZnO and Ag phases with a low active surface-to-volume ratio, and more importantly, it cannot guarantee the uniform and twinned distribution of ZnO and Ag, and thus cannot effectively construct abundant Zn-Ag-O heterointerfaces. The merits of UC, including an ultrahigh surface area and interconnected carbon framework for active sites dispersion, cannot be reflected in ZnO-Ag+UC. As a result, ZnO-Ag+UC presents much lower FE (CO) than ZnO-Ag@UC (Figure 5.13a). As exhibited in Figure 5.11d, the highest CO partial current densities are realized by ZnO-Ag@UC, which also demonstrates superiority over previously reported catalysts (Table 5.1).

Table 5.1 Comparison of CO_2RR performance of ZnO-Ag@UC with recently reported Zn-based catalysts using an H-type cell

Catalyst	Operating potential (V vs. RHE)	Faradaic efficiency (CO) (%)	Faradaic efficiency (H_2) (%)	Energy efficiency (%)	Current density (CO) (mA cm^{-2})	Reference
ZnO-Ag@UC	**-0.93**	**98.1**	**4.1**	**60.9**	**22.3**	**This work**
R-ZnO/rGO	-1.0	94.3	N/A	56.7	7.2	[266]
Zn P-NS	-1.0	90.0	N/A	54.1	7.4	[267]
LiET-Zn	-1.17	91.1	N/A	50.9	5.3	[268]
h-Zn	-0.95	85.4	8.0	52.5	9.5	[269]
Vo-rich ZnO	-1.1	83.0	18.0	47.7	16.1	[240]
Zn dendrite	-1.1	79.0	N/A	45.4	13.4	[225]
9.4%-Ag-alloyed Zn	-1.0	97.0	7.0	58.3	16.8	[270]
ZIF-A-LD/CB	-1.0	75.0	N/A	45.1	3.2	[271]
PD-Zn/Ag	-1.2	74.0	14.4	40.8	9.7	[272]
MZnNSs	-1.13	86.0	12.5	48.8	5.2	[273]
$Zn_{94}Cu_6$	-0.95	90.0	10.0	52.9	7.1	[274]
RE-Zn-CO_2	-1.0	77.6	N/A	46.6	8.4	[275]

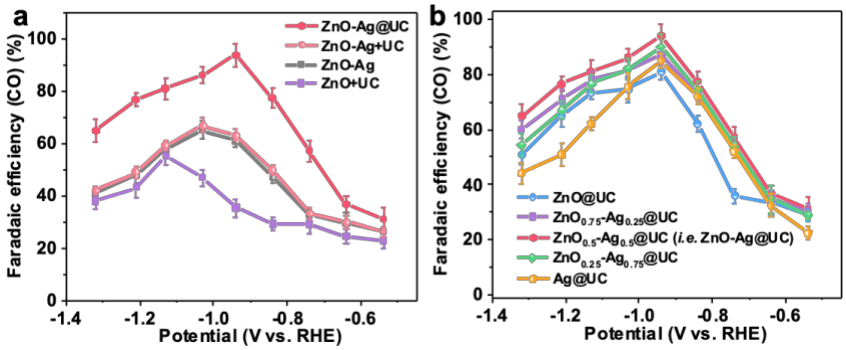

Figure 5.13 FE for CO of (a) various control samples for comparison and (b) ZnO-Ag-based samples with various ratios.

To further investigate the effect of bimetallic ratios on CO_2RR performance for CO production, we prepared catalysts with various ZnO and Ag ratios, including $ZnO_{0.75}$-$Ag_{0.25}$@UC and $ZnO_{0.25}$-$Ag_{0.75}$@UC. ZnO-Ag@UC, which has identical contents of ZnO and Ag, here is denoted as $ZnO_{0.5}$-$Ag_{0.5}$@UC for explicit comparison. As shown in Figure 5.13b, with the Ag introduction to ZnO, the FE of CO is significantly enhanced, with $ZnO_{0.5}$-$Ag_{0.5}$@UC reaching the optimum selectivity for CO. This could be ascribed to the boosted electron transfer effects with the increased heterointerfaces established. $ZnO_{0.5}$-$Ag_{0.5}$@UC, possessing identical ZnO and Ag content, probably presents abundant and desirable interfacial sites contributing to improved catalytic activity.[276] However, $ZnO_{0.25}$-$Ag_{0.75}$@UC exhibits slightly declined FE of CO compared to $ZnO_{0.5}$-$Ag_{0.5}$@UC, which could be due to the reduced interfacial sites with more Ag added.[276]

In terms of the catalytic mechanism, at the interface, ZnO modulates the electron configuration of the interfacial Ag atom with the concomitant electron density reconfiguration, while the interfacial Ag behaves as the main active site by binding with CO_2 species; it should be noted that it is the Ag site in contact with ZnO at the interface that adsorbs the carbon source as the active center instead of other sites in the Ag particle. Therefore, ZnO and Ag are equally critical in the catalyst with the construction of the Zn-Ag-O heterointerfaces, prominently improving CO_2RR activity and selectivity for CO as compared to that of ZnO only and Ag only.

To demonstrate the stability of the developed catalysts, a major concern for CO_2RR, we employed a strict standard to investigate the catalyst stability. The stability measurements were stopped when the FE decreased by more than 5% from the initial state, after which the catalysts were considered to deliver not as good CO_2RR selectivity as their initial states. It is worthy to note that, under this rigorous standard, ZnO-Ag@UC exhibits remarkable long-term stability over 150 h at the potential of -0.93 V (Figure 5.11e), which far exceeds other recently reported results (Table 5.2). ZnO-Ag@UC maintains a steady current density of approximately 21.5 mA cm^{-2} with negligible degradation, while the CO FE stays above 90%, demonstrating that ZnO-Ag@UC is highly stable during CO_2RR. Besides, Ag@UC and ZnO@UC present better stability than ZnO+UC, revealing the crucial role of the "ship in a bottle" structure on stability improvement. After a long-term stability test, ZnO-Ag@UC maintains the ZnO and Ag phases, as confirmed by ex situ XRD analysis (Figure 5.11f). As disclosed by ex situ TEM and HAADF-STEM images (Figure 5.11g and h), ZnO-Ag nanoparticles are still confined well within the UC pores at an original size of 3.1 nm without obvious agglomeration or detachment. The intact Ag and ZnO phases remain twinned to constitute one nanoparticle (Figure 5.11i-m). By contrast, ZnO+UC shows a much larger micrometer-sized bulk after stability testing because of the absence of a nanopore spatial confinement effect (Figure 5.14), resulting in a limited active surface-to-volume ratio. Besides, the serious agglomeration and fragmentation occur, causing inevitable loss of catalytic activity and stability. Therefore, with the well-tailored "two ships in a bottle" structure and effective electron delocalization within the Zn-Ag-O heterointerface, ZnO-Ag@UC demonstrates superior electrochemical performances and long-term durability, revealing high promise for a practical CO_2RR system.

Table 5.2 Stability comparison of ZnO-Ag@UC with recently reported CO_2RR catalysts for CO production

Catalyst	Stability (h)	Reference
ZnO-Ag@UC	**150**	**This work**
R-ZnO/rGO	21	[266]
9.4%-Ag-alloyed Zn	11	[270]
CdS needles	24	[277]
$Sn_{2.7}Cu$	40	[278]
Co@PC/C	20	[279]
ZnCoNC	30	[280]
L70-Ag-NCs	18	[246]
CoPc-CN/CNT	10	[281]
Ag@Al-PMOF	12	[282]
Ni-NCB	24	[283]
Co-N_5/HNPCSs	10	[284]
Au needles	8	[285]
Au/PE	35	[286]
CoPc/CNT	10	[287]
PcCu-O_8-Zn/CNT	11	[224]

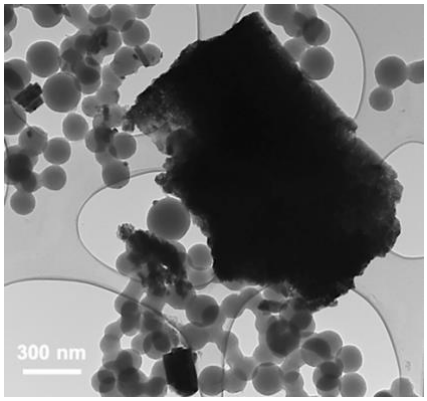

Figure 5.14 Ex situ TEM image of ZnO+UC after stability test.

5.4 Conclusions

Guided by theoretical calculations, we developed a “two ships in a bottle” design for ternary Zn-Ag-O catalysts comprising ultrafine twinned ZnO and Ag nanoparticles impregnated inside the nanopores of an ultrahigh-surface-area carbon matrix for selective and durable CO_2 reduction to CO. Thermodynamic DFT analyses and in situ XAS studies disclose that the electron delocalization from Zn and Ag to O not only improves the intrinsic activity for generating CO by stabilizing *COOH but also increases the energy barrier for forming HCOO* and *H to suppress formate and H_2 and promote CO selectivity. Moreover, the well-tailored “two ships in a bottle” structure not only controls the nanoparticle size and guarantees an ultrahigh surface-to-volume ratio to provide plentiful active sites, significantly promoting CO_2RR activity, but also potently prohibits nanoparticles from agglomeration and detachment during both synthesis and CO_2RR, greatly improving stability. A win-win between exposure of active sites with high selectivity and stability is thus achieved. Consequently, the developed catalyst exhibits high energy efficiency of 60.9% for CO production with an excellent selectivity up to 98.1% and long-term durability of over 150 h. This work presents a new

strategic direction to design high-performance catalyst, enabling electrochemical processes more sustainable for practical application.

Chapter 6 Conclusions and Future Work

6.1 Conclusions

In this thesis, approaches to rationally engineering porous carbon-based metal nanocomposites are successfully implemented to develop high-performance electrocatalysts. In Chapter 3, a unique "ship in a bottle" concept is proposed and successfully implemented to engineer bifunctional oxygen electrocatalysts for ORR and OER. The catalyst consisting of CoS_2 nanoparticles impregnated inside the defective carbon nanopores with S-doped pore wall is prepared via precursor impregnation, hydrolysis and subsequent thermal sulfurization. This methodology realizes the combination of excellent catalytic kinetics and electrical conductivity provided by the interconnecting porous carbon framework acting as a nanoreactor, which effectively restricts the nucleation (i.e., overgrowth) and agglomeration of nanoparticles during catalysis. Therefore, the elaborately engineered catalyst harvesting the synergistic effect between defect-rich interfaces (i.e., S-doped pores) and effective catalytic active sites (CoS_2 and C−S−C bonding) guarantees excellent bifunctional catalytic activity and durability for both ORR and OER. When the as-prepared catalyst is integrated into the air cathode, the assembled Zn−air battery exhibits low charge and discharge overpotential (i.e., high energy efficiency), large peak power density, and exceptionally stable cyclability of over 340 h at a very high current density of 25 mA cm^{-2}, outperforming noble-metal benchmarks and other recently reported results.

Based on the study in Chapter 3, Chapter 4 further takes advantage of the "ship in a bottle" strategy to manipulate metal nanoclusters crystallinity and introduce defect engineering. The engineered ultrafine amorphous tantalum oxide nanoclusters with oxygen vacancies (Ta_2O_{5-x}) implanted inside a microporous carbon matrix are, for the first time, employed as a new electrocatalyst for polysulfide catalysis and retention. Carbon nanopores restrict the nucleation of Ta_2O_{5-x} nanoseeds to shape the incomplete unit cell in an amorphous structure with enlarged active surfaces, which reduces the Ta–O bond length and provides strong chemical affinity for LPS. The oxygen vacancies further tune the Ta–O local coordination environment and electron band structure of Ta_2O_{5-x} to improve the intrinsic electrical conductivity and function as catalytic centers. The engineered 3D conductive nanoreactor loaded with Ta_2O_{5-x} nanoclusters efficiently inhibits LPS shuttling and promotes LPS conversion with fast redox kinetics. Meanwhile, the sulfur agglomeration and volume expansion are well suppressed in the pitaya-like structure. These featuring superiorities endow the developed sulfur electrode with outstanding rate capability and cyclability even at practically relevant sulfur loading and electrolyte content.

Chapter 5 further optimizes the monometallic design to a bimetallic design by a "two ships in a bottle" strategy to meet higher electrocatalyst requirements. The engineered bimetallic Zn-Ag-O catalysts, where ZnO and Ag phases are twinned to constitute an individual ultrafine nanoparticle impregnated inside nanopores of an ultrahigh-surface-area carbon matrix, enable selective and durable CO_2 reduction to CO. Thermodynamic DFT analyses and in situ XAS studies disclose that the electron delocalization from Zn and Ag to O not only improves the intrinsic activity for generating CO by stabilizing *COOH but also increases the energy barrier for forming HCOO* and *H to suppress formate and H_2 and promote CO selectivity. Moreover,

the well-tailored “two ships in a bottle” structure not only controls the nanoparticle size and guarantees an ultrahigh surface-to-volume ratio to provide plentiful active sites, significantly promoting CO_2RR activity, but also potently prohibits nanoparticles from agglomeration and detachment during both synthesis and CO_2RR, greatly improving stability. A win−win between exposure of high-density active sites with high selectivity and stability is thus achieved. Consequently, the developed catalyst exhibits high energy efficiency of 60.9% for CO production with an excellent selectivity up to 98.1% and long-term durability of over 150 h.

In summary, in this thesis, the developed strategy of impregnating UMNPs into nanopores of high-surface-area porous carbon matrices presents multiple merits to fulfill the design principles of an ideal catalyst: i) the nucleation and growth of nanoclusters/nanoparticles is restricted by the 3D nanoreator to control their size and offer a high surface-to-volume ratio to expose abundant active sites, significantly promoting catalytic activity; ii) the metal-in-pore structure potently immobilizes UMNPs and inhibits their agglomeration and detachment during both synthesis and electrocatalytic reactions, greatly prolonging catalyst durability; iii) the interconnected porous conductive network facilitates mass transport and electron mobility throughout the framework, expediting catalytic kinetics; iv) multiple modification approaches, such as heteroatom doping, defect engineering, crystallinity manipulation, and electron configuration modulation, can be incorporated to improve catalyst intrinsic activity and selectivity. This strategy is successfully implemented in promising electrochemical transformation systems including oxygen, sulfur, and CO_2 electrocatalysis, providing a new route to efficiently convert abundant resources such as H_2O, S, and CO_2 to electricity to march toward a sustainable energy future.

6.2 Recommended Future Work

Based on the studies conducted in this thesis, the following recommendations are proposed for future work.

(1) Porous support design. Aside from porous carbon materials studied in this thesis, a wide range of porous materials, such as MOFs, zeolite, silica, could be explored as the tailored support for immobilizing UMNPs. To enable the efficient impregnation of UMNPs into the pores, the controllable optimization of pore textures (e.g., surface area, pore size, and pore volume) and surface properties is crucial, which can tune the interaction between metal precursor molecules and pore surface of the supports. By introducing various functional groups into support surface, the inherent electronic and steric properties of the decorated groups may deliberately balance the interaction between the resulting UMNPs and the supports, and finally endow the UMNPs with better binding, higher stabilization, and unique physicochemical and catalytic properties. In addition, the facile and precise synthesis routes to tailored porous supports should be developed in the future work.

(2) Improved impregnation techniques. Ordinary impregnation with metal precursors results, in many cases, in poly-dispersed MNPs both within the pores and on the outer surface of the support, probably as a result of the partial deposition or adsorption of the precursors on the outer surface. Therefore, efficient approaches to introducing metal precursors into the interior pores of the matrices should be developed. The use of a sacrificial template and combination of multiple impregnation techniques provide feasible strategies.

(3) Active site engineering. To further enhance the catalytic activity and selectivity for satisfying higher catalytic requirements, the exploration of multi-metal components

impregnated into porous supports is highly promising. Meanwhile, the interplay between various metal phases through the modulation of electron configuration and distribution should be understood by employing theoretical calculations coupled with advanced material characterization techniques. Besides, how to achieve a win−win between high density of active sites and uniform distribution is a critical consideration. In addition, further downsizing the metal particles to atomic level provides an effective way to significantly enhance the metal utilization efficiency and reduce the cost of noble metal catalysts. Rationally engineering single-atom or diatomic sites immobilized into porous supports offers a highly promising research direction. Last but not least, metal components and supports are not independent systems; efforts on exploring their synergistic effect will shed light on novel and efficient design strategies toward high-performance catalysts.

Copyright Permissions

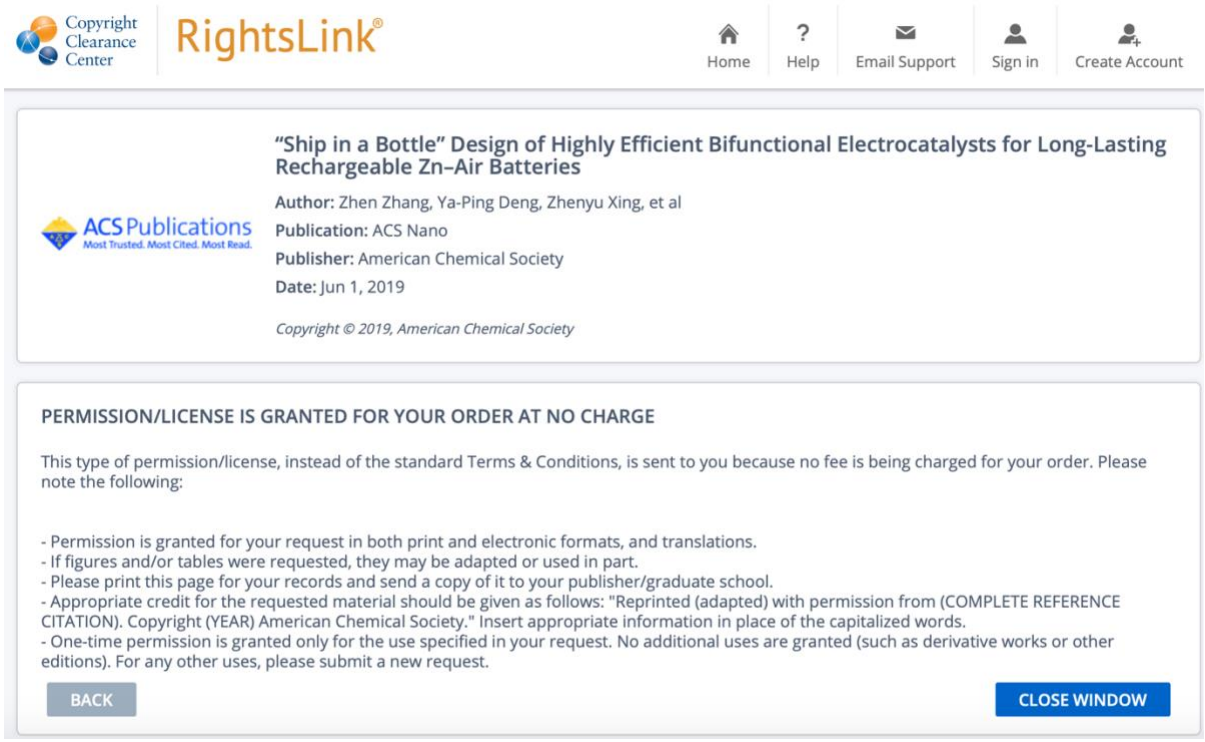

Copyright Clearance Center | RightsLink®

Home | Help | Email Support | Sign in | Create Account

ACS Publications
Most Trusted. Most Cited. Most Read.

"Ship in a Bottle" Design of Highly Efficient Bifunctional Electrocatalysts for Long-Lasting Rechargeable Zn–Air Batteries

Author: Zhen Zhang, Ya-Ping Deng, Zhenyu Xing, et al
Publication: ACS Nano
Publisher: American Chemical Society
Date: Jun 1, 2019

Copyright © 2019, American Chemical Society

PERMISSION/LICENSE IS GRANTED FOR YOUR ORDER AT NO CHARGE

This type of permission/license, instead of the standard Terms & Conditions, is sent to you because no fee is being charged for your order. Please note the following:

- Permission is granted for your request in both print and electronic formats, and translations.
- If figures and/or tables were requested, they may be adapted or used in part.
- Please print this page for your records and send a copy of it to your publisher/graduate school.
- Appropriate credit for the requested material should be given as follows: "Reprinted (adapted) with permission from (COMPLETE REFERENCE CITATION). Copyright (YEAR) American Chemical Society." Insert appropriate information in place of the capitalized words.
- One-time permission is granted only for the use specified in your request. No additional uses are granted (such as derivative works or other editions). For any other uses, please submit a new request.

BACK | CLOSE WINDOW

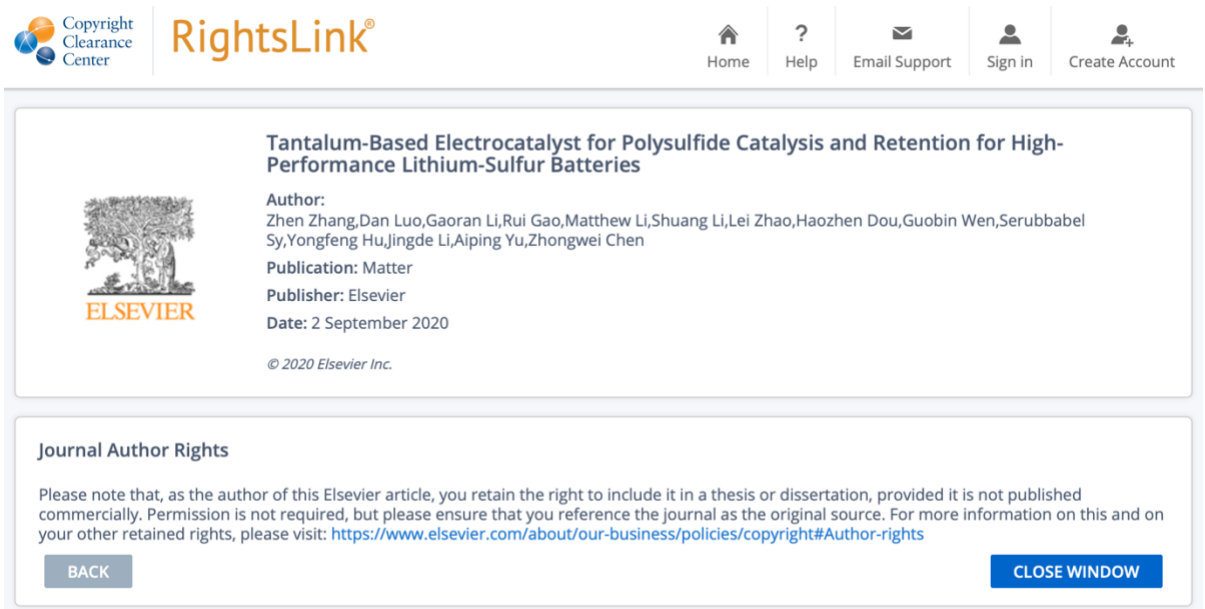

Copyright Clearance Center | RightsLink®

Home | Help | Email Support | Sign in | Create Account

ELSEVIER

Tantalum-Based Electrocatalyst for Polysulfide Catalysis and Retention for High-Performance Lithium-Sulfur Batteries

Author:
Zhen Zhang,Dan Luo,Gaoran Li,Rui Gao,Matthew Li,Shuang Li,Lei Zhao,Haozhen Dou,Guobin Wen,Serubbabel Sy,Yongfeng Hu,Jingde Li,Aiping Yu,Zhongwei Chen
Publication: Matter
Publisher: Elsevier
Date: 2 September 2020

© 2020 Elsevier Inc.

Journal Author Rights

Please note that, as the author of this Elsevier article, you retain the right to include it in a thesis or dissertation, provided it is not published commercially. Permission is not required, but please ensure that you reference the journal as the original source. For more information on this and on your other retained rights, please visit: https://www.elsevier.com/about/our-business/policies/copyright#Author-rights

BACK | CLOSE WINDOW

References

1 Y. Xu, V. Ramanathan and D. G. Victor, *Nature*, 2018, **564**, 30–32.

2 IEA, *World Energy Outlook 2020*, IEA, Paris, 2020.

3 L. Capuano, *International Energy Outlook 2020 (IEO2020)*, U.S. Energy Information Administration (EIA), Washington, DC, 2020.

4 Z. W. Seh, J. Kibsgaard, C. F. Dickens, I. Chorkendorff, J. K. Nørskov and T. F. Jaramillo, *Science*, 2017, **355**, eaad4998.

5 Z. Zhang, Y.-P. Deng, Z. Xing, D. Luo, S. Sy, Z. P. Cano, G. Liu, Y. Jiang and Z. Chen, *ACS Nano*, 2019, **13**, 7062–7072.

6 J. Fu, R. Liang, G. Liu, A. Yu, Z. Bai, L. Yang and Z. Chen, *Adv. Mater.*, 2019, **31**, 1805230.

7 Z. Zhang, D. Luo, G. Li, R. Gao, M. Li, S. Li, L. Zhao, H. Dou, G. Wen, S. Sy, Y. Hu, J. Li, A. Yu and Z. Chen, *Matter*, 2020, **3**, 920–934.

8 Y. Song, W. Cai, L. Kong, J. Cai, Q. Zhang and J. Sun, *Adv. Energy Mater.*, 2020, **10**, 1901075.

9 Z. Zhang, G. Wen, D. Luo, B. Ren, Y. Zhu, R. Gao, H. Dou, G. Sun, M. Feng, Z. Bai, A. Yu and Z. Chen, *J. Am. Chem. Soc.*, 2021, **143**, 6855–6864.

10 F. Pan and Y. Yang, *Energy Environ. Sci.*, 2020, **13**, 2275–2309.

11 G. Li, S. Wang, Y. Zhang, M. Li, Z. Chen and J. Lu, *Adv. Mater.*, 2018, **30**, 1705590.

12 D. L. Fedlheim and C. A. Foss, *Metal nanoparticles: synthesis, characterization, and applications*, CRC press, 2001.

13 Q.-L. Zhu and Q. Xu, *Chem*, 2016, **1**, 220–245.

14 R. J. White, R. Luque, V. L. Budarin, J. H. Clark and D. J. Macquarrie, *Chem. Soc. Rev.*, 2009, **38**, 481–494.

15 Z. Zhang, Z. P. Cano, D. Luo, H. Dou, A. Yu and Z. Chen, *J. Mater. Chem. A*, 2019, **7**, 20985–21003.

16 C. Hu, Y. Lin, J. W. Connell, H. Cheng, Y. Gogotsi, M. Titirici and L. Dai, *Adv. Mater.*, 2019, **31**, 1806128.

17 L. Dai, Y. Xue, L. Qu, H.-J. Choi and J.-B. Baek, *Chem. Rev.*, 2015, **115**, 4823–4892.

18 H. Sun, J. Zhu, D. Baumann, L. Peng, Y. Xu, I. Shakir, Y. Huang and X. Duan, *Nat. Rev. Mater.*, 2019, **4**, 45–60.

19 Q. Wu, L. Yang, X. Wang and Z. Hu, *Adv. Mater.*, 2019, 1904177.

20 S. Navalon, A. Dhakshinamoorthy, M. Alvaro and H. Garcia, *Coord. Chem. Rev.*, 2016, **312**, 99–148.

21 J. Lu, S. Yin and P. K. Shen, *Electrochem. Energy Rev.*, 2019, **2**, 105–127.

22 D. Higgins, M. A. Hoque, M. H. Seo, R. Wang, F. Hassan, J.-Y. Choi, M. Pritzker, A. Yu, J. Zhang and Z. Chen, *Adv. Funct. Mater.*, 2014, **24**, 4325–4336.

23 J. Wang, H. Wu, D. Gao, S. Miao, G. Wang and X. Bao, *Nano Energy*, 2015, **13**, 387–396.

24 B. Petrova, T. Budinova, N. Petrov, M. F. Yardim, E. Ekinci and M. Razvigorova, *Carbon*, 2005, **43**, 261–267.

25 E. Rodríguez and R. García, *Energy Fuels*, 2012, **26**, 3703–3710.

26 X. Shao, Z. Feng, R. Xue, C. Ma, W. Wang, X. Peng and D. Cao, *AIChE J.*, 2011, **57**, 3042–3051.

27 F. Rodríguez-reinoso, *Carbon*, 1998, **36**, 159–175.

28 R. J. White, V. Budarin, R. Luque, J. H. Clark and D. J. Macquarrie, *Chem Soc Rev*, 2009, **38**, 3401–3418.

29 D. Li, T. Ma, R. Zhang, Y. Tian and Y. Qiao, *Fuel*, 2015, **139**, 68–70.

30 L. Guo, J. Yang, G. Hu, X. Hu, L. Wang, Y. Dong, H. DaCosta and M. Fan, *ACS Sustain. Chem. Eng.*, 2016, **4**, 2806–2813.

31 M. Sevilla, C. Falco, M.-M. Titirici and A. B. Fuertes, *RSC Adv*, 2012, **2**, 12792–12797.

32 C. Falco, N. Baccile and M.-M. Titirici, *Green Chem.*, 2011, **13**, 3273.

33 R. Wang, P. Wang, X. Yan, J. Lang, C. Peng and Q. Xue, *ACS Appl. Mater. Interfaces*, 2012, **4**, 5800–5806.

34 A. E. Pütün, N. Özbay, E. P. Önal and E. Pütün, *Fuel Process. Technol.*, 2005, **86**, 1207–1219.

35 O. Ioannidou and A. Zabaniotou, *Renew. Sustain. Energy Rev.*, 2007, **11**, 1966–2005.

36 M. Sevilla and R. Mokaya, *Energy Env. Sci*, 2014, **7**, 1250–1280.

37 C. O. Ania and E. Raymundo-Piñero, in *Nanoporous Materials for Gas Storage*, eds. K. Kaneko and F. Rodríguez-Reinoso, Springer Singapore, Singapore, 2019, pp. 91–135.

38 M. G. Plaza, A. S. González, J. J. Pis, F. Rubiera and C. Pevida, *Appl. Energy*, 2014, **114**, 551–562.

39 A. Baçaoui, A. Yaacoubi, A. Dahbi, C. Bennouna, R. Phan Tan Luu, F. J. Maldonado-Hodar, J. Rivera-Utrilla and C. Moreno-Castilla, *Carbon*, 2001, **39**, 425–432.

40 J. Wang and S. Kaskel, *J. Mater. Chem.*, 2012, **22**, 23710.

41 T.-H. Liou, *Chem. Eng. J.*, 2010, **158**, 129–142.

42 J. Hayashi, T. Horikawa, I. Takeda, K. Muroyama and F. Nasir Ani, *Carbon*, 2002, **40**, 2381–2386.

43 M. A. Lillo-Rodenas, D. Cazorla-Amoros and A. Linares-Solano, *Carbon*, 2003, 9.

44 J. Romanos, M. Beckner, T. Rash, L. Firlej, B. Kuchta, P. Yu, G. Suppes, C. Wexler and P. Pfeifer, *Nanotechnology*, 2012, **23**, 015401.

45 J. Serafin, U. Narkiewicz, A. W. Morawski, R. J. Wróbel and B. Michalkiewicz, *J. CO2 Util.*, 2017, **18**, 73–79.

46 Z. Zhang, D. Luo, G. Lui, G. Li, G. Jiang, Z. P. Cano, Y.-P. Deng, X. Du, S. Yin, Y. Chen, M. Zhang, Z. Yan and Z. Chen, *Carbon*, 2019, **143**, 531–541.

47 Diana. P. Vargas, L. Giraldo and J. C. Moreno-Piraján, *J. Anal. Appl. Pyrolysis*, 2012, **96**, 146–152.

48 B. Grzyb, C. Hildenbrand, S. Berthon-Fabry, D. Bégin, N. Job, A. Rigacci and P. Achard, *Carbon*, 2010, **48**, 2297–2307.

49 R. J. White, V. Budarin, R. Luque, J. H. Clark and D. J. Macquarrie, *Chem. Soc. Rev.*, 2009, **38**, 3401.

50 C. Robertson and R. Mokaya, *Microporous Mesoporous Mater.*, 2013, **179**, 151–156.

51 A. E. Danks, S. R. Hall and Z. Schnepp, *Mater Horiz*, 2016, **3**, 91–112.

52 A. M. ElKhatat and S. A. Al-Muhtaseb, *Adv. Mater.*, 2011, **23**, 2887–2903.

53 B. Hu, S.-H. Yu, K. Wang, L. Liu and X.-W. Xu, *Dalton Trans.*, 2008, 5414–5423.

54 R. Demir-Cakan, N. Baccile, M. Antonietti and M.-M. Titirici, *Chem. Mater.*, 2009, **21**, 484–490.

55 M. Sevilla and A. B. Fuertes, *Chem. – Eur. J.*, 2009, **15**, 4195–4203.

56 Y. Li, D. Li, Y. Rao, X. Zhao and M. Wu, *Carbon*, 2016, **105**, 454–462.

57 M. Sevilla and A. B. Fuertes, *Carbon*, 2009, **47**, 2281–2289.

58 M.-M. Titirici, Robin. J. White, C. Falco and M. Sevilla, *Energy Environ. Sci.*, 2012, **5**, 6796.

59 M. Sevilla and A. B. Fuertes, *Energy Environ. Sci.*, 2011, **4**, 1765.

60 Z. Liu, Z. Zhang, Z. Jia, L. Zhao, T. Zhang, W. Xing, S. Komarneni, F. Subhan and Z. Yan, *Chem. Eng. J.*, 2018, **337**, 290–299.

61 T.-Y. Ma, L. Liu and Z.-Y. Yuan, *Chem Soc Rev*, 2013, **42**, 3977–4003.

62 T. Kyotani, N. Sonobe and A. Tomita, *Nature*, 1988, **331**, 331–333.

63 T. Kyotani, T. Nagai, S. Inoue and A. Tomita, *Chem. Mater.*, 1997, **9**, 609–615.

64 Q. Li, J. Yang, D. Feng, Z. Wu, Q. Wu, S. S. Park, C.-S. Ha and D. Zhao, *Nano Res.*, 2010, **3**, 632–642.

65 X. He, H. Zhang, H. Zhang, X. Li, N. Xiao and J. Qiu, *J. Mater. Chem. A*, 2014, **2**, 19633–19640.

66 K. P. Gierszal and M. Jaroniec, *J. Am. Chem. Soc.*, 2006, **128**, 10026–10027.

67 Y. Liang, F. Liang, D. Wu, Z. Li, F. Xu and R. Fu, *Phys. Chem. Chem. Phys.*, 2011, **13**, 8852.

68 J. Liu, N. P. Wickramaratne, S. Z. Qiao and M. Jaroniec, *Nat. Mater.*, 2015, **14**, 763–774.

69 T. N. Hoheisel, S. Schrettl, R. Szilluweit and H. Frauenrath, *Angew. Chem. Int. Ed.*, 2010, **49**, 6496–6515.

70 C. Liang, K. Hong, G. A. Guiochon, J. W. Mays and S. Dai, *Angew. Chem. Int. Ed.*, 2004, **43**, 5785–5789.

71 Y. Meng, D. Gu, F. Zhang, Y. Shi, H. Yang, Z. Li, C. Yu, B. Tu and D. Zhao, *Angew. Chem. Int. Ed.*, 2005, **44**, 7053–7059.

72 S. Tanaka, N. Nishiyama, Y. Egashira and K. Ueyama, *Chem. Commun.*, 2005, 2125–2127.

73 G.-P. Hao, W.-C. Li, D. Qian, G.-H. Wang, W.-P. Zhang, T. Zhang, A.-Q. Wang, F. Schüth, H.-J. Bongard and A.-H. Lu, *J. Am. Chem. Soc.*, 2011, **133**, 11378–11388.

74 G.-P. Hao, W.-C. Li, D. Qian and A.-H. Lu, *Adv. Mater.*, 2010, **22**, 853–857.

75 R. W. Pekala, *J. Mater. Sci.*, 1989, **24**, 3221–3227.

76 F.-D. Han, Y.-J. Bai, R. Liu, B. Yao, Y.-X. Qi, N. Lun and J.-X. Zhang, *Adv. Energy Mater.*, 2011, **1**, 798–801.

77 A. S. Jalilov, G. Ruan, C.-C. Hwang, D. E. Schipper, J. J. Tour, Y. Li, H. Fei, E. L. G. Samuel and J. M. Tour, *ACS Appl. Mater. Interfaces*, 2015, **7**, 1376–1382.

78 Q. Zeng, D. Wu, C. Zou, F. Xu, R. Fu, Z. Li, Y. Liang and D. Su, *Chem Commun*, 2010, **46**, 5927–5929.

79 Y. Wan, X. Qian, N. Jia, Z. Wang, H. Li and D. Zhao, *Chem. Mater.*, 2008, **20**, 1012–1018.

80 S.-C. Qi, Y. Liu, A.-Z. Peng, D.-M. Xue, X. Liu, X.-Q. Liu and L.-B. Sun, *Chem. Eng. J.*, 2019, **361**, 945–952.

81 M. C. Gutiérrez, F. Rubio and F. del Monte, *Chem. Mater.*, 2010, **22**, 2711–2719.

82 M. Hu, J. Reboul, S. Furukawa, N. L. Torad, Q. Ji, P. Srinivasu, K. Ariga, S. Kitagawa and Y. Yamauchi, *J. Am. Chem. Soc.*, 2012, **134**, 2864–2867.

83 A. E. Creamer and B. Gao, *Environ. Sci. Technol.*, 2016, **50**, 7276–7289.

84 Y. Wang, K. Zhong, Z. Huang, L. Chen, Y. Dai, H. Zhang, M. Su, J. Yan, S. Yang, M. Li, T. Xu and J. Tang, *J. Power Sources*, 2020, **450**, 227681.

85 H. Nishihara, Q.-H. Yang, P.-X. Hou, M. Unno, S. Yamauchi, R. Saito, J. I. Paredes, A. Martínez-Alonso, J. M. D. Tascón, Y. Sato, M. Terauchi and T. Kyotani, *Carbon*, 2009, **47**, 1220–1230.

86 Q. Wang, W. Xia, W. Guo, L. An, D. Xia and R. Zou, *Chem. – Asian J.*, 2013, **8**, 1879–1885.

87 G. Qin, K.-R. Hao, Q.-B. Yan, M. Hu and G. Su, *Nanoscale*, 2019, **11**, 5798–5806.

88 Z. Xing, N. Gao, Y. Qi, X. Ji and H. Liu, *Carbon*, 2017, **115**, 271–278.

89 T. Kim, J. Lee and K.-H. Lee, *RSC Adv.*, 2016, **6**, 24667–24674.

90 P. F. Fulvio, R. T. Mayes, X. Wang, S. M. Mahurin, J. C. Bauer, V. Presser, J. McDonough, Y. Gogotsi and S. Dai, *Adv. Funct. Mater.*, 2011, **21**, 2208–2215.

91 X. Li, Q. Xue, X. Chang, L. Zhu, C. Ling and H. Zheng, *ACS Appl. Mater. Interfaces*, 2017, **9**, 8336–8343.

92 S. Stankovich, D. A. Dikin, G. H. B. Dommett, K. M. Kohlhaas, E. J. Zimney, E. A. Stach, R. D. Piner, S. T. Nguyen and R. S. Ruoff, *Nature*, 2006, **442**, 282–286.

93 A. K. Geim, *Science*, 2009, **324**, 1530–1534.

94 Y. Zhu, S. Murali, W. Cai, X. Li, J. W. Suk, J. R. Potts and R. S. Ruoff, *Adv. Mater.*, 2010, **22**, 3906–3924.

95 D. R. Dreyer, S. Park, C. W. Bielawski and R. S. Ruoff, *Chem Soc Rev*, 2010, **39**, 228–240.

96 G. Srinivas, J. Burress and T. Yildirim, *Energy Environ. Sci.*, 2012, **5**, 6453.

97 M. Shan, Q. Xue, N. Jing, C. Ling, T. Zhang, Z. Yan and J. Zheng, *Nanoscale*, 2012, **4**, 5477.

98 A. Lerf, H. He, M. Forster and J. Klinowski, *J. Phys. Chem. B*, 1998, **102**, 4477–4482.

99 S. P. Koenig, L. Wang, J. Pellegrino and J. S. Bunch, *Nat. Nanotechnol.*, 2012, **7**, 728–732.

100 S. Iijima, *Nature*, 1991, **354**, 56–58.

101 D. N. Futaba, K. Hata, T. Yamada, T. Hiraoka, Y. Hayamizu, Y. Kakudate, O. Tanaike, H. Hatori, M. Yumura and S. Iijima, *Nat. Mater.*, 2006, **5**, 987–994.

102 D. Deng, L. Yu, X. Chen, G. Wang, L. Jin, X. Pan, J. Deng, G. Sun and X. Bao, *Angew. Chem. Int. Ed.*, 2013, **52**, 371–375.

103 M. Rahimi, D. J. Babu, J. K. Singh, Y.-B. Yang, J. J. Schneider and F. Müller-Plathe, *J. Chem. Phys.*, 2015, **143**, 124701.

104 M. Zheng, Y. Chi, Q. Hu, H. Tang, X. Jiang, L. Zhang, S. Zhang, H. Pang and Q. Xu, *J. Mater. Chem. A*, 2019, **7**, 17204–17241.

105 W. Shen, S. Zhang, Y. He, J. Li and W. Fan, *J Mater Chem*, 2011, **21**, 14036–14040.

106 M. Asai, T. Ohba, T. Iwanaga, H. Kanoh, M. Endo, J. Campos-Delgado, M. Terrones, K. Nakai and K. Kaneko, *J. Am. Chem. Soc.*, 2011, **133**, 14880–14883.

107 D. Mantzalis, N. Asproulis and D. Drikakis, *Phys. Rev. E*, 2011, **84**, 066304.

108 H. W. Kroto, J. R. Heath, S. C. O'Brien, R. F. Curl and R. E. Smalley, *Nature*, 1985, **318**, 162–163.

109 W. Krätschmer, L. D. Lamb, K. Fostiropoulos and D. R. Huffman, *Nature*, 1990, **347**, 354–358.

110 C. Shan, H.-J. Yen, K. Wu, Q. Lin, M. Zhou, X. Guo, D. Wu, H. Zhang, G. Wu and H.-L. Wang, *Nano Energy*, 2017, **40**, 327–335.

111 D. Pontiroli, S. Scaravonati, M. Sidoli, G. Magnani, L. Fornasini, C. Milanese and M. Riccò, *Chem. Phys. Lett.*, 2019, **731**, 136607.

112 J. Friedl, M. A. Lebedeva, K. Porfyrakis, U. Stimming and T. W. Chamberlain, *J. Am. Chem. Soc.*, 2018, **140**, 401–405.

113 J. Coro, M. Suárez, L. S. R. Silva, K. I. B. Eguiluz and G. R. Salazar-Banda, *Int. J. Hydrog. Energy*, 2016, **41**, 17944–17959.

114 S. H. Noh, C. Kwon, J. Hwang, T. Ohsaka, B.-J. Kim, T.-Y. Kim, Y.-G. Yoon, Z. Chen, M. H. Seo and B. Han, *Nanoscale*, 2017, **9**, 7373–7379.

115 F. Gao, G.-L. Zhao, S. Yang and J. J. Spivey, *J. Am. Chem. Soc.*, 2013, **135**, 3315–3318.

116 P. Sood, K. C. Kim and S. S. Jang, *ChemPhysChem*, 2018, **19**, 753–758.

117 Y.-Z. Chen, G. Cai, Y. Wang, Q. Xu, S.-H. Yu and H.-L. Jiang, *Green Chem.*, 2016, **18**, 1212–1217.

118 M. Sabo, A. Henschel, H. Fröde, E. Klemm and S. Kaskel, *J. Mater. Chem.*, 2007, **17**, 3827–3832.

119 P. Serp, P. Kalck and R. Feurer, *Chem. Rev.*, 2002, **102**, 3085–3128.

120 Q.-L. Zhu, J. Li and Q. Xu, *J. Am. Chem. Soc.*, 2013, **135**, 10210–10213.

121 M. Imperor-Clerc, D. Bazin, M.-D. Appay, P. Beaunier and A. Davidson, *Chem. Mater.*, 2004, **16**, 1813–1821.

122 A. Aijaz, A. Karkamkar, Y. J. Choi, N. Tsumori, E. Rönnebro, T. Autrey, H. Shioyama and Q. Xu, *J. Am. Chem. Soc.*, 2012, **134**, 13926–13929.

123 T. Ishida, N. Kinoshita, H. Okatsu, T. Akita, T. Takei and M. Haruta, *Angew. Chem. Int. Ed.*, 2008, **47**, 9265–9268.

124 H. Okatsu, N. Kinoshita, T. Akita, T. Ishida and M. Haruta, *Appl. Catal. Gen.*, 2009, **369**, 8–14.

125 H.-L. Jiang, Q.-P. Lin, T. Akita, B. Liu, H. Ohashi, H. Oji, T. Honma, T. Takei, M. Haruta and Q. Xu, *Chem. - Eur. J.*, 2011, **17**, 78–81.

126 I. Katsounaros, S. Cherevko, A. R. Zeradjanin and K. J. J. Mayrhofer, *Angew. Chem. Int. Ed.*, 2014, **53**, 102–121.

127 M.-S. Balogun, H. Yang, Y. Luo, W. Qiu, Y. Huang, Z.-Q. Liu and Y. Tong, *Energy Environ. Sci.*, 2018, **11**, 1859–1869.

128 J.-S. Lee, S. Tai Kim, R. Cao, N.-S. Choi, M. Liu, K. T. Lee and J. Cho, *Adv. Energy Mater.*, 2011, **1**, 34–50.

129 Y. Li and H. Dai, *Chem. Soc. Rev.*, 2014, **43**, 5257–5275.

130 Y. Li and J. Lu, *ACS Energy Lett.*, 2017, **2**, 1370–1377.

131 R. Cao, J.-S. Lee, M. Liu and J. Cho, *Adv. Energy Mater.*, 2012, **2**, 816–829.

132 J.-S. Lee, T. Lee, H.-K. Song, J. Cho and B.-S. Kim, *Energy Environ. Sci.*, 2011, **4**, 4148.

133 D. U. Lee, P. Xu, Z. P. Cano, A. G. Kashkooli, M. G. Park and Z. Chen, *J. Mater. Chem. A*, 2016, **4**, 7107–7134.

134 J. Yin, Y. Li, F. Lv, Q. Fan, Y.-Q. Zhao, Q. Zhang, W. Wang, F. Cheng, P. Xi and S. Guo, *ACS Nano*, 2017, **11**, 2275–2283.

135 Z.-Q. Liu, H. Cheng, N. Li, T. Y. Ma and Y.-Z. Su, *Adv. Mater.*, 2016, **28**, 3777–3784.

136 H. Cheng, M.-L. Li, C.-Y. Su, N. Li and Z.-Q. Liu, *Adv. Funct. Mater.*, 2017, **27**, 1701833.

137 H. Cheng, J.-M. Chen, Q.-J. Li, C.-Y. Su, A.-N. Chen, J.-X. Zhang, Z.-Q. Liu and Y. Tong, *Chem. Commun.*, 2017, **53**, 11596–11599.

138 X. Liu, M. Park, M. G. Kim, S. Gupta, G. Wu and J. Cho, *Angew. Chem. Int. Ed.*, 2015, **54**, 9654–9658.

139 D. Yan, Y. Li, J. Huo, R. Chen, L. Dai and S. Wang, *Adv. Mater.*, 2017, **29**, 1606459.

140 Z. Liu, Z. Zhao, Y. Wang, S. Dou, D. Yan, D. Liu, Z. Xia and S. Wang, *Adv. Mater.*, 2017, **29**, 1606207.

141 M. S. Faber, R. Dziedzic, M. A. Lukowski, N. S. Kaiser, Q. Ding and S. Jin, *J. Am. Chem. Soc.*, 2014, **136**, 10053–10061.

142 W. Kiciński, M. Szala and M. Bystrzejewski, *Carbon*, 2014, **68**, 1–32.

143 Z. Shadike, M.-H. Cao, F. Ding, L. Sang and Z.-W. Fu, *Chem. Commun.*, 2015, **51**, 10486–10489.

144 Z. X. Huang, Y. Wang, J. I. Wong, W. H. Shi and H. Y. Yang, *Electrochimica Acta*, 2015, **167**, 388–395.

145 M. Kuang, Q. Wang, P. Han and G. Zheng, *Adv. Energy Mater.*, 2017, **7**, 1700193.

146 J. Tang, J. Shen, N. Li and M. Ye, *Ceram. Int.*, 2014, **40**, 15411–15419.

147 G. Mera, A. Navrotsky, S. Sen, H.-J. Kleebe and R. Riedel, *J. Mater. Chem. A*, 2013, **1**, 3826.

148 F. Shahzad, P. Kumar, S. Yu, S. Lee, Y.-H. Kim, S. M. Hong and C. M. Koo, *J. Mater. Chem. C*, 2015, **3**, 9802–9810.

149 H. Huang, J. Zhu, W. Zhang, C. S. Tiwary, J. Zhang, X. Zhang, Q. Jiang, H. He, Y. Wu, W. Huang, P. M. Ajayan and Q. Yan, *Chem. Mater.*, 2016, **28**, 1737–1745.

150 Q. Xu, P. Pu, J. Zhao, C. Dong, C. Gao, Y. Chen, J. Chen, Y. Liu and H. Zhou, *J. Mater. Chem. A*, 2015, **3**, 542–546.

151 W. Niu, Z. Li, K. Marcus, L. Zhou, Y. Li, R. Ye, K. Liang and Y. Yang, *Adv. Energy Mater.*, 2018, **8**, 1701642.

152 X. Cui, Z. Xie and Y. Wang, *Nanoscale*, 2016, **8**, 11984–11992.

153 L. Samad, M. Cabán-Acevedo, M. J. Shearer, K. Park, R. J. Hamers and S. Jin, *Chem. Mater.*, 2015, **27**, 3108–3114.

154 M. Li, C. Liu, H. Zhao, H. An, H. Cao, Y. Zhang and Z. Fan, *Carbon*, 2015, **86**, 197–206.

155 A. M. El-Sawy, I. M. Mosa, D. Su, C. J. Guild, S. Khalid, R. Joesten, J. F. Rusling and S. L. Suib, *Adv. Energy Mater.*, 2016, **6**, 1501966.

156 J. Ye, F. He, J. Nie, Y. Cao, H. Yang and X. Ai, *J. Mater. Chem. A*, 2015, **3**, 7406–7412.

157 D. Sun, R. Ban, P.-H. Zhang, G.-H. Wu, J.-R. Zhang and J.-J. Zhu, *Carbon*, 2013, **64**, 424–434.

158 G. Li, X. Wang, J. Fu, J. Li, M. G. Park, Y. Zhang, G. Lui and Z. Chen, *Angew. Chem. Int. Ed.*, 2016, **55**, 4977–4982.

159 Y. Su, Y. Zhu, H. Jiang, J. Shen, X. Yang, W. Zou, J. Chen and C. Li, *Nanoscale*, 2014, **6**, 15080–15089.

160 J. Fu, Z. P. Cano, M. G. Park, A. Yu, M. Fowler and Z. Chen, *Adv. Mater.*, 2017, **29**, 1604685.

161 Z. Chen, M. Waje, W. Li and Y. Yan, *Angew. Chem. Int. Ed.*, 2007, **46**, 4060–4063.

162 A. Zadick, L. Dubau, N. Sergent, G. Berthomé and M. Chatenet, *ACS Catal.*, 2015, **5**, 4819–4824.

163 Z. Yang, Z. Yao, G. Li, G. Fang, H. Nie, Z. Liu, X. Zhou, X. Chen and S. Huang, *ACS Nano*, 2012, **6**, 205–211.

164 L. Zhang and Z. Xia, *J. Phys. Chem. C*, 2011, **115**, 11170–11176.

165 Y. Cao, M. Li, J. Lu, J. Liu and K. Amine, *Nat. Nanotechnol.*, 2019, **14**, 200–207.

166 Z. P. Cano, D. Banham, S. Ye, A. Hintennach, J. Lu, M. Fowler and Z. Chen, *Nat. Energy*, 2018, **3**, 279–289.

167 J. Xie, H.-J. Peng, J.-Q. Huang, W.-T. Xu, X. Chen and Q. Zhang, *Angew. Chem. Int. Ed.*, 2017, **56**, 16223–16227.

168 F. Wu, S. Chen, V. Srot, Y. Huang, S. K. Sinha, P. A. van Aken, J. Maier and Y. Yu, *Adv. Mater.*, 2018, **30**, 1706643.

169 Y. Son, J.-S. Lee, Y. Son, J.-H. Jang and J. Cho, *Adv. Energy Mater.*, 2015, **5**, 1500110.

170 X. Wu, A. Markir, Y. Xu, E. C. Hu, K. T. Dai, C. Zhang, W. Shin, D. P. Leonard, K. Kim and X. Ji, *Adv. Energy Mater.*, 2019, **9**, 1902422.

171 X. Wang, G. Li, J. Li, Y. Zhang, A. Wook, A. Yu and Z. Chen, *Energy Environ. Sci.*, 2016, **9**, 2533–2538.

172 T. Zhou, W. Lv, J. Li, G. Zhou, Y. Zhao, S. Fan, B. Liu, B. Li, F. Kang and Q.-H. Yang, *Energy Environ. Sci.*, 2017, **10**, 1694–1703.

173 W. Xue, D. Yu, L. Suo, C. Wang, Z. Wang, G. Xu, X. Xiao, M. Ge, M. Ko, Y. Chen, L. Qie, Z. Zhu, A. S. Helal, W.-K. Lee and J. Li, *Matter*, 2019, **1**, 1047–1060.

174 Y. Song, Z. Sun, J. Cai, N. Wei, M. Wang, Y. Shao, Z. Liu and J. Sun, *J. Mater. Chem. A*, 2019, **7**, 20750–20759.

175 S. Wang, J. Liao, X. Yang, J. Liang, Q. Sun, J. Liang, F. Zhao, A. Koo, F. Kong, Y. Yao, X. Gao, M. Wu, S.-Z. Yang, R. Li and X. Sun, *Nano Energy*, 2019, **57**, 230–240.

176 H. Lin, L. Yang, X. Jiang, G. Li, T. Zhang, Q. Yao, G. W. Zheng and J. Y. Lee, *Energy Environ. Sci.*, 2017, **10**, 1476–1486.

177 M. Chhowalla, H. S. Shin, G. Eda, L.-J. Li, K. P. Loh and H. Zhang, *Nat. Chem.*, 2013, **5**, 263–275.

178 J. He and A. Manthiram, *Energy Storage Mater.*, 2019, **20**, 55–70.

179 C. Zhang, W. Lv, W. Zhang, X. Zheng, M.-B. Wu, W. Wei, Y. Tao, Z. Li and Q.-H. Yang, *Adv. Energy Mater.*, 2014, **4**, 1301565.

180 D. Chen, M. Qiao, Y.-R. Lu, L. Hao, D. Liu, C.-L. Dong, Y. Li and S. Wang, *Angew. Chem. Int. Ed.*, 2018, **57**, 8691–8696.

181 P. Zhang, J. Zhang and J. Gong, *Chem. Soc. Rev.*, 2014, **43**, 4395–4422.

182 W.-J. Chun, A. Ishikawa, H. Fujisawa, T. Takata, J. N. Kondo, M. Hara, M. Kawai, Y. Matsumoto and K. Domen, *J. Phys. Chem. B*, 2003, **107**, 1798–1803.

183 Y. Wang, R. Zhang, J. Chen, H. Wu, S. Lu, K. Wang, H. Li, C. J. Harris, K. Xi, R. V. Kumar and S. Ding, *Adv. Energy Mater.*, 2019, 1900953.

184 C. Chaneliere, J. L. Autran, R. A. B. Devine and B. Balland, *Mater. Sci. Eng. R Rep.*, 1998, **22**, 269–322.

185 A. G. Mal'chik, S. A. Kuznetsova, S. O. Kryuchkova and V. V. Kozik, *Inorg. Mater.*, 2017, **53**, 994–1003.

186 V. Etacheri, C. Wang, M. J. O'Connell, C. K. Chan and V. G. Pol, *J. Mater. Chem. A*, 2015, **3**, 9861–9868.

187 C. Joseph, P. Bourson and M. D. Fontana, *J. Raman Spectrosc.*, 2012, **43**, 1146–1150.

188 S. Xia, J. Ni, S. V. Savilov and L. Li, *Nano Energy*, 2018, **45**, 407–412.

189 J. F. Carneiro, R. S. Rocha, P. Hammer, R. Bertazzoli and M. R. V. Lanza, *Appl. Catal. Gen.*, 2016, **517**, 161–167.

190 C. Yuan, J. Li, L. Hou, X. Zhang, L. Shen and X. W. (David) Lou, *Adv. Funct. Mater.*, 2012, **22**, 4592–4597.

191 D. Luo, G. Li, Y.-P. Deng, Z. Zhang, J. Li, R. Liang, M. Li, Y. Jiang, W. Zhang, Y. Liu, W. Lei, A. Yu and Z. Chen, *Adv. Energy Mater.*, 2019, **9**, 1900228.

192 R. Gao, Z. Li, X. Zhang, J. Zhang, Z. Hu and X. Liu, *ACS Catal.*, 2016, **6**, 400–406.

193 Y. Zhang, Z. Mu, C. Yang, Z. Xu, S. Zhang, X. Zhang, Y. Li, J. Lai, Z. Sun, Y. Yang, Y. Chao, C. Li, X. Ge, W. Yang and S. Guo, *Adv. Funct. Mater.*, 2018, **28**, 1707578.

194 M. Brown, R. E. Peierls and E. A. Stern, *Phys. Rev. B*, 1977, **15**, 738–744.

195 T. Tsuchiya, H. Imai, S. Miyoshi, P.-A. Glans, J. Guo and S. Yamaguchi, *Phys. Chem. Chem. Phys.*, 2011, **13**, 17013.

196 D. S. Gatewood, T. L. Schull, O. Baturina, J. J. Pietron, Y. Garsany, K. E. Swider-Lyons and D. E. Ramaker, *J. Phys. Chem. C*, 2008, **112**, 4961–4970.

197 S.-M. Paek and Y.-I. Kim, *J. Alloys Compd.*, 2014, **587**, 251–254.

198 R. Ramprasad, *J. Appl. Phys.*, 2003, **94**, 5609–5612.

199 D. M. Pickup, G. Mountjoy, M. A. Holland, G. W. Wallidge, R. J. Newport and M. E. Smith, *J. Mater. Chem.*, 2000, **10**, 1887–1894.

200 Y. R. Denny, T. Firmansyah, S. K. Oh, H. J. Kang, D.-S. Yang, S. Heo, J. Chung and J. C. Lee, *Mater. Res. Bull.*, 2016, **82**, 1–6.

201 W. Cai, G. Li, K. Zhang, G. Xiao, C. Wang, K. Ye, Z. Chen, Y. Zhu and Y. Qian, *Adv. Funct. Mater.*, 2018, **28**, 1704865.

202 J. Wang, J. Liang, J. Wu, C. Xuan, Z. Wu, X. Guo, C. Lai, Y. Zhu and D. Wang, *J. Mater. Chem. A*, 2018, **6**, 6503–6509.

203 G. Li, W. Lei, D. Luo, Y. Deng, Z. Deng, D. Wang, A. Yu and Z. Chen, *Energy Environ. Sci.*, 2018, **11**, 2372–2381.

204 T.-Z. Hou, W.-T. Xu, X. Chen, H.-J. Peng, J.-Q. Huang and Q. Zhang, *Angew. Chem. Int. Ed.*, 2017, **56**, 8178–8182.

205 J. Hwang, R. R. Rao, L. Giordano, Y. Katayama, Y. Yu and Y. Shao-Horn, *Science*, 2017, **358**, 751.

206 D. Liu, C. Zhang, G. Zhou, W. Lv, G. Ling, L. Zhi and Q.-H. Yang, *Adv. Sci.*, 2018, **5**, 1700270.

207 J. S. Yeon, S. H. Park, J. Suk, H. Lee and H. S. Park, *Chem. Eng. J.*, 2020, **382**, 122946.

208 D. Luo, Y.-P. Deng, X. Wang, G. Li, J. Wu, J. Fu, W. Lei, R. Liang, Y. Liu, Y. Ding, A. Yu and Z. Chen, *ACS Nano*, 2017, **11**, 11521–11530.

209 D. Su, M. Cortie, H. Fan and G. Wang, *Adv. Mater.*, 2017, **29**, 1700587.

210 W. Bao, D. Su, W. Zhang, X. Guo and G. Wang, *Adv. Funct. Mater.*, 2016, **26**, 8746–8756.

211 Z. Li, C. Li, X. Ge, J. Ma, Z. Zhang, Q. Li, C. Wang and L. Yin, *Nano Energy*, 2016, **23**, 15–26.

212 Y. An, Z. Zhang, H. Fei, S. Xiong, B. Ji and J. Feng, *ACS Appl. Mater. Interfaces*, 2017, **9**, 12400–12407.

213 Q. Sun, B. Xi, J.-Y. Li, H. Mao, X. Ma, J. Liang, J. Feng and S. Xiong, *Adv. Energy Mater.*, 2018, **8**, 1800595.

214 S. Liu, J. Li, X. Yan, Q. Su, Y. Lu, J. Qiu, Z. Wang, X. Lin, J. Huang, R. Liu, B. Zheng, L. Chen, R. Fu and D. Wu, *Adv. Mater.*, 2018, **30**, 1706895.

215 Z. Xiao, Z. Yang, L. Zhang, H. Pan and R. Wang, *ACS Nano*, 2017, **11**, 8488–8498.

216 S. Shen, X. Xia, Y. Zhong, S. Deng, D. Xie, B. Liu, Y. Zhang, G. Pan, X. Wang and J. Tu, *Adv. Mater.*, 2019, **31**, 1900009.

217 Z. Xing, G. Li, S. Sy and Z. Chen, *Nano Energy*, 2018, **54**, 1–9.

218 P. De Luna, C. Hahn, D. Higgins, S. A. Jaffer, T. F. Jaramillo and E. H. Sargent, *Science*, 2019, **364**, eaav3506.

219 J. Artz, T. E. Müller, K. Thenert, J. Kleinekorte, R. Meys, A. Sternberg, A. Bardow and W. Leitner, *Chem. Rev.*, 2018, **118**, 434–504.

220 C. Hepburn, E. Adlen, J. Beddington, E. A. Carter, S. Fuss, N. Mac Dowell, J. C. Minx, P. Smith and C. K. Williams, *Nature*, 2019, **575**, 87–97.

221 Y. Y. Birdja, E. Pérez-Gallent, M. C. Figueiredo, A. J. Göttle, F. Calle-Vallejo and M. T. M. Koper, *Nat. Energy*, 2019, **4**, 732–745.

222 G. M. Tomboc, S. Choi, T. Kwon, Y. J. Hwang and K. Lee, *Adv. Mater.*, 2020, **32**, 1908398.

223 L. Sun, V. Reddu, A. C. Fisher and X. Wang, *Energy Environ. Sci.*, 2020, **13**, 374–403.

224 H. Zhong, M. Ghorbani-Asl, K. H. Ly, J. Zhang, J. Ge, M. Wang, Z. Liao, D. Makarov, E. Zschech, E. Brunner, I. M. Weidinger, J. Zhang, A. V. Krasheninnikov, S. Kaskel, R. Dong and X. Feng, *Nat. Commun.*, 2020, **11**, 1409.

225 J. Rosen, G. S. Hutchings, Q. Lu, R. V. Forest, A. Moore and F. Jiao, *ACS Catal.*, 2015, **5**, 4586–4591.

226 Y. Wang, L. Cao, N. J. Libretto, X. Li, C. Li, Y. Wan, C. He, J. Lee, J. Gregg, H. Zong, D. Su, J. T. Miller, T. Mueller and C. Wang, *J. Am. Chem. Soc.*, 2019, **141**, 16635–16642.

227 N. Han, P. Ding, L. He, Y. Li and Y. Li, *Adv. Energy Mater.*, 2020, **10**, 1902338.

228 N. Han, Y. Wang, H. Yang, J. Deng, J. Wu, Y. Li and Y. Li, *Nat. Commun.*, 2018, **9**, 1320.

229 X. Duan, J. Xu, Z. Wei, J. Ma, S. Guo, S. Wang, H. Liu and S. Dou, *Adv. Mater.*, 2017, **29**, 1701784.

230 W. Luc and F. Jiao, *ACS Catal.*, 2017, **7**, 5856–5861.

231 Z. Ma, S. Li, L. Wu, L. Song, G. Jiang, Z. Liang, D. Su, Y. Zhu, R. R. Adzic, J. X. Wang and Z. Chen, *Nano Energy*, 2020, **69**, 104455.

232 Z. Xing, Y.-P. Deng, S. Sy, G. Tan, A. Li, J. Li, Y. Niu, N. Li, D. Su, J. Lu and Z. Chen, *Nano Energy*, 2019, **65**, 104051.

233 D. Luo, Z. Zhang, G. Li, S. Cheng, S. Li, J. Li, R. Gao, M. Li, S. Sy, Y.-P. Deng, Y. Jiang, Y. Zhu, H. Dou, Y. Hu, A. Yu and Z. Chen, *ACS Nano*, 2020, **14**, 4849–4860.

234 W. Kohn and L. J. Sham, *Phys. Rev.*, 1965, **140**, A1133–A1138.

235 P. E. Blöchl, *Phys. Rev. B*, 1994, **50**, 17953–17979.

236 G. Kresse and J. Furthmüller, *Phys. Rev. B*, 1996, **54**, 11169–11186.

237 K. Bashyal, C. K. Pyles, S. Afroosheh, A. Lamichhane and A. T. Zayak, *J. Phys. Condens. Matter*, 2018, **30**, 065501.

238 S. Verma, Y. Hamasaki, C. Kim, W. Huang, S. Lu, H.-R. M. Jhong, A. A. Gewirth, T. Fujigaya, N. Nakashima and P. J. A. Kenis, *ACS Energy Lett.*, 2018, **3**, 193–198.

239 C. M. Gabardo, A. Seifitokaldani, J. P. Edwards, C.-T. Dinh, T. Burdyny, M. G. Kibria, C. P. O'Brien, E. H. Sargent and D. Sinton, *Energy Environ. Sci.*, 2018, **11**, 2531–2539.

240 Z. Geng, X. Kong, W. Chen, H. Su, Y. Liu, F. Cai, G. Wang and J. Zeng, *Angew. Chem. Int. Ed.*, 2018, **57**, 6054–6059.

241 D. L. T. Nguyen, Y. Kim, Y. J. Hwang and D. H. Won, *Carbon Energy*, 2020, **2**, 72–98.

242 N. Wu, L. Xiao and L. Zhuang, *J. Mater. Chem. A*, 2019, **7**, 20567–20573.

243 J. Xiao and T. Frauenheim, *J. Phys. Chem. C*, 2013, **117**, 1804–1808.

244 X. Bai, W. Chen, C. Zhao, S. Li, Y. Song, R. Ge, W. Wei and Y. Sun, *Angew. Chem. Int. Ed.*, 2017, **56**, 12219–12223.

245 M. Dunwell, Q. Lu, J. M. Heyes, J. Rosen, J. G. Chen, Y. Yan, F. Jiao and B. Xu, *J. Am. Chem. Soc.*, 2017, **139**, 3774–3783.

246 S. Liu, C. Sun, J. Xiao and J.-L. Luo, *ACS Catal.*, 2020, **10**, 3158–3163.

247 Y. Zhou, R. Zhou, X. Zhu, N. Han, B. Song, T. Liu, G. Hu, Y. Li, J. Lu and Y. Li, *Adv. Mater.*, 2020, **32**, 2000992.

248 R. Gao, L. Pan, H. Wang, X. Zhang, L. Wang and J.-J. Zou, *ACS Catal.*, 2018, **8**, 8420–8429.

249 G. Wen, B. Ren, M. G. Park, J. Yang, H. Dou, Z. Zhang, Y. Deng, Z. Bai, L. Yang, J. Gostick, G. A. Botton, Y. Hu and Z. Chen, *Angew. Chem. Int. Ed.*, 2020, **59**, 12860–12867.

250 G. Wen, D. U. Lee, B. Ren, F. M. Hassan, G. Jiang, Z. P. Cano, J. Gostick, E. Croiset, Z. Bai, L. Yang and Z. Chen, *Adv. Energy Mater.*, 2018, **8**, 1802427.

251 J. W. F. To, Z. Chen, H. Yao, J. He, K. Kim, H.-H. Chou, L. Pan, J. Wilcox, Y. Cui and Z. Bao, *ACS Cent. Sci.*, 2015, **1**, 68–76.

252 H. Xiao, W. Zhang, Q. Yao, L. Huang, L. Chen, B. Boury and Z. Chen, *Appl. Catal. B Environ.*, 2019, **244**, 719–731.

253 R. Al-Gaashani, S. Radiman, A. R. Daud, N. Tabet and Y. Al-Douri, *Ceram. Int.*, 2013, **39**, 2283–2292.

254 M.-Y. Kim, M. H. Naveen, N. G. Gurudatt and Y.-B. Shim, *Small*, 2017, **13**, 1700502.

255 N. J. Firet, M. A. Blommaert, T. Burdyny, A. Venugopal, D. Bohra, A. Longo and W. A. Smith, *J. Mater. Chem. A*, 2019, **7**, 2597–2607.

256 S. Akel, R. Dillert, N. Balayeva, R. Boughaled, J. Koch, M. El Azzouzi and D. Bahnemann, *Catalysts*, 2018, **8**, 647.

257 J. Feng, D. Fan, Q. Wang, L. Ma, W. Wei, J. Xie and J. Zhu, *Colloids Surf. Physicochem. Eng. Asp.*, 2017, **520**, 743–756.

258 D. Samanta and P. Jena, *J. Am. Chem. Soc.*, 2012, **134**, 8400–8403.

259 A. K. Rana, Y. Kumar, P. Rajput, S. N. Jha, D. Bhattacharyya and P. M. Shirage, *ACS Appl. Mater. Interfaces*, 2017, **9**, 7691–7700.

260 S. Kumar, S. Basu, B. Rana, A. Barman, S. Chatterjee, S. N. Jha, D. Bhattacharyya, N. K. Sahoo and A. K. Ghosh, *J. Mater. Chem. C*, 2014, **2**, 481–495.

261 S.-H. Park, C.-H. Kwak, S.-Y. Seo, S.-H. Kim, B.-H. Kim, C.-I. Park, Y.-W. Park and S.-W. Han, *J. Korean Phys. Soc.*, 2009, **55**, 94–97.

262 J. Rosen, G. S. Hutchings, Q. Lu, S. Rivera, Y. Zhou, D. G. Vlachos and F. Jiao, *ACS Catal.*, 2015, **5**, 4293–4299.

263 W. I. U. Withanage, S. Yanagida, T. Takei and N. Kumada, *J. Ceram. Soc. Jpn.*, 2018, **126**, 784–788.

264 Z. Wang, K. Teramura, S. Hosokawa and T. Tanaka, *Appl. Catal. B Environ.*, 2015, **163**, 241–247.

265 M. Favaro, H. Xiao, T. Cheng, W. A. Goddard, J. Yano and E. J. Crumlin, *Proc. Natl. Acad. Sci.*, 2017, **114**, 6706–6711.

266 D. L. T. Nguyen, C. W. Lee, J. Na, M.-C. Kim, N. D. K. Tu, S. Y. Lee, Y. J. Sa, D. H. Won, H.-S. Oh, H. Kim, B. K. Min, S. S. Han, U. Lee and Y. J. Hwang, *ACS Catal.*, 2020, **10**, 3222–3231.

267 K. Liu, J. Wang, M. Shi, J. Yan and Q. Jiang, *Adv. Energy Mater.*, 2019, **9**, 1900276.

268 K. Jiang, H. Wang, W.-B. Cai and H. Wang, *ACS Nano*, 2017, **11**, 6451–6458.

269 D. H. Won, H. Shin, J. Koh, J. Chung, H. S. Lee, H. Kim and S. I. Woo, *Angew. Chem. Int. Ed.*, 2016, **55**, 9297–9300.

270 S. Lamaison, D. Wakerley, J. Blanchard, D. Montero, G. Rousse, D. Mercier, P. Marcus, D. Taverna, D. Giaume, V. Mougel and M. Fontecave, *Joule*, 2020, **4**, 395–406.

271 S. Dou, J. Song, S. Xi, Y. Du, J. Wang, Z.-F. Huang, Z. J. Xu and X. Wang, *Angew. Chem. Int. Ed.*, 2019, **58**, 4041–4045.

272 Q. H. Low, N. W. X. Loo, F. Calle-Vallejo and B. S. Yeo, *Angew. Chem. Int. Ed.*, 2019, **58**, 2256–2260.

273 T. Zhang, X. Li, Y. Qiu, P. Su, W. Xu, H. Zhong and H. Zhang, *J. Catal.*, 2018, **357**, 154–162.

274 P. Moreno-García, N. Schlegel, A. Zanetti, A. Cedeño López, M. de J. Gálvez-Vázquez, A. Dutta, M. Rahaman and P. Broekmann, *ACS Appl. Mater. Interfaces*, 2018, **10**, 31355–31365.

275 D. L. T. Nguyen, M. S. Jee, D. H. Won, H. Jung, H.-S. Oh, B. K. Min and Y. J. Hwang, *ACS Sustain. Chem. Eng.*, 2017, **5**, 11377–11386.

276 J. Huang, M. Mensi, E. Oveisi, V. Mantella and R. Buonsanti, *J. Am. Chem. Soc.*, 2019, **141**, 2490–2499.

277 F.-Y. Gao, S.-J. Hu, X.-L. Zhang, Y.-R. Zheng, H.-J. Wang, Z.-Z. Niu, P.-P. Yang, R.-C. Bao, T. Ma, Z. Dang, Y. Guan, X.-S. Zheng, X. Zheng, J.-F. Zhu, M.-R. Gao and S.-H. Yu, *Angew. Chem. Int. Ed.*, 2020, **132**, 8784–8790.

278 K. Ye, Z. Zhou, J. Shao, L. Lin, D. Gao, N. Ta, R. Si, G. Wang and X. Bao, *Angew. Chem. Int. Ed.*, 2020, **59**, 4814–4821.

279 C. He, Y. Zhang, Y. Zhang, L. Zhao, L. Yuan, J. Zhang, J. Ma and J. Hu, *Angew. Chem. Int. Ed.*, 2020, **59**, 4914–4919.

280 W. Zhu, L. Zhang, S. Liu, A. Li, X. Yuan, C. Hu, G. Zhang, W. Deng, K. Zang, J. Luo, Y. Zhu, M. Gu, Z. Zhao and J. Gong, *Angew. Chem. Int. Ed.*, 2020, **59**, 12664–12668.

281 X. Lu, Y. Wu, X. Yuan, L. Huang, Z. Wu, J. Xuan, Y. Wang and H. Wang, *ACS Energy Lett.*, 2018, **3**, 2527–2532.

282 Y. T. Guntern, J. R. Pankhurst, J. Vávra, M. Mensi, V. Mantella, P. Schouwink and R. Buonsanti, *Angew. Chem. Int. Ed.*, 2019, **58**, 12632–12639.

283 T. Zheng, K. Jiang, N. Ta, Y. Hu, J. Zeng, J. Liu and H. Wang, *Joule*, 2019, **3**, 265–278.

284 Y. Pan, R. Lin, Y. Chen, S. Liu, W. Zhu, X. Cao, W. Chen, K. Wu, W.-C. Cheong, Y. Wang, L. Zheng, J. Luo, Y. Lin, Y. Liu, C. Liu, J. Li, Q. Lu, X. Chen, D. Wang, Q. Peng, C. Chen and Y. Li, *J. Am. Chem. Soc.*, 2018, **140**, 4218–4221.

285 M. Liu, Y. Pang, B. Zhang, P. De Luna, O. Voznyy, J. Xu, X. Zheng, C. T. Dinh, F. Fan, C. Cao, F. P. G. de Arquer, T. S. Safaei, A. Mepham, A. Klinkova, E. Kumacheva, T. Filleter, D. Sinton, S. O. Kelley and E. H. Sargent, *Nature*, 2016, **537**, 382–386.

286 J. Li, G. Chen, Y. Zhu, Z. Liang, A. Pei, C.-L. Wu, H. Wang, H. R. Lee, K. Liu, S. Chu and Y. Cui, *Nat. Catal.*, 2018, **1**, 592–600.

287 X. Zhang, Z. Wu, X. Zhang, L. Li, Y. Li, H. Xu, X. Li, X. Yu, Z. Zhang, Y. Liang and H. Wang, *Nat. Commun.*, 2017, **8**, 14675.